The Pennsylvania State University

The Graduate School

Department of Aerospace Engineering

INVESTIGATION OF CONTACT ACOUSTIC NONLINEARITIES ON METAL AND COMPOSITE AIRFRAME STRUCTURES VIA INTENSITY BASED HEALTH MONITORING

A Thesis in

Aerospace Engineering

by

Peter Quinn Romano

Submitted in Partial Fulfillment
of the Requirements
for the Degree of

Master of Science

August 2011

The thesis of Peter Quinn Romano was reviewed and approved* by the following:

Stephen Conlon
Research Associate, PSU Applied Research Laboratory
Assistant Professor of Aerospace Engineering
Thesis Co-Advisor

Edward Smith
Professor of Aerospace Engineering
Thesis Co-Advisor

George Lesieutre
Professor of Aerospace Engineering
Head of the Department of Aerospace Engineering

*Signatures are on file in the Graduate School

ABSTRACT

The detection and monitoring of fatigue cracks on rotorcraft airframes is a major concern for maintenance personnel. While current practice relies on a schedule-based approach, this method creates large periods of time where the vehicle is grounded, and not mission capable. Structural Health Monitoring (SHM) systems strive to solve this problem by providing critical information to maintenance personnel based on the actual condition of the structure.

In this thesis, Nonlinear Structural Intensity (NSI) and Nonlinear Structural Surface Intensity (NSSI) based damage detection techniques were improved for metallic structures and extended to composite airframe structures. Several test beds were developed to facilitate experiments characterizing various types of relevant structural damage. These include an aluminum stiffened panel, integrally stiffened composite panels, and an OH-58D "Kiowa Warrior" tail boom.

Measurement of NSI maps at sub-harmonic frequencies was completed on the aluminum stiffened panel to provide enhanced understanding of the physical mechanism behind the characteristic contact acoustic nonlinearity (CAN) mechanism. An energy "source" at an ultra-subharmonic frequency was localized within the damaged footprint for the aluminum stiffened panel, a result not explicitly shown in previous studies. Additionally, a different application for the formulation of SSI was developed. NSSI as formulated in the frequency domain had a higher signal-to-noise ratio (60 dB difference in noise floor), as well as a greater overall sensitivity to damage in the form of loose fasteners (11.6 dB increase). NSSI was also evaluated to determine the sensitivity to structural damping levels, and proved to be relatively independent of the damping condition present on the structure.

A new detection metric relying on modulated wave spectroscopy was developed and implemented using the NSSI damage detection feature. This technique, denoted NSSI-MW, relied

on the interaction between two interrogation waves (in the form of combinational frequencies) to form a more stable method for damage detection while still providing a high sensitivity to damage. Results comparing NSSI to NSSI-MW showed that the single-tone approach had a higher sensitivity to damage (43.1 dB detection strength), but required judicious selection of drive force levels and frequency. NSSI-MW was able to characterize the damage response with high detection strength (27.2 dB), but did not require optimization of force or frequency. The active NSSI techniques were also extended to composite materials, adding a level of complexity due to their construction (orthotropic / anisotropic designs), as well as the higher distributed damping present in the plate structures studied. Each metric was able to detect damage in the form of a delamination in the bond line of the integral stiffener to a high degree of sensitivity.

Measurements transitioning NSSI and NSSI-MW damage detection metrics to an OH-58 tail boom flight structure showed promise for intensity-based health monitoring techniques to be applied to complex airframe structures. Consistent with measurements from both the aluminum and composite stiffened panels, NSSI was shown to have a higher sensitivity (45 dB detection strength) than NSSI-MW (22 dB detection strength) when detecting simulated damage in the form of a loose hanger bearing bracket. In addition, Both NSSI and NSSI-MW were shown to be more sensitive damage detection features than nonlinear metrics based solely on strain or acceleration.

TABLE OF CONTENTS

LIST OF FIGURES

LIST OF TABLES

ACKNOWLEDGEMENTS

Many people contributed to the successful completion of this research. I would like to thank my advisors Dr. Stephen C. Conlon and Dr. Edward C. Smith for their incredibly helpful support and insight over the entire course of my studies, both undergraduate and graduate.

Thank you to Dr. Fabio Semperlotti, and Micah Shepard for their guidance in the laboratory, and for answering the numerous questions I had in the lab. Additional thanks to Kevin Brennan and Justin Long for their help on this project. I would like to offer thanks to Dr. Thomas Juska for providing his expertise in fabricating the composite panels for this research. I am also extremely grateful to Richard Auhl, Mark Catalano, and Greg Seeger for all the help they provided me with laboratory hardware setup and accompanying issues. Last, but not least, I offer a special thank you for my friends and family for their continuous love and support throughout my time at Penn State.

I gratefully acknowledge the funding provided by the Applied Research Laboratory at the Pennsylvania State University Exploratory and Foundational program.

Chapter 1

Introduction

1.1 Background

As damage detection technology matures, structural health monitoring (SHM) systems become more feasible and are identified more frequently as critical elements of aerospace systems. On any aircraft operating within its regular flight envelope, a multitude of sources can cause damage, ranging from corrosion due to atmospheric conditions to ballistic impacts. One of the most critical damage types occurring on rotorcraft structures is fatigue cracking due to high cycle dynamic loading.

Detecting and monitoring critical cracks on any rotorcraft is a major concern for maintenance personnel. Current practice relies on a schedule based maintenance approach, often based on life cycle predictions. However, fatigue cracks and corresponding propagation cannot be completely predicted using this approach. In addition, schedule based maintenance can require a large period of time where the vehicle is grounded, and therefore not mission-capable. Structural Health Monitoring (SHM) systems strive to solve this problem by providing critical information to maintenance personnel based on the actual condition of the structure.

While true Condition Based Maintenance (CBM) is not in practice currently, several systems used within the aerospace industry are in place to help transition maintenance practices towards this approach. These Health and Usage Monitoring (HUMS) systems show a step towards a true CBM approach, but lack the ability to detect unpredicted structural damage occurring during normal flight operations, or between scheduled maintenance procedures. For critical parts experiencing cracking due to high cycle fatigue, this lack of information could result

in the failure of a critical component structure, causing catastrophic failure, and potentially severe injury to those operating the aircraft.

The need for SHM systems on rotorcraft is becoming increasingly desirable, as aging platforms require an ever increasing maintenance hour to flight hour ratio. The methods developed in this thesis aim to provide more extensive information for SHM systems that is critical to implementing a CBM approach for structures. This allows for more efficient maintenance of critical rotorcraft structural components, and reduces the associated cost and downtime of mission capable aircraft.

1.2 Vibration Based Structural Health Monitoring

As stated by Farrar and Worden [1], "damage" can be defined as changes introduced into a system that adversely affect its current or future performance, including changes to the boundary conditions or system connectivity. Figure 1-1 illustrates the many different kinds of damage, their associated sizes that can occur in a typical aerospace structure. In terms of size, damage is typically considered to start at the material level, or "microscale." This material defect manifests as material voids, or dislocations. In contrast, at the "macroscale" level damage is seen as fatigue cracks, or holes from ballistic impacts. Regardless of the scale at which damage occurs, monitoring the initiation and propagation of damage is an important concern for health monitoring systems. If damage propagates to a critical size between scheduled inspections, it leaves the structure vulnerable to failure. Health monitoring systems are application dependant; while some work well detecting ballistic impacts, these same techniques may not be applicable to detecting material voids. For an SHM system to have the best performance, the scale at which it operates must be chosen carefully.

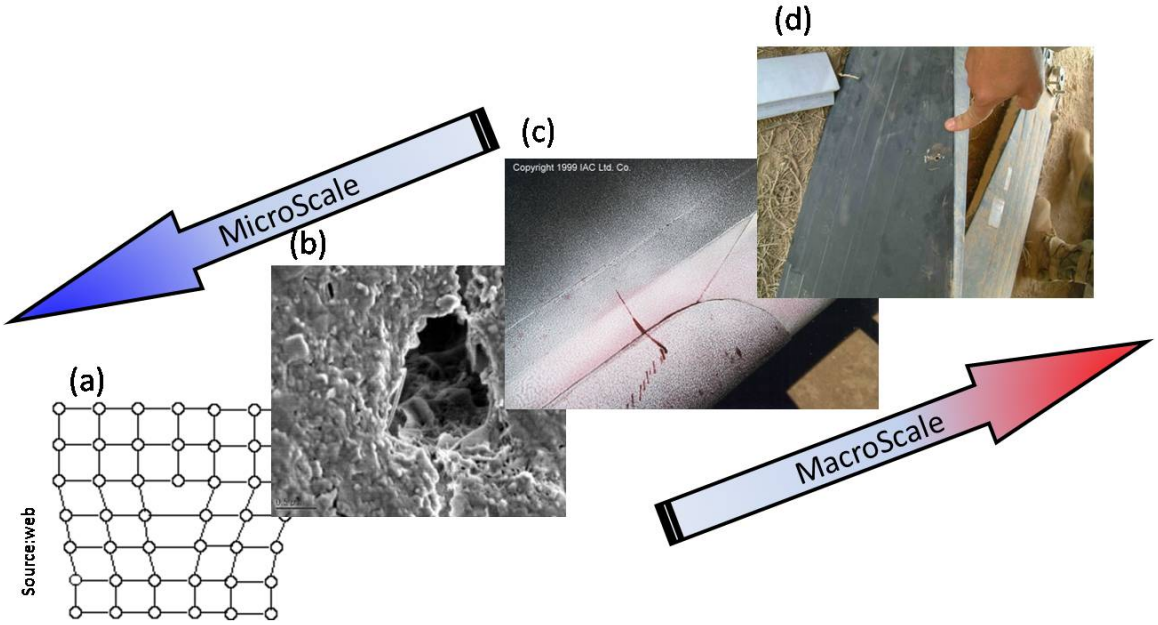

Figure 1-1: Schematic showing the impact of the damage length scales across a wide variety of aerospace structures. (a) dislocation, (b) void into the material, (c) fatigue crack on the leading edge of a rotor blade, (d) ballistic impact of a rotor blade. Damage initiation/propagation is also a very important factor in SHM detection parameters [14]

The goal of vibration based SHM is to detect damage at the component/substructure level. Achieving this goal would enable an easier transition from the schedule-based maintenance methods currently in practice to a more unified CBM approach. One of the easiest ways to implement a CBM approach is to track the vibration response of a structure over time, as all aircraft vibrate during normal operation. Monitoring for changes in the response can be accomplished using readily available and widely understood sensors such as strain gages and accelerometers. This technique has seen heavy use in rotating machinery diagnostics [2], rotorcraft drive systems [3], and is currently one of the main techniques used to monitor offshore wind turbines in Europe.

More recently, the focus of vibration-based health monitoring techniques has shifted towards detection based on structural dynamic changes. Differences in modal parameters such as shifts in natural frequencies, modal damping values, or modes shapes are functions of

the system mass, stiffness, and damping (physical parameters). Changes due to damage in the structure lead to changes in these modal parameters corresponding to the damage extent [4]. Many different systems and metrics that incorporate these methods exist currently (see References [4-6]), and while they can successfully detect global damage in structures, they show room for increased sensitivity to detect smaller damage features. Additionally, these systems lack the ability to localize damage. The need for an SHM system that has a higher sensitivity and can localize damage has sparked development in several technologies including the use of structural intensity. In their nonlinear formulation, these high sensitivity methods rely on the acoustic phenomenon known as contact acoustic nonlinearity.

1.3 Introduction to Contact Acoustic Nonlinearity (CAN)

When non-bonded surfaces come into contact, a unique type of nonlinear acoustic signature is produced, known as a Contact Acoustic Nonlinearity (CAN). The interaction of elastic waves at closing cracks is an acoustic phenomenon that is well understood, and has been extensively studied in the past [7-10]. CAN is a complicated physical mechanism, and the particular type of contact at the damage location can be related to the local opening and closure motion of the interface (a ‘clapping’ mechanism). The damage interface acts as a nonlinear scatter in an otherwise linear elastic system (a healthy structure).

CAN is assumed to be associated with the lack of symmetric stiffness across the contact interface (Figure 1-2). Under compression, the material elasticity is higher than when subjected to tensile stress, and in its simplest form can be represented by a bilinear stiffness model. This model approximates the behavior of the “clapping” mechanism that occurs with CAN.

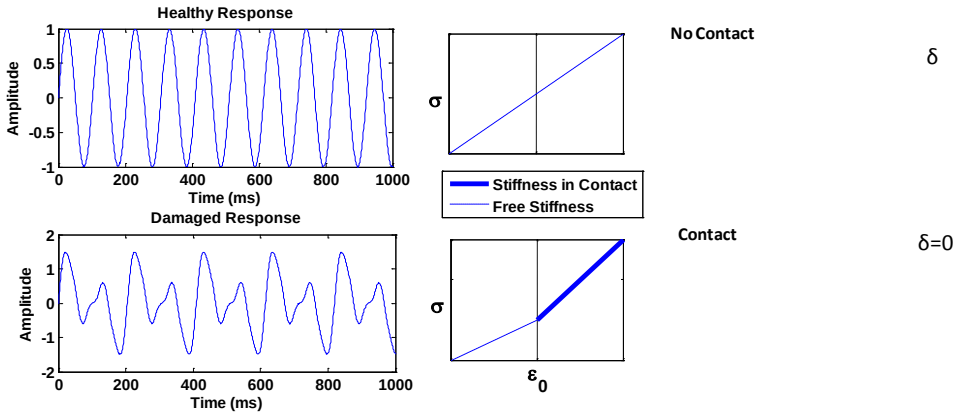

Figure 1-2: Contact Acoustic Nonlinearity schematic. When damaged, CAN is modeled as a bilinear stiffness model where ε_0 defines the initial static contact strain. As the phenomenon occurs, nonlinear harmonics appear in the response. Compression stiffness is assumed to be higher than the tensile stiffness due to the loss of contact between the two surfaces under excitation.

For example, a closed crack under the initial contact strain ε_0, and driven with a harmonic excitation strong enough to excite the nonlinear contact can be approximated as by Equation (1.1).

$$\sigma = E(1 + \delta(\varepsilon_0)\Delta E/E)\varepsilon \tag{1.1}$$

This piece-wise stress-strain relation (where $\delta(\varepsilon_0)$ is simply a unit step function) provides an estimation of the asymmetrical dynamics that are occurring at the contact interface [11]. When the two interfaces are in contact, the system is assumed to have a stiffness E (bold blue line). When the strain is less than ε_0, contact is lost between the two interfaces, and the system has a lower overall stiffness in tension (dotted blue line). This same bilinear stiffness behavior can occur at "closed" cracks as well, such as those pressed together by residual stress in a structure, fused by corrosion, or in delaminated composite materials.

A healthy structure will behave in a linear manner, and display none of the nonlinear content present in a damaged system. As damage is introduced, energy from the driving frequency is redistributed into nonlinear harmonics. These harmonics appear as fractional

bifurcations of the sub-harmonic frequencies, and integer multiples of the driving frequency resulting from a single tone excitation (Figure 1-3). In reality, the damage feature that will create these nonlinear harmonics is very complicated, and can be considered to behave similar to a set of coupled nonlinear oscillators [11]. The super-harmonic response is created as a result of the resonance properties of the oscillating system. The sub- and ultra-subharmonic response is only indicative of the local defect "resonance" effect, and is created as the system transitions to the region of parametric resonance.

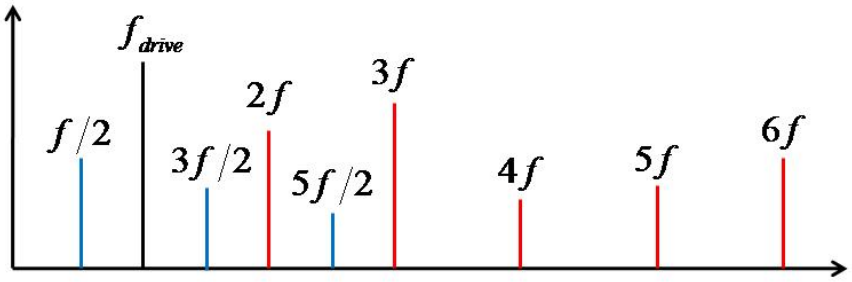

Figure 1-3: Illustration of the damaged structural response in the frequency domain under a single tone harmonic excitation. Note the presence of both super-harmonics (red) and ultra-subharmonics (blue) in the response.

Conventional linear techniques for non destructive evaluation (NDE) ignore the presence of nonlinear harmonics, and overlook the high sensitivity detection strength nonlinear features offer. For example, because damage such as closed cracks and delaminations have higher coefficients of transmissibility, the reflected wave from the drive frequency will be weaker, and linear techniques relying on amplitude changes in this interrogation signal will be even less sensitive to these types of damage characteristics [14]. CAN's unique nonlinear signature allows for new health monitoring techniques to utilize the response, offering a level of sensitivity not demonstrated by traditional linear methods.

Instead of relying on linear detection metrics, the nonlinear harmonic response generated by the dynamic excitation of these cracks can be used as a detection feature. Utilizing the sub-

harmonic response ($nf/2$) allows for "baseline-free" detection; the nonlinear response only appears when damage is present in the system, and will not be present in a healthy structure. This response has a high degree of sensitivity, but is very difficult to activate, requiring judicious selection of frequency and amplitude for the driving condition. Utilizing the super-harmonic response (nf), it is still possible to detect damage. However, due to harmonic distortion of the drive signal present in almost all experimental drive systems, this technique requires a healthy baseline measurement. Practically, using this response is much easier, if somewhat less sensitive, as it is less sensitive to the driving condition.

A variety of different interrogation methods can be used to activate the CAN phenomenon, including a single tone harmonic excitation. Under a single tone excitation, many nonlinear harmonics are produced as damage is introduced into the system. However, the unique acoustic signature created by a closed crack at its interface is a sub-harmonic wave at multiples of half the interrogation frequency ($f/2$, $3f/2$, $5f/2$, etc.). Additionally, integer multiples of the driving frequency (nf) will be present as well. These higher order harmonics are indicative of damage, but are less sensitive in experimental settings due to harmonic distortion effects in the drive system. Because the key damage indicative response of CAN is the nonlinear fractional bifurcation of the sub-harmonic frequencies ($nf/2$), health monitoring using CAN sub-harmonic-based features is ideal for use in a high sensitivity detection algorithm.

CAN displays a high instability sub-harmonic behavior which can be described as a parametric resonance. The presence of sub-harmonic frequencies indicates the transition to a region where the nonlinear effects become unstable [10, 11]. When activated via single tone harmonic excitation, the parametric resonance displays a nonlinear hysteretic behavior. Unlike a typical linear hysteresis behavior, amplitude changes when increasing are not equivalent to those when decreasing. Once the potential energy needed to activate the nonlinearity is overcome, the kinetic energy needed to keep the system in motion is significantly lower (Figure 1-4). The end

result of this behavior is a step-like sub-harmonic response as the driving force is increased, and a roll-off sub-harmonic response as the drive force is decreased. This behavior is common in highly nonlinear systems, and is due to the difference in phase of the two contact surfaces.

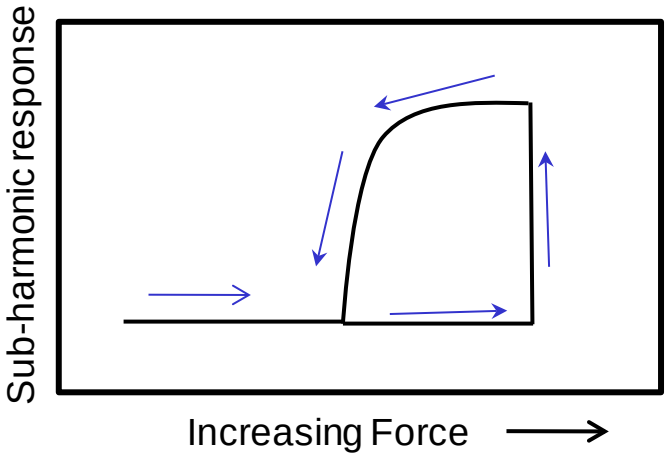

Figure 1-4: Illustration of the hysteretic behavior seen as CAN is activated by a single tone harmonic excitation

In addition to classical nonlinear methods that rely on a single tone excitation, various techniques relying on Nonlinear Elastic Wave Spectroscopy (NEWS), specifically Nonlinear Wave Modulation Spectroscopy (NWMS) have been used to greatly increase detection of similar nonlinear features due to fatigue cracking [12, 13]. Under a modulated wave excitation, the nonlinear response signature is more complex; wave interactions are combinations of the two interrogation frequencies. This interaction gives rise to nonlinear wave effects generated by the hysteretic behavior of the damage interface. These effects require a higher order model of the changing elastic modulus which incorporates the combination of the classical nonlinear behavior, as well as the corresponding hysteretic nonlinearity. This can be described by Equation (1.2).

$$E(\varepsilon, \dot{\varepsilon}) = E_0\{1 - \beta\varepsilon - \delta\varepsilon^2 - \alpha[\Delta\varepsilon + \varepsilon(t)\text{sign}(\dot{\varepsilon}) + \cdots]\} \quad (1.2)$$

Here, E_0 represents the undamaged linear elastic modulus of elasticity. β and δ represent the second and third order nonlinearity coefficients which appear as a result of a Taylor series expansion of the stress-strain relation, $\Delta\varepsilon$ is the local strain amplitude, and α represents a material hysteresis factor taking into account the history of both stress and strain. The term $\text{sign}(\dot{\varepsilon})$ is simply +1 if the strain rate $\dot{\varepsilon}$ is positive, or -1 if it is negative [12]. By interrogating using two sine waves (low frequency f_{low} , high frequency f_{high}), the higher frequency wave amplitude will be modulated with the low frequency. The low frequency tone acts as the "exercising" force which sets the two surfaces in motion, and the high frequency tone acts as a "carrier" wave, which activates the local parametric resonance. In the frequency domain, the modulations of the two waves occur as "sidebands." These combinations of the two interrogation frequencies are indicative of damage (Figure 1-5). The first order sidebands present in the response spectrum (f_+ , f_-) represent a classical nonlinearity in many systems. The higher order combinational tones ($f_{2,3+}$, $f_{2,3-}$) represent the hysteretic nonlinearity of the structure [13].

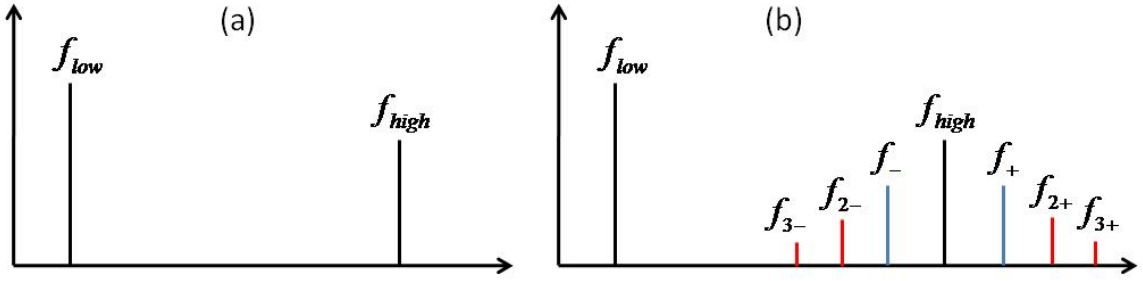

Figure 1-5: Illustration of the structural response in the frequency domain for the (a) healthy and (b) damaged conditions under a modulated wave excitation. Note (b) shows the presence of both classical (blue) and hysteretic nonlinearity (red) in the response.

There are several tradeoffs between both interrogation methods (CAN using sub-harmonic response vs. NWMS) used for health monitoring of fatigue cracks. Detection of CAN sub-harmonic response via single tone harmonic excitation is extremely sensitive *because* of the high instability of the associated parametric resonance. However, this instability may make

detection using sub-harmonic CAN-based features difficult to measure outside of a laboratory setting, even with prior knowledge of how the structure behaves. Finding the ideal driving condition to trigger the nonlinear response of the damage feature local "resonance" requires careful selection of both frequency and amplitude, and could be easily missed simply due to the highly unstable nature of the physical mechanism. Using NWMS to interrogate a structure is a much more stable interrogation method because it does not rely on the parametric resonance and associated self-modulation of a single wave to detect damage. The stability of this interrogation technique may lend itself better to use in a semi- or fully automated SHM system.

1.4 Introduction to Intensity Based Health Monitoring Techniques

Originally implemented by Noiseaux [15] and Pavic [16] in the late 1970's, Structural Intensity (SI) is defined as the mechanical power flow per unit area (stress multiplied by the complex conjugate of velocity) in a vibrating structure. SI is a vector quantity, and can be determined by using several different methods. Strain gages, accelerometers, or even laser vibrometer velocity measurements at various locations on a structure can be used to determine the energy flow through the entire structure. Taking the divergence of the intensity field allows for localization of energy sources and sinks. In addition, by tracking the changes in magnitude and phase over time, SI can be used as a powerful tool for visualizing damage present in a system.

Recent work by Conlon, Semperlotti et al. [17] showed the use of Structural Intensity (SI) and Nonlinear Structural Intensity (NSI) as health monitoring techniques for rotorcraft airframe structures by exploiting the nonlinear behavior of fatigue cracks. Linear SI relies on determining the energy flow present in a structure from only the driving (source) frequencies. In a healthy structure, no nonlinear contact "sources" are present, and the SI field would simply show energy flowing from sources (driving locations) to sinks (dissipation locations). When damage is

present, the “breathing” effects lead to energy spilling over from the driving frequency to nonlinear harmonics generated by the “clapping” mechanism present at the damage location. By exploiting the information present in these harmonics, Nonlinear Structural Intensity (NSI) can be processed at each harmonic, and the “virtual source” present from energy injected into the system can be localized at the damage location using either sub- or super harmonic frequencies.

To allow examination of the CAN effect using intensity based damage detection techniques, a heavy steel fixture was designed for use with an aluminum stiffened plate. This fixture provided stable boundary conditions for the panel and allowed for the use of a scanning laser vibrometer, as well as discrete sensors to characterize the flow of energy in the healthy / damaged structure. NSI visualization was applied to the aluminum stiffened panel test bed with damage introduced as loose fasteners connecting the plate to the stiffener. When actively excited using a single frequency drive, the healthy condition exhibits none of the characteristic nonlinear behavior present with the damaged condition. Data was processed using a finite differencing scheme developed by Schmidt [18] to obtain the necessary estimated special derivatives for the NSI calculation. NSI maps and their corresponding divergence fields for an excitation frequency f_e = 706Hz are presented in Figure 1-6 [19].

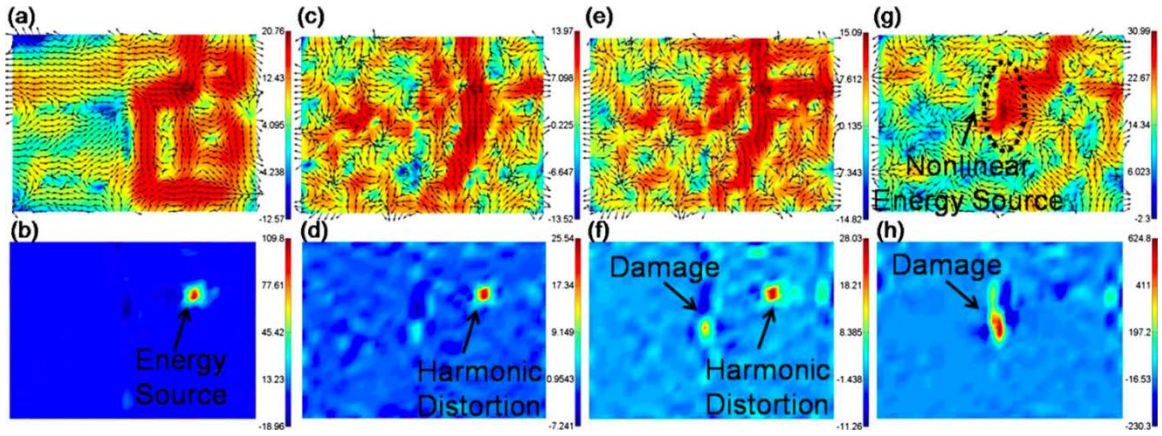

Figure 1-6: (a) SI map and (b) divergence plot at the driving frequency f_e=706 Hz for the healthy plate. SI map and divergence plot at $2f_e$=1412 Hz for the (c) and (d) healthy, (e) and (f) one-row, and (g) and (h) two-row damage conditions. The divergence plots show that energy is injected into the plate at the damage location due to the nonlinear contact with the stiffener [19].

In the healthy configuration, no nonlinear contact is present, and the SI field is simply reverberant. At the first damage increment evaluated at the first super-harmonic frequency, a small nonlinear energy source can be localized at the damage location, but harmonic distortion of the drive signal obscures the resultant signature. This source due to the CAN is more clearly visible at the second damage increment, and the divergence plot clearly identifies the damage location. Harmonic distortion is still present for the two-row condition, but is obscured by the magnitude of the "source" due to damage.

While NSI is a useful technique for visualizing damage, it is not easily applied to realistic airframe structures due to the difficulty of obtaining accurate velocity measurements on complex geometries. In addition, the original SI formulation is only valid for structures that meet thin plate theory assumptions (isotropic, thickness small compared to lengthwise dimensions). To overcome this, intensity methods were later developed on more complex structures [20] utilizing Structural Surface Intensity (SSI). Unlike its counterpart SI, which uses information at discrete locations over the entire structure surface to visualize the flow of energy, SSI is only representative of the energy flow at the free surface, and at the measurement location.

Semperlotti, Conlon et al. [21] recently extended the concept of Structural Surface Intensity (SSI) into the nonlinear domain. This quantity, Nonlinear Structural Surface Intensity (NSSI), is formulated for mechanical systems whose response is governed by nonlinearity due to the CAN effect. NSSI provides an increased sensitivity to structural flaws which are difficult to detect with conventional linear techniques while still holding a physical meaning related to energy flow [17]. Similar to SSI in the linear domain, NSSI also uses multiple measurements (two velocities and three strains – Figure 1-7) combined into one metric or feature

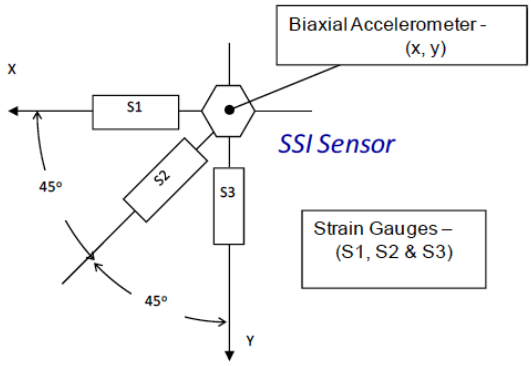

Figure 1-7: SSI sensor suite, including 3 PZT strain sensors in a rectangular rosette configuration, and a biaxial accelerometer. Acceleration signals are numerically integrated to provide velocities needed for the SSI calculation [16].

The nonlinear vibration response associated with the presence of a contact acoustic nonlinearity makes NSSI an ideal high sensitivity metric to use for SHM methods. Three discrete SSI measurement suites were used to exploit the presence of energy at sub-harmonic frequencies, localizing and sizing the response due to damage. As the damage feature size increased the relative amplitude of the sub-harmonics created by the CAN were expected to increase accordingly, exhibiting a monotonic trend [17]. The acquired acceleration signals were numerically integrated to yield velocity, and strain rosette response was used to estimate the shear strain [22]. Since no sub-harmonics are present in the healthy condition (no nonlinear vibration mechanisms present), NSSI is considered to be a baseline-free metric (Figure 1-8). The final

velocity and strain signals were used to yield an NSSI estimate, which exhibited a monotonic trend as damage size increased, as predicted (Figure 1-9). This confirms that NSSI is a metric very sensitive to damage size, and is a more robust damage detection feature than other metrics using a linear approach.

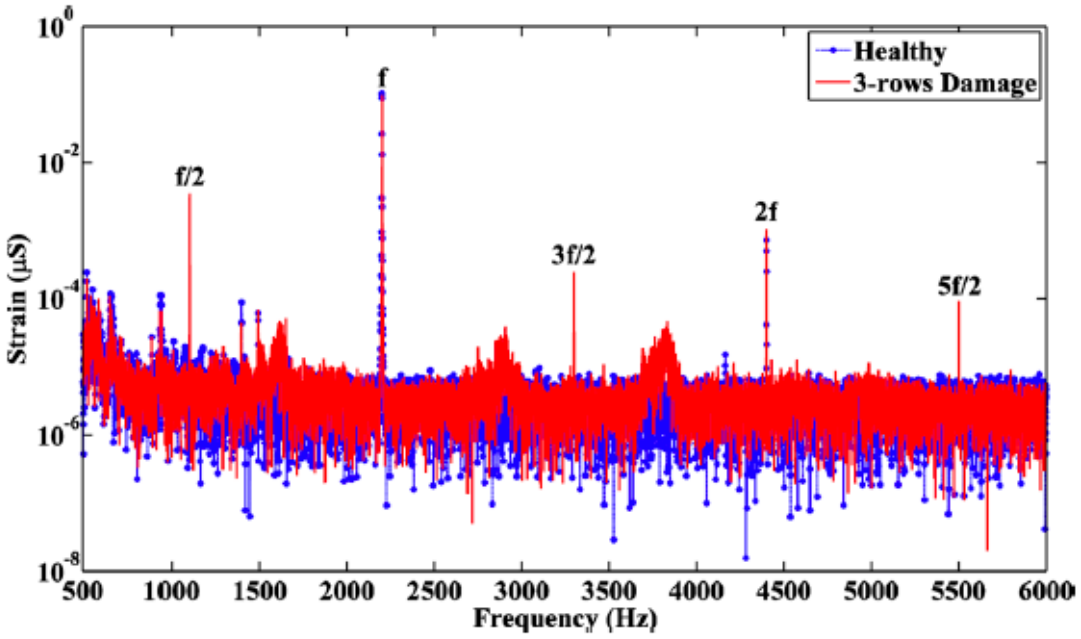

Figure 1-8: Frequency spectra of strain history collected on the experimental test setup (sensor at 45 degrees) for the healthy and three-rows loose damage configuration. Sub- and ultra-subharmonics are clearly visible in the damaged spectral response. Note that the healthy response also contains 2f content due to harmonic distortion present in the drive system. [21]

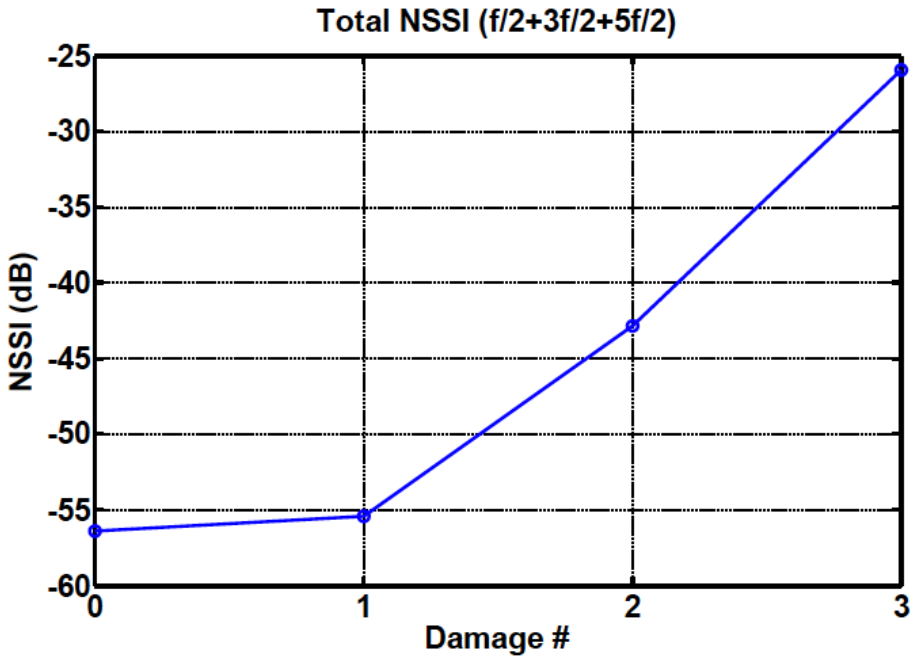

Figure 1-9: Stiffened panel experimental relation between total NSSI and damage size. Increment #0 refers to the healthy condition while #1-3 refers to the damage configuration in number of bolt rows loose. Results prove the NSSI feature is a monotonic function with respect to the damage extent [17]

1.5 Objectives and Thesis Outline

1.5.1 Research Objectives

The main focus of this thesis is to investigate contact acoustic nonlinearity characteristics in damaged structures, develop structural intensity-based damage detection approaches that key off CAN effects, and evaluate the performance of the techniques as they are applied to relevant metallic and composite airframe structures.

Specific objectives that meet this overall goal are to:

1. Design and develop a variety of experimental test beds to allow examination of the active energy flow in plate structures via intensity-based damage detection techniques.

2. Study CAN effects on energy flow in damaged structures by using NSI visualization at sub-harmonic frequencies to determine how the nonlinear phenomenon manifests with relevant damage types and sizes.
3. Fully understand the behavior of contact acoustic nonlinearities by examining hysteresis effects to provide insight into interrogation signal design and how the technique could be implemented into an automated SHM system.
4. Evaluate the detection strength and stability of a new approach utilizing modulated wave interrogation, NSSI-MW, and compare the new metric's effectiveness to the single tone interrogation approach.
5. Transition the methods developed on isotropic metal plates and extend them to composite materials to provide performance insight for applications on more complex airframe structures with varying degrees of damping
6. Transition each intensity-based SHM technique to a complex airframe structure to examine the effectiveness of each metric.

1.5.2 Outline and Organization

This thesis is divided into six chapters. A technical approach is presented in Chapter 2 of this thesis, including the theoretical background and development of all structural intensity methods, and a description of each experimental test bed. First, a brief review of structural intensity in plates is presented. In this section, the finite difference-based algorithms for determining SI experimentally are developed. Following this, the formulation for SSI and NSSI is reviewed, and each test bed is described in detail. In Chapter 3, results of NSI and NSSI are reviewed for several test cases on the aluminum stiffened panel and

composite panel test beds. In Chapter 4, the new hybrid technique, NSSI-MW, is evaluated for effectiveness, and the effect different interrogation signals have on CAN hysteresis is presented. In Chapter 5, an OH-58 tail boom was as used a development structure to evaluate the performance of each metric and their effectiveness on a complex airframe structure with realistic damage. Finally, a summary of all research results and recommendations for future work is presented in Chapter 6.

Chapter 2

Technical Approach

2.1 Introduction

In this chapter, several intensity-based methods for structural health monitoring, and their application to a variety of test beds are discussed. The approach taken for the development of each detection technique used a “stepping stone” path to make the transition to more complex structures easier. Each method was evaluated starting with an aluminum stiffened panel, complexity was added by moving to composite stiffened panels with higher distributed damping, and each surface intensity technique was ultimately tested on a tail boom from an OH-58 Kiowa Warrior (a real, complex airframe structure).

Each SI measurement technique relies on frequency response data post processed by MATLAB codes to obtain the necessary spectral quantities needed for each calculation. Fortunately, data in the frequency domain is relatively simple to obtain and well understood. Standard instrumentation such as strain gages and accelerometers were used to acquire time histories, which were then post processed into the frequency domain according to well known signal analysis theories [23].

A review of previously developed intensity formulations is presented here, which provide insight into potential advantages of using intensity-based metrics in structural health monitoring systems over those that are currently in place within the aerospace industry. Intensity-based damage detection can be broken down into two parts: Structural Intensity (SI), which uses information at a variety of discrete points over the entire structure to help visualize energy flow path, and Structural Surface Intensity (SSI), which relies on information at a single sensor

location to determine the energy flow on the free surface of the structure. Each of these methods has a nonlinear counterpart, denoted Nonlinear Structural Intensity (NSI), and Nonlinear Structural Surface Intensity (NSSI). In addition, a new technique was developed that relies on Nonlinear Wave Modulation Spectroscopy (NWMS). Referred to as Nonlinear Structural Surface Intensity – Modulated Wave (NSSI-MW), this method was developed to determine the metric's effectiveness in evaluating damage characteristics. These detection results can be compared to the single tone approach to see if the technique was potentially easier to implement in an automated SHM system.

In order to successfully evaluate the overall effectiveness of each metric presented in this chapter, a complete understanding of the theoretical background for each technique is required. Formulations for SI and NSI are highlighted in Section 2.2, including the required finite difference formulas needed for the experimental SI calculation. Similarly, the development for SSI and NSSI is reviewed in Section 2.3. Additionally, Section 2.3 provides the theoretical background and development for NSSI-MW. Lastly, a detailed description of the test beds used to evaluate the relative effectiveness of each measurement technique is provided in Section 2.4.

2.2 Structural Intensity (SI) and Nonlinear Structural Intensity (NSI) Methods

Originating in the noise and vibration control communities, intensity measurements were initially applied in airborne acoustic power flow studies [24]. As these techniques advanced, they were applied to structures as well. While a variety of different ways exist to calculate structural intensity, this work focused on measuring SI with finite differencing techniques via thin plate theory. The development of the original SI formulation according to thin plate theory from Pavic [16] is presented in the first part of this section. Following this, NSI as developed by Conlon, Semperlotti et al. [19] is reviewed.

Recently, several authors have focused on measuring structural intensity in thin plates. Work by Arruda and Mas [25] and later continued by Daley [26] demonstrated that in plates conforming to thin plate theory assumptions, structural intensity (neglecting rotational inertia and shear deformation) can be formulated as follows.

Classical thin plate theory gives the bending wave equation for a thin plate to be

$$D\nabla^2\nabla^2 w(x,y,t) + \rho h \frac{\partial^2(x,y,t)}{\partial t^2} = F(t)\delta(x_0,y_0) \tag{2.1}$$

where $D = \frac{Eh^3}{(1-\upsilon)}$ is the flexural stiffness, E is the material Young's modulus, υ is Poisson's ratio, h is the plate thickness, $w(x,y,t)$ is the transverse displacement, ρ is the material density, and $F(t)\delta(x_0,y_0)$ is the applied force at a given point [27]. Figure 2-1 shows a differential thin plate element to which this equation can be applied.

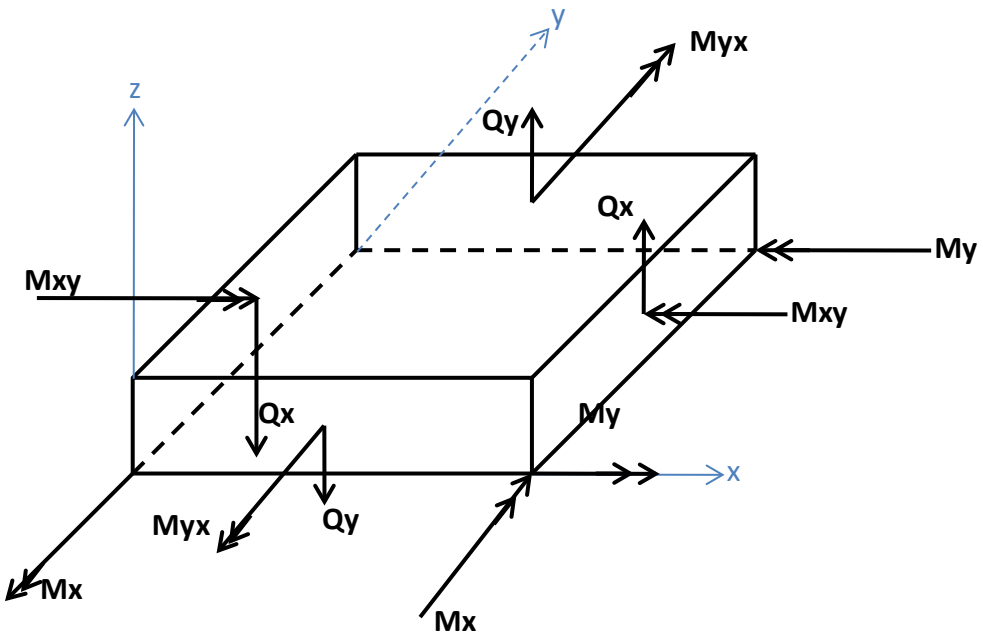

Figure 2-1: Free body diagram of a thin plate element showing the assumed force, moment, and shear vector orientations

For thin plates, the moments and shear forces per unit length can be written as:

$$M_x = \widetilde{D}\left(\frac{\partial^2 w}{\partial x^2} + \upsilon\frac{\partial^2 w}{\partial y^2}\right) \tag{2.2}$$

$$M_y = \widetilde{D}\left(\frac{\partial^2 w}{\partial y^2} + \upsilon\frac{\partial^2 w}{\partial x^2}\right) \tag{2.3}$$

$$M_{xy} = M_{yx} = \widetilde{D}(1-\upsilon)\frac{\partial^2 w}{\partial x \partial y} \tag{2.4}$$

$$Q_x = \widetilde{D}\frac{\partial}{\partial x}(\nabla^2 w) = \widetilde{D}\left(\frac{\partial^3 w}{\partial x^3} + \frac{\partial^3 w}{\partial x \partial y^2}\right) \tag{2.5}$$

$$Q_y = \widetilde{D}\frac{\partial}{\partial y}(\nabla^2 w) = \widetilde{D}\left(\frac{\partial^3 w}{\partial y^3} + \frac{\partial^3 w}{\partial y \partial x^2}\right) \tag{2.6}$$

To incorporate the effect of material damping losses, the flexural rigidity constant is expressed as a complex quantity $\widetilde{D} = D(1 - i\eta)$ where D is the real part and η is the material loss factor [26].

Vibrational energy in structures propagates mainly through two basic wave types: compression and shear. Depending on the physical characteristics of the structure, these can combine into more complex forms as bending, torsional, and longitudinal waves. For thin plates, bending waves are largest component, and are usually responsible for most of the energy at the structure surface. Typically, the reactive vibration component (standing waves) part is very large, and the active part (net energy flow) is very low. Knowing this, the total structural intensity vector in a thin plate is the vector sum of each component part (bending, twisting, shear) in both the x and y direction, given as [25]:

$$I_x = \frac{\langle Q_x \dot{w}\rangle_t + \langle M_x \dot{\theta}_y\rangle_t - \langle M_{xy}\dot{\theta}_x\rangle_t}{h} = I_x^s + I_x^b + I_x^t \tag{2.7}$$

$$I_y = \frac{\langle Q_y \dot{w}\rangle_t - \langle M_y \dot{\theta}_x\rangle_t + \langle M_{xy}\dot{\theta}_y\rangle_t}{h} = I_y^s + I_y^b + I_y^t \tag{2.8}$$

where each superscript *b*, *s*, *t*, denotes the bending, shear, and twisting component respectively. Additionally, $\langle ... \rangle_t$ denotes a time averaged quantity, *h* the plate thickness, and the plane rotation angles are $\Theta_x = \frac{\partial w}{\partial y}$, $\Theta_y = \frac{\partial w}{\partial x}$ and $\dot{\Theta} = \frac{\partial w}{\partial t}$. Lastly, the time derivative $\dot{w}$ represents the out of plane velocity of the plate at any given point.

Substituting the expressions in Equations (2.2)-(2.6) into Equations (2.7) and (2.8), the final six components of structural intensity can be written analytically in terms of acceleration (second time derivative $\ddot{w}$) as

$$I_x^s - \frac{D}{h}\langle \frac{i}{\omega^3}(1-i\eta)(\frac{\partial^3 \ddot{w}}{\partial x^3} + \frac{\partial^3 \ddot{w}}{\partial x \partial y^2})\ddot{w}\rangle_t \tag{2.9}$$

$$I_y^s = -\frac{D}{h}\langle \frac{i}{\omega^3}(1-i\eta)(\frac{\partial^3 \ddot{w}}{\partial y^3} + \frac{\partial^3 \ddot{w}}{\partial y \partial x^2})\ddot{w}\rangle_t \tag{2.10}$$

$$I_x^b = \frac{D}{h}\langle (1-i\eta)\frac{1}{\omega^3}\left(\frac{\partial^2 \ddot{w}}{\partial x^2} + \frac{1}{\upsilon}\frac{\partial^2 \ddot{w}}{\partial y^2}\right)\left(i\frac{\partial \ddot{w}}{\partial x}\right)\rangle_t \tag{2.11}$$

$$I_y^b = \frac{D}{h}\langle (1-i\eta)\frac{1}{\omega^3}\left(\frac{\partial^2 \ddot{w}}{\partial y^2} + \frac{1}{\upsilon}\frac{\partial^2 \ddot{w}}{\partial x^2}\right)\left(i\frac{\partial \ddot{w}}{\partial y}\right)\rangle_t \tag{2.12}$$

$$I_x^t = -\frac{D}{h}(1-\upsilon)\langle (1-i\eta)\frac{1}{\omega^3}\frac{\partial^2 \ddot{w}}{\partial x \partial y}\left(i\frac{\partial \ddot{w}}{\partial y}\right)\rangle_t \tag{2.13}$$

$$I_y^t = -\frac{D}{h}(1-\upsilon)\langle (1-i\eta)\frac{1}{\omega^3}\frac{\partial^2 \ddot{w}}{\partial x \partial y}\left(i\frac{\partial \ddot{w}}{\partial x}\right)\rangle_t \tag{2.14}$$

It is important to remember this formulation is only valid for structures conforming to the thin plate theory assumptions. For structures with more complex geometries, these assumptions are not valid, and the energy flow cannot be mapped accurately using this formulation.

To implement this specific SI measurement method, a matrix of acceleration cross-spectra is needed. This matrix can be determined using the well known Multiple Input/Multiple Output system theory [23]. The response cross spectra matrix can be determined from the triple matrix equation

$$G_{\ddot{w}_i\ddot{w}_j} = H^{'*}_{\ddot{w}_{pi}} G_{pp} H_{\ddot{w}_{pj}} \tag{2.15}$$

where $H_{\ddot{w}_{pi}}$ and $H_{\ddot{w}_{pj}}$ represent the transfer function matrix between any arbitrary input point *i* or *j* and the driving point *p*, and H'^{*} represents the complex conjugate transpose. In this case, only a single point excitation is used, and the resulting cross spectra between two time signals *x(t)* and *y(t)* is

$$G_{xy}(f) = \frac{1}{2} X^{*}(f) Y(f) \tag{2.16}$$

where $X^{*}(f)$ and $Y(f)$ represent the complex amplitudes of *x(t)* and *y(t)* in the frequency domain.

Having determined the cross-spectra matrix, the spatial derivatives at any point on the plate can be determined by using finite difference approximations to a high degree of accuracy. Due to the nature of the central finite differencing grid, it is necessary on plate structures to separate into 9 regions to fully estimate SI at every point (Figure 2-2). If only central differencing is used, the SI field will artificially go to zero at the edges. To avoid this, combinations of forward, backward, and central differencing is used are used in the outlying edge regions. For region 5, only central differencing is needed to fully estimate all derivatives.

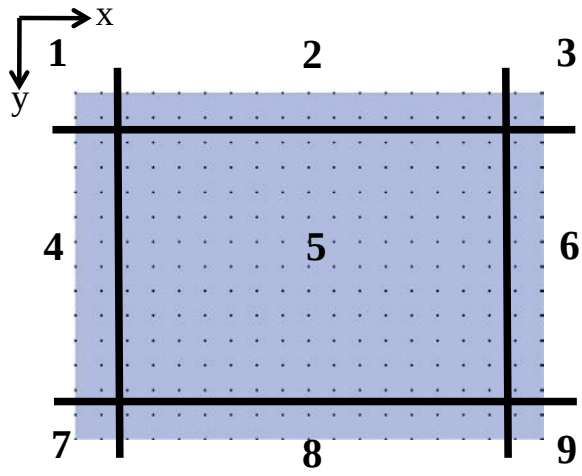

Figure 2-2: Required region separation of plate structures for which different combinations of central, forward, and backward differencing were used to estimate plate SI at every grid point.

Following the technique described by Daley [26], arrays used for the SI calculation are different for each region, and are presented in Reference [28]. A full derivation of the shear intensity component in the y direction for region 5 is described below, as Reference [18] and [26] contain sign and typographical index errors in their formulation. Similar methods can be used to derive the equations in each direction for their respective component (bend, twist, shear). The resultant formulations for each intensity component in region 5 (central-central) are listed following the derivation. For brevity, the derivation for the finite differencing formulas in other regions is not described, but each the final result of each component is listed in Appendix C

By using a Taylor series expansion, any arbitrary function $w = f(x)$ at $(x_i + \Delta x)$ and $(x_i - \Delta x)$ can be written as:

$$w(x_i + \Delta x) = w_i + w_i^{'}\Delta x + \frac{w_i^{''}\Delta x^2}{2!} + \frac{w_i^{'''}\Delta x^3}{3!} + \cdots \tag{2.17}$$

$$w(x_i - \Delta x) = w_i - w_i^{'}\Delta x + \frac{w_i^{''}\Delta x^2}{2!} - \frac{w_i^{'''}\Delta x^3}{3!} + \cdots \tag{2.18}$$

Subtracting Equation (2.17) from (2.18) gives:

$$w_i^{'} = \frac{w(x_i + \Delta x) - w(x_i - \Delta x)}{2\Delta x} - (\frac{1}{6}w_i^{'''}\Delta x^2 + \cdots) \tag{2.19}$$

Using equally spaced points to the left and right of x_i , Equation (2.19) can be written to order Δx^2 as

$$w_i^{'} = \frac{w_{i+1} - w_{i-1}}{2\Delta x} \tag{2.20}$$

Similarly, equations for higher order derivatives can be obtained by using 4 surrounding points

$$w_i^{''} = \frac{w_{i+1} - 2w_i + w_{i-1}}{\Delta x^2} \tag{2.21}$$

$$w_i^{'''} = \frac{w_{i+2} - 2w_{i+1} + 2w_{i-1} - w_{i-2}}{2\Delta x^3} \tag{2.22}$$

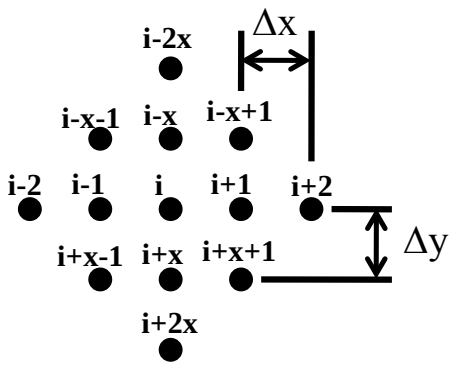

Figure 2-3: Array used to calculate SI at any point within region 5 on a plate. The SI vector at the center point (point #i) is calculated via finite differencing of the structural response matrix. *x* represents the number of points in the x-direction.

Following the convention of the central differencing grid shown in Figure 2-3, the third derivative (shear) of *w* in both the x and y directions can be estimated as

$$\frac{\partial^3 w}{\partial x^3} = \frac{w_{i+2} - 2w_{i+1} + 2w_{i-1} - w_{i-2}}{2\Delta x^3} \tag{2.23}$$

$$\frac{\partial^3 w}{\partial y^3} = \frac{w_{i+2x} - 2w_{i+x} + 2w_{i-x} - w_{i-2x}}{2\Delta y^3} \tag{2.24}$$

Now each component of intensity can be calculated with this approximation. Substituting Equation (2.6) into the first term of Equation (2.8), the shear component of intensity in the y-direction becomes

$$I_y^s = -\frac{D}{h}\langle \frac{i}{\omega^3}(1 - i\eta)(\frac{\partial^3 \ddot{w}}{\partial y^3} + \frac{\partial^3 \ddot{w}}{\partial y \partial x^2})\ddot{w}\rangle_t \tag{2.25}$$

Expanding with the finite difference approximations gives

$$I_y^s = \frac{-D}{\omega^3 h}\langle i(1 - i\eta)\left[\frac{(\ddot{w}_{i+2x} - 2\ddot{w}_{i+x} + 2\ddot{w}_{i-x} - \ddot{w}_{i-2x})\ddot{w}_i}{2\Delta y^3} + \frac{\left((\ddot{w}_{i+x-1} - \ddot{w}_{i-x-1}\right) - 2(\ddot{w}_{i+x} - \ddot{w}_{i-x}) + (\ddot{w}_{i+x+1} - \ddot{w}_{i-x+1}))\ddot{w}_i}{2\Delta y \Delta x^2}\right]\rangle_t \tag{2.26}$$

Rearranging

$$I_y^s = \frac{-D}{2\omega^3 h\Delta y}\langle i(1-i\eta)\left[\frac{\ddot{w}_{i+2x}\ddot{w}_\iota - 2\ddot{w}_{i+x}\ddot{w}_\iota + 2\ddot{w}_{i-x}\ddot{w}_\iota - \ddot{w}_{i-2x}\ddot{w}_\iota}{\Delta y^2}\right.$$
$$\left. + \frac{\ddot{w}_{i+x-1}\ddot{w}_\iota - w_{\iota-\ddot{x}-1}\ddot{w}_\iota - 2\ddot{w}_{i+x}\ddot{w}_\iota - 2w_{\iota-\ddot{x}}\ddot{w}_\iota + \ddot{w}_{i+x+1}\ddot{w}_\iota - w_{\iota-\ddot{x}+1}\ddot{w}_\iota}{\Delta x^2}\right]\rangle_t \quad (2.27)$$

Using Equation (2.16) to transform Equation (2.27) into the frequency domain gives

$$I_y^s = \frac{-D}{4\omega^3 h\Delta y} Im\left\{(1-i\eta)\left[\frac{\ddot{W}^*_{i+2x}\ddot{W}_\iota - 2\ddot{W}^*_{i+x}\ddot{W}_\iota + 2\ddot{W}^*_{i-x}\ddot{W}_\iota - \ddot{W}^*_{i-2x}\ddot{W}_\iota}{\Delta y^2}\right.\right.$$
$$\left.\left. + \frac{\ddot{W}^*_{i+x+1}\ddot{W}_\iota - \ddot{W}^*_{i-x-1}\ddot{W}_\iota - 2\ddot{W}^*_{i+x}\ddot{W}_\iota - 2\ddot{W}^*_{i-x}\ddot{W}_\iota + \ddot{W}^*_{i+x+1}\ddot{W}_\iota - \ddot{W}^*_{i-x+1}\ddot{W}_\iota}{\Delta x^2}\right]\right\} \quad (2.28)$$

where W^* represents the complex amplitude of the acceleration, and Im represents the imaginary part of the signal. Equation (2.28) can then be rewritten in terms of known cross spectra measurements as

$$I_y^s = \frac{-D}{2\omega^3 h\Delta y} Im\left\{(1-i\eta)\left[\frac{G_{\ddot{w}_{i+2x}\ddot{w}_i} - 2G_{\ddot{w}_{i+x}\ddot{w}_i} + 2G_{\ddot{w}_{i-x}\ddot{w}_i} - G_{\ddot{w}_{i-2x}\ddot{w}_i}}{\Delta y^2}\right.\right.$$
$$\left.\left. + \frac{G_{\ddot{w}_{i+x+1}\ddot{w}_i} - G_{\ddot{w}_{i-x-1}\ddot{w}_i} - 2G_{\ddot{w}_{i+x}\ddot{w}_i} - 2G_{\ddot{w}_{i-x}\ddot{w}_i} + G_{\ddot{w}_{i+x+1}\ddot{w}_i} - G_{\ddot{w}_{i-x+1}\ddot{w}_i}}{\Delta x^2}\right]\right\} \quad (2.29)$$

The remaining SI components for region 5 can be derived similarly, and are listed in Equations (2.30)-(2.34).

$$I_x^s = \frac{-D}{2\omega^3 h\Delta x} Im\left\{(1-i\eta)\left[\frac{G_{\ddot{w}_{i+2}\ddot{w}_i} - 2G_{\ddot{w}_{i+1}\ddot{w}_i} + 2G_{\ddot{w}_{i-1}\ddot{w}_i} - G_{\ddot{w}_i\ddot{w}_i}}{\Delta x^2}\right.\right.$$
$$\left.\left. + \frac{G_{\ddot{w}_{i+x+1}\ddot{w}_i} - G_{\ddot{w}_{i+x-1}\ddot{w}_2} - 2G_{\ddot{w}_{i+1}\ddot{w}_i} - 2G_{\ddot{w}_{i-1}\ddot{w}_i} + G_{\ddot{w}_{i-x+1}\ddot{w}_i} - G_{\ddot{w}_{i-x-1}\ddot{w}_i}}{\Delta y^2}\right]\right\} \quad (2.30)$$

$$I_x^b = \frac{D}{2\omega^3 h\Delta x} Im\left\{(1-i\eta)\left[\frac{(G_{\ddot{w}_{i+1}\ddot{w}_{i+1}} - 2G_{\ddot{w}_i\ddot{w}_{i+1}} + 2G_{\ddot{w}_{i-1}\ddot{w}_{i+1}})}{\Delta x^2}\right.\right.$$
$$- \frac{(G_{\ddot{w}_{i+1}\ddot{w}_{i-1}} - 2G_{\ddot{w}_i\ddot{w}_{i-1}} + G_{\ddot{w}_{i-1}\ddot{w}_{i-1}})}{\Delta x^2} \quad (2.31)$$
$$\left.\left. + \frac{1}{\upsilon}\frac{(G_{\ddot{w}_{i+x}\ddot{w}_{i+1}} - 2G_{\ddot{w}_i\ddot{w}_{i+1}} + G_{\ddot{w}_{i-x}\ddot{w}_i}) - (G_{\ddot{w}_{i+x}\ddot{w}_{i-1}} - 2G_{\ddot{w}_i\ddot{w}_{i-1}} + G_{\ddot{w}_{i-x}\ddot{w}_{i-1}})}{\Delta y^2}\right]\right\}$$

$$I_y^b = \frac{D}{2\omega^3 h\Delta y} Im\left\{(1-i\eta)\left[\frac{(G_{\ddot{w}_{i+x}\ddot{w}_{i+x}} - 2G_{\ddot{w}_i\ddot{w}_{i+x}} + G_{\ddot{w}_{i-x}\ddot{w}_{i+x}})}{\Delta y^2}\right.\right.$$
$$+\frac{-(G_{\ddot{w}_{i+x}\ddot{w}_{i-x}} - 2G_{\ddot{w}_i\ddot{w}_{i-x}} + G_{\ddot{w}_{i-x}\ddot{w}_{i-x}})}{\Delta y^2} + \frac{1}{v}\frac{(G_{\ddot{w}_{i+1}\ddot{w}_{i+x}} - 2G_{\ddot{w}_i\ddot{w}_{i+x}} + G_{\ddot{w}_{i-1}\ddot{w}_{i+x}})}{\Delta x^2} \quad (2.32)$$
$$\left.\left.+\frac{1}{v}\frac{-(G_{\ddot{w}_{i+1}\ddot{w}_{i-x}} - 2G_{\ddot{w}_i\ddot{w}_{i+x}} + G_{\ddot{w}_{i-1}\ddot{w}_{i-x}})}{\Delta x^2}\right]\right\}$$

$$I_x^t = \frac{-D(1-v)}{8\omega^3 h\Delta x\Delta y^2} Im\left\{(1-i\eta)\left[G_{\ddot{w}_{i+y}\ddot{w}_{i-x-1}} + G_{\ddot{w}_{i+x}\ddot{w}_{i+x+1}} - G_{\ddot{w}_{i+x}\ddot{w}_{i-x+1}} - G_{\ddot{w}_{i+x}\ddot{w}_{i+x-1}}\right.\right.$$
$$\left.\left. - G_{\ddot{w}_{i-x}\ddot{w}_{i-x-1}} - G_{\ddot{w}_{i-x}\ddot{w}_{i+x+1}} + G_{\ddot{w}_{i-x}\ddot{w}_{i-x+1}} + G_{\ddot{w}_{i-x}\ddot{w}_{i+x-1}}\right]\right\} \quad (2.33)$$

$$I_y^t = \frac{-D(1-v)}{8\omega^3 h\Delta y\Delta x^2} Im\left\{(1-i\eta)\left[G_{\ddot{w}_{i+1}\ddot{w}_{i-x-1}} + G_{\ddot{w}_{i+1}\ddot{w}_{i+x+1}} - G_{\ddot{w}_{i+1}\ddot{w}_{i-x+1}} - G_{\ddot{w}_{i+1}\ddot{w}_{i+x-1}}\right.\right.$$
$$\left.\left. - G_{\ddot{w}_{i-1}\ddot{w}_{i-x-1}} - G_{\ddot{w}_{i-1}\ddot{w}_{i+x+1}} + G_{\ddot{w}_{i-1}\ddot{w}_{i-x+1}} + G_{\ddot{w}_{i-1}\ddot{w}_{i+x-1}}\right]\right\} \quad (2.34)$$

In its linear form, SI is evaluated at only the driving frequency. In the nonlinear system however, the damaged response will redistribute energy from the driving frequency, which appears in the form of nonlinear harmonics present in the response spectra. To visualize this effect, SI can be evaluated at the nonlinear harmonic frequencies. This method is denoted Nonlinear Structural Intensity (NSI). The CAN phenomenon can be visualized by taking the divergence of the NSI vector field.

$$\text{div}(I) = \nabla(I) = \frac{\partial I_x}{\partial x} + \frac{\partial I_y}{\partial y} \quad (2.35)$$

The divergence of a NSI field will show only sources due to nonlinear contact when evaluated at sub-harmonic frequencies. If NSI is evaluated at super-harmonic frequencies, a weak source may be present at the drive location due to harmonic distortion of the drive signal.

2.3 Structural Surface Intensity (SSI) and Nonlinear Structural Surface Intensity (NSSI) Methods

While SI and NSI are both extremely valuable tools for visualizing damage present in systems, they are not easily applied to more complex geometries on three dimensional structures since the original formulation for SI is only applicable to idealized beam and plate structural elements. The complex geometries of realistic airframe structures are also difficult to scan, and materials commonly used within the aerospace industry (such as composites) have a low reflectivity, further complicating the experimental process. To overcome this, a more general SI formulation is needed to accommodate measurements on complex structures.

Pavic [20] originally formulated SSI as a discrete way to measure power flow per unit depth through beam and plate like-isotropic structures. With structures conforming to thin plate theory assumptions, it is possible to obtain measurements of pure mechanical power flow by simply integrating the measured surface intensity by the cross-sectional area. However, in more complex structures, such as anisotropic composite panels, this is not possible because the material properties are not constant through the thickness. The formulation of SSI presented here is only indicative of the energy flow at the free surface and measurement location, unlike its counterpart SI, which uses information at discrete locations over the entire structure surface to visualize the flow of energy.

Figure 2-4 shows a general elastic body subjected to an external dynamic force. Under plane stress conditions, the normal and tangential shear stress must be neglected ($\sigma_z = \tau_{zx} = \tau_{zy} = 0$), and the remaining intensity vectors will only be on the surface plane of the element. These vectors can be defined as

$$I_x^s = \langle -\sigma_x u_x \rangle_t - \langle \tau_{xy} u_y \rangle_t \tag{2.36}$$

$$I_y^s = \langle -\sigma_y u_y \rangle_t - \langle \tau_{yx} u_x \rangle_t \tag{2.37}$$

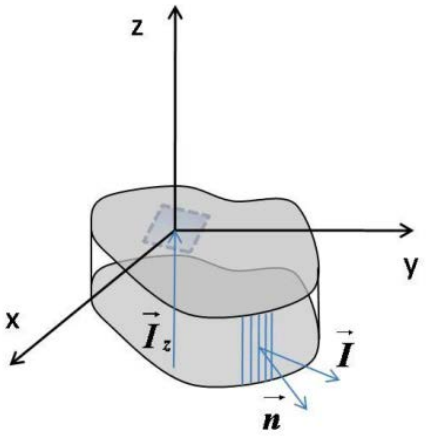

Figure 2-4: Schematic of an elastic body under plane stress conditions. The intensity vector $\vec{I}_z = 0$ [14].

Since it is not possible to directly measure stress, Equations (2.36) and (2.37) must be written in terms of strain using the constitutive equations

$$\sigma_x = \frac{E}{1-\upsilon^2}\left(\varepsilon_x + \upsilon\varepsilon_y\right) \tag{2.38}$$

$$\sigma_y = \frac{E}{1-\upsilon^2}\left(\varepsilon_y + \upsilon\varepsilon_x\right) \tag{2.39}$$

$$\tau_{xy} = \tau_{yx} = G\gamma_{xy} \tag{2.40}$$

where E, G and υ represent the elastic modulus, shear modulus, and Poisson's ratio, and the relation between E and G is $E = 2G(1+\upsilon)$. This gives the final result for each intensity component in the time domain as

$$I_x^s = -G\left[\frac{2}{1-\upsilon}\langle\left(\varepsilon_x + \upsilon\varepsilon_y\right)u_x\rangle_t + \langle\gamma_{xy}u_y\rangle_t\right] \tag{2.41}$$

$$I_y^s = -G\left[\frac{2}{1-\upsilon}\langle\left(\varepsilon_y + \upsilon\varepsilon_x\right)u_y\rangle_t + \langle\gamma_{xy}u_x\rangle_t\right] \tag{2.42}$$

To measure SSI, 5 distinct measurements are needed (3 strains, 2 velocities). In order to estimate the shear strain, a standard rosette configuration of strain gages was used. Velocity signals were numerically integrated from measured in-plane accelerations. Each individual signal is then filtered to remove any DC offset, and used for the SSI calculation. This is done for each sensor

suite, and for a set number of averages. The final result can then be averaged to obtain the final SSI quantity in the time domain. A signal flow diagram of the SSI time domain calculation process is presented in Figure 2-5.

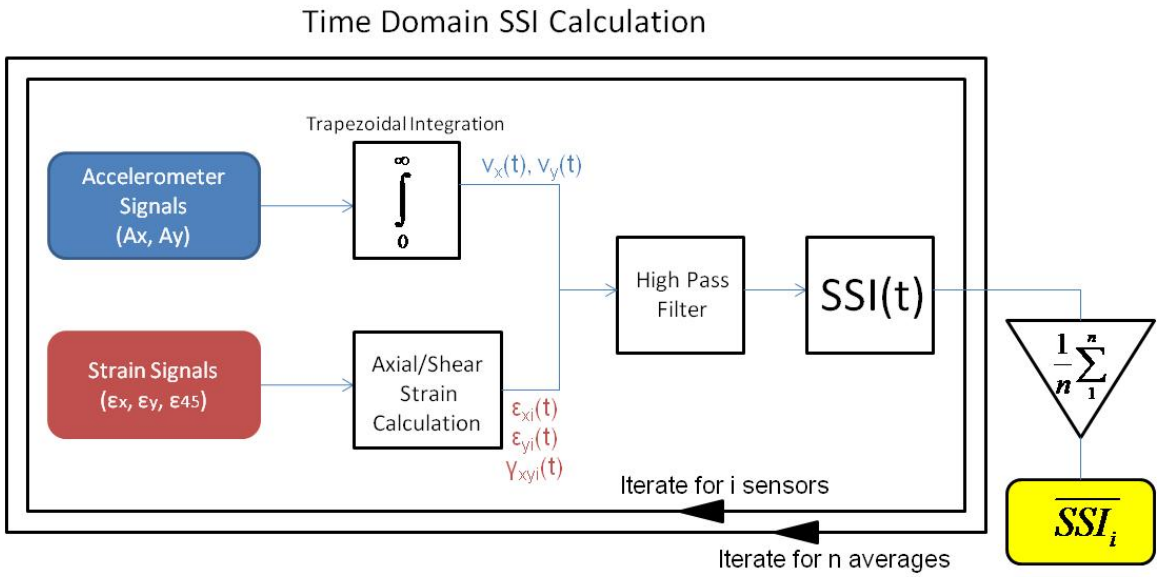

Figure 2-5: Signal flow diagram for the SSI time domain formulation. Acceleration is integrated to yield velocity. Axial and shear strains are calculated from their respective sensors. Each signal is then filtered and used for the SSI calculation.

Using Parseval's theorem [23] to transform Equations (2.41) and (2.42) into the frequency domain yields

$$\mathrm{I}_{\mathrm{x}}^{\mathrm{s}} = -\mathrm{G} * Re \int_0^{\infty} \left[\frac{2}{1-\upsilon} \left(\mathbf{G}_{\varepsilon_{\mathrm{x}} u_{\mathrm{x}}} + \upsilon \mathbf{G}_{\varepsilon_{\mathrm{y}} u_{\mathrm{x}}} \right) + \mathbf{G}_{\gamma_{\mathrm{xy}} u_{\mathrm{y}}} \right] \mathrm{df} \tag{2.43}$$

$$\mathrm{I}_{\mathrm{y}}^{\mathrm{s}} = -\mathrm{G} * Re \int_0^{\infty} \left[\frac{2}{1-\upsilon} \left(\mathbf{G}_{\varepsilon_{\mathrm{y}} u_{\mathrm{y}}} + \upsilon \mathbf{G}_{\varepsilon_{\mathrm{x}} u_{\mathrm{y}}} \right) + \mathbf{G}_{\gamma_{\mathrm{xy}} u_{\mathrm{x}}} \right] \mathrm{df} \tag{2.44}$$

where '*Re*' represents the real part of the signal, and $\boldsymbol{G}_{xy}$ represents the single sided cross-spectra between signals *x(t)* and *y(t)*. Note that in their original publication, Equations (2.43) and (2.44) contain a typographical error (missing a negative sign). A signal flow diagram of the SSI calculation process for the frequency domain method is presented in Figure 2-6.

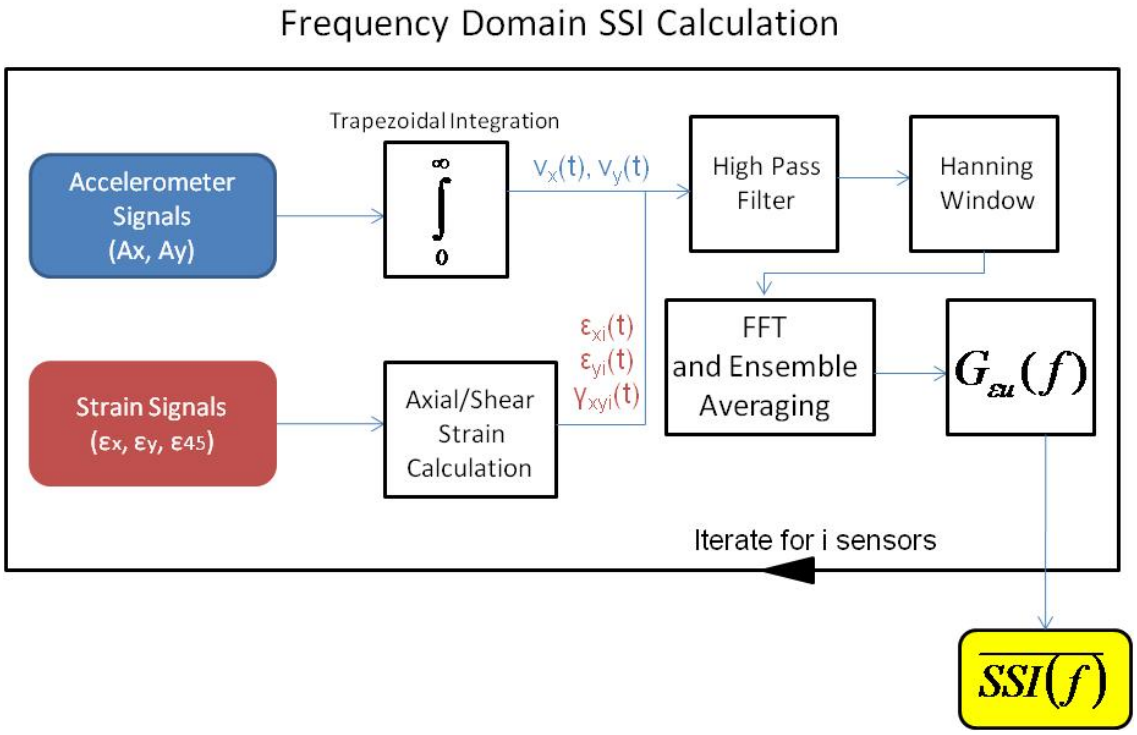

Figure 2-6: Signal flow diagram for the SSI frequency domain formulation. Acceleration is integrated to yield velocity. Axial and shear strains are calculated from their respective sensors. Each signal is then filtered, transformed into the frequency domain and ensemble averaged. The required cross spectral densities are then calculated and used for the SSI calculation.

Semperlotti et al. [14,21] recently extended the concept of Structural Surface Intensity (SSI) into the nonlinear domain. This quantity, Nonlinear Structural Surface Intensity (NSSI), is formulated for mechanical systems whose response is governed by nonlinearity at the damage location. As many linear techniques can overlook damage signatures by only evaluating changes in the drive frequency, NSSI is evaluated at the nonlinear harmonics produced when damage is present. Similar to its' linear counterpart, NSSI in the frequency domain is implemented as follows.

$$\mathrm{NSSI}_{\mathrm{x}}^{\mathrm{s}} = \sum_{\mathrm{n}=1,3,5} \left(-\mathrm{G} * Re \int_{\mathrm{nf}/2-.01\mathrm{f}}^{\mathrm{nf}/2+.01\mathrm{f}} \left[\frac{2}{1-\upsilon} \left(\mathbf{G}_{\varepsilon_{\mathrm{x}} u_{\mathrm{x}}} + \upsilon \mathbf{G}_{\varepsilon_{\mathrm{y}} u_{\mathrm{x}}} \right) + \mathbf{G}_{\gamma_{\mathrm{xy}} u_{\mathrm{y}}} \right] \mathrm{df} \right) \tag{2.45}$$

$$\mathrm{NSSI}_{y}^{s}=\sum_{n=1,3,5}\left(-G*Re\int_{nf/2-.01f}^{nf/2+.01f}\left[\frac{2}{1-\upsilon}\left(\mathbf{G}_{\varepsilon_y u_y}+\upsilon\mathbf{G}_{\varepsilon_x u_y}\right)+\mathbf{G}_{\gamma_{xy} u_x}\right]df\right) \tag{2.46}$$

Unlike linear SSI, the NSSI metric is only evaluated at the first three nonlinear sub-harmonics produced with damage. Experimentally, this evaluation is simply an integration performed with a 1% band around where each nonlinear harmonic would be located $\left(f/2, 3f/2, 5f/2\right)$ as a function of the drive frequency *f*. illustrates this formulation. The application of the NSSI formulation is illustrated with measured response spectra in Figure 2-7 .

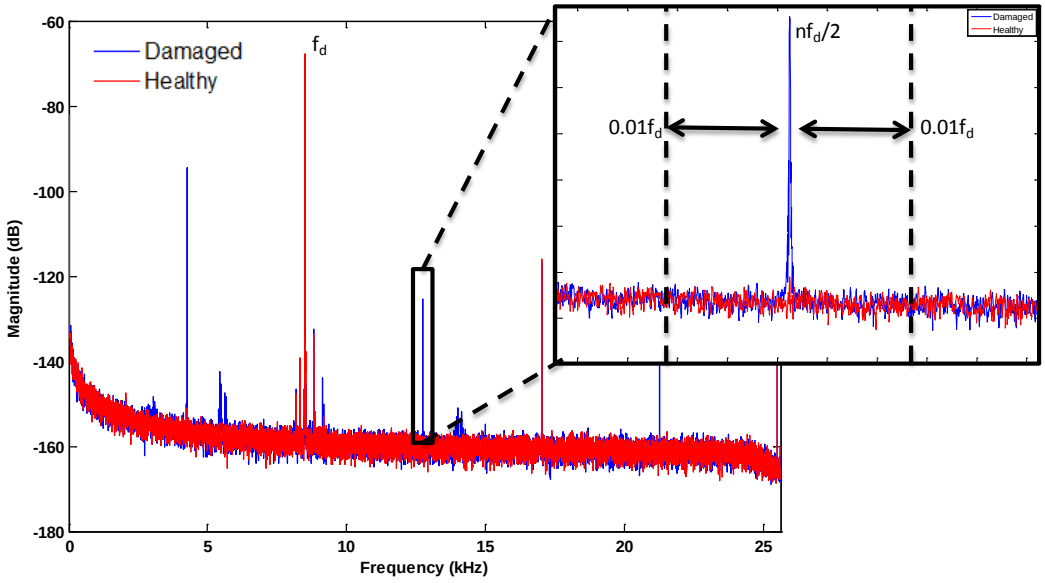

Figure 2-7: Strain response autospectra illustrating the NSSI formulation. 1% of the driving frequency is used around each sub or ultra-subharmonic for the integration limits

Nonlinear Wave Modulation Spectroscopy (NWMS) was also used to evaluate the presence of damage in a structure due to fatigue cracking [12, 13]. Similar to interrogating with a single tone harmonic excitation, nonlinear harmonics will appear in the response signature, although in a more complex form. Under a modulated wave excitation, the nonlinear response signature is more complex; wave interactions are combinations of the two interrogation

frequencies. The first order sidebands present in the response spectrum (f_+ , f_-) represent a classical nonlinearity in many systems. The higher order combinational tones ($f_{2,3+}$, $f_{2,3-}$) represent the hysteretic nonlinearity of the structure [13].

Evaluating the structural intensity at these nonlinear combinational tones forms the new approach, Nonlinear Structural Surface Intensity – Modulated Wave (NSSI-MW). Like NSSI, NSSI-MW has a high sensitivity to damage by relying on detection of combinational tones produced by the wave interactions of two interrogation signals when damage is present on a structure. Experimentally, the evaluation of NSSI-MW is again simply an integration performed with a 1% band around where each combinational tone would be located $\left(\mathrm{f_{high}} \pm \mathrm{nf_{low}}\right)$ as a function of the drive frequencies $\mathrm{f_{high}}$ and $\mathrm{f_{low}}$. The application of NSSI-MW with measured response spectra is illustrated in Figure 2-8, which in the frequency domain is formulated as follows

$$\mathrm{NSSI_x^s - MW} = \sum_{\mathrm{n=1,2,3}} \left(-\mathrm{G} * Re \int_{\mathrm{f_{high} \pm nf_{low} - .01 f_{low}}}^{\mathrm{f_{high} \pm nf_{low} + .01 f_{low}}} \left[\frac{2}{1-\upsilon} \left(\mathbf{G}_{\varepsilon_x u_x} + \upsilon \mathbf{G}_{\varepsilon_y u_x} \right) + \mathbf{G}_{\gamma_{xy} u_y} \right] \mathrm{df} \right) \tag{2.47}$$

$$\mathrm{NSSI_y^s - MW} = \sum_{\mathrm{n=1,2,3}} \left(-\mathrm{G} * Re \int_{\mathrm{f_{high} \pm nf_{low} - .01 f_{low}}}^{\mathrm{f_{high} \pm nf_{low} + .01 f_{low}}} \left[\frac{2}{1-\upsilon} \left(\mathbf{G}_{\varepsilon_y u_y} + \upsilon \mathbf{G}_{\varepsilon_x u_y} \right) + \mathbf{G}_{\gamma_{xy} u_x} \right] \mathrm{df} \right) \tag{2.48}$$

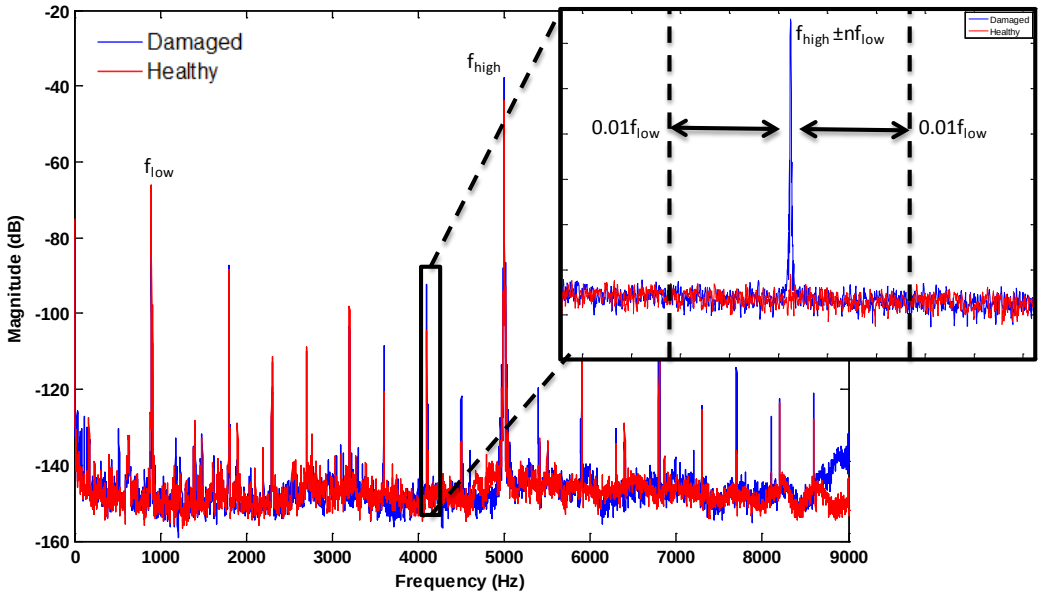

Figure 2-8: Acceleration response autospectra illustrating the NSSI-MW formulation. 1% of the low driving frequency is used around each combinational tone for the integration limits.

Each metric described here offers distinct advantages over conventional linear ultrasonic techniques for damage detection. NSI, while a useful tool for damage visualization and localization, is not easily applicable to complex geometries due to the difficulty of obtaining the needed velocity measurements, and the limitations of the original formulation. Both surface intensity metrics NSSI and NSSI-MW served to complement the NSI visualization technique as a means to apply intensity-based health monitoring techniques to more complex structures.

To quantitatively evaluate every metric described in this chapter, and their potential application realistic airframe structures, each surface intensity metric was applied to experimental data taken on a variety of test beds. When possible, NSI visualization was used to provide additional insight into how CAN will manifest with damage. A detailed description of each test bed, and its role in the development of each technique is presented in the following section.

2.4 Experimental Test Beds

The approach taken for the further development of intensity based airframe detection technology combined several different thrust areas that expanded upon important results developed by previous authors [17]. A “stepping stone” path was used to facilitate an easier transition to more complex structures, starting with an aluminum stiffened panel, adding complexity by moving to composite stiffened panels, and ultimately a tail boom from an OH-58 Kiowa Warrior.

2.4.1 Aluminum Stiffened Panel

A heavy steel fixture (Figure 2-9) was designed for use with the aluminum plate structure to allow examination of CAN effects using intensity based techniques for damage detection. This fixture provided stable clamped-clamped boundary conditions for the panel, and allowed for use of a Polytec PSV 400 scanning laser vibrometer to measure the needed surface velocities (Figure 2-10), as well as discrete sensors to characterize the flow of energy in the healthy / damaged condition. The plate was manufactured from an aluminum 7075 alloy, and the material properties and dimensions are listed in Table 2-1.

Table 2-1: 7075 T6 Aluminum Panel Material Properties

	English Units	**SI Units**
Length	35 in	.89 m
Width	23 in	.58 m
Thickness	.060 in	.0015 m
Young’s Modulus, E	10.2 Msi	70.00 GPa
Shear Modulus, G	3.90 Msi	26.90 GPa
Poisson’s Ratio (υ)	.33	.33

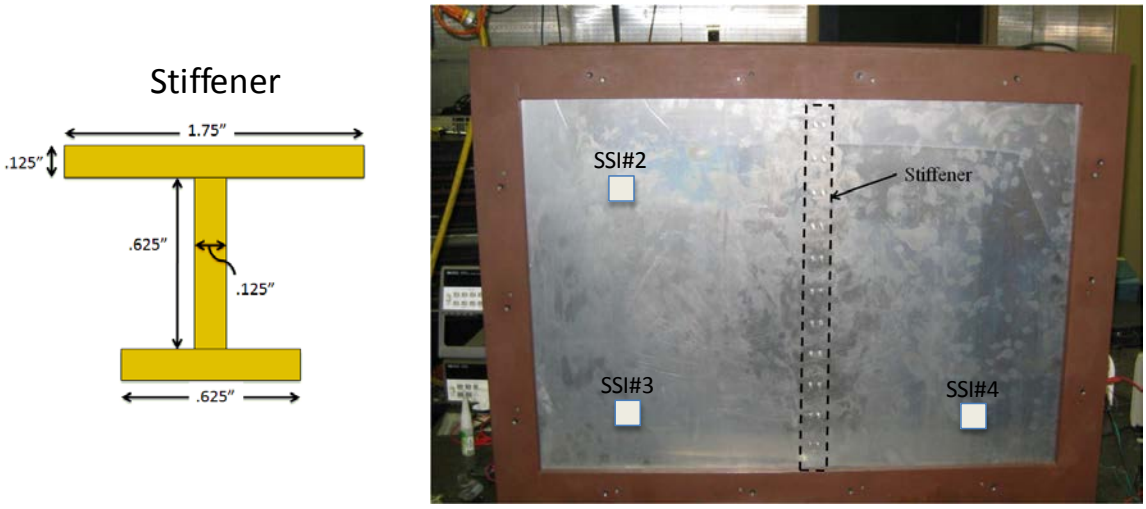

Figure 2-9: Stiffened panel test bed, isotropic aluminum plate (7075 alloy 35" x 23" x .060") in heavy steel fixture. Stiffener (T6061 alloy irregular I-beam) affixed with machine screws every 1.5". Damage is introduced by loosening fasters. Each frame bolt was torqued to 5 ft –lbs and every stiffener bolt was torqued to75 in-lb.

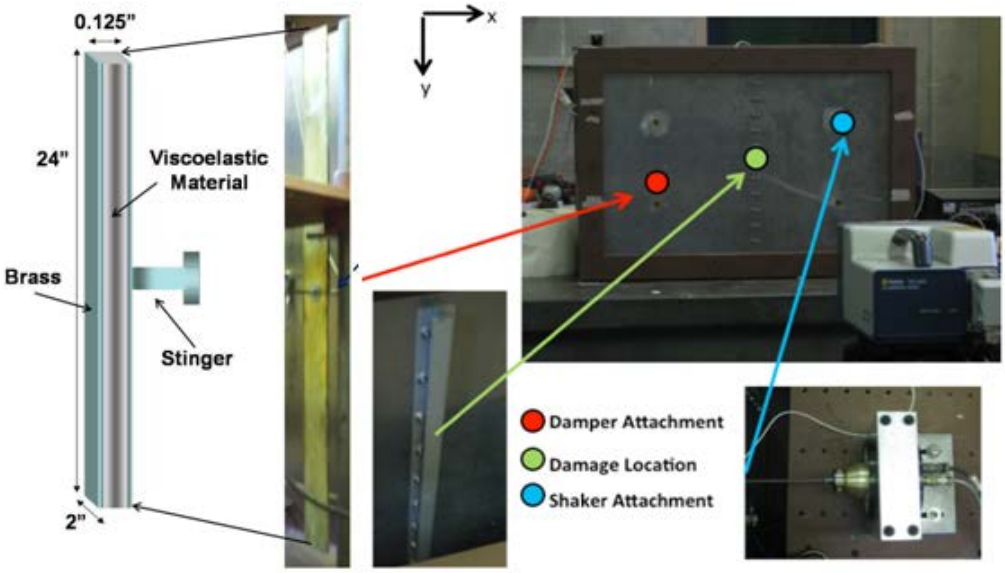

Figure 2-10: Experimental test set up with aluminum stiffened plate, vibration shaker source, point damper, and Polytec PSV 400 scanning laser vibrometer (37 x 30 grid points on plate). Damage is introduced by loosening rows of bolts on the stiffener. Damping is provided by a constrained layer damper (24" x 2" x .125") comprised of 2 layers of brass and viscoelastic material. Damping values range from η=.0138 @ 50Hz to η=.00133 @ 10000Hz

Several discrete sensor arrays for SSI measurements were present on the panel. The SSI suites consist of 3 strain and 2 velocity measurements. While it is possible to use foil strain gages

for these measurements, 3 separate PCB Piezotronics model 740B02 strain sensors were used for each rosette because of their high sensitivity and high frequency response. PCB model 356A14 tri-axial accelerometers were used to acquire the acceleration time waveforms and numerically integrated to acquire velocity. The entire sensor suite is pictured in Figure 2-11. A total of 3 SSI suites were used on the aluminum panel, located 7 inches from each edge of the plate. Their locations are shown graphically in Figure 2-9.

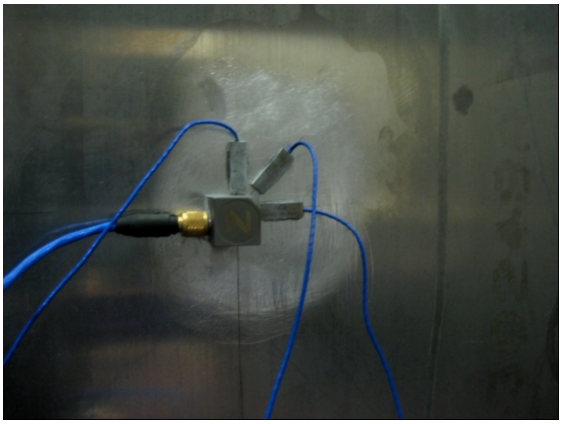

Figure 2-11: SSI measurement suite consisting of 3 separate PCB Piezotronics model 740B02 strain sensors and a PCB model 356A14 tri-axial accelerometer. The acceleration time waveform is numerically integrated to acquire the velocity needed for the SSI calculation.

While SI does not necessarily require a dominant energy source to be present [29], typically it is easier to visualize the flow of energy through a structure when clear sources and sinks are present. To provide a dominant driving source, a matched pair of Wilcoxon F4/F7 shakers was used. The electrodynamic F4 shaker has a usable frequency range of 10-7500Hz, and can provide a maximum 10 lbs. of force. The piezoceramic F7 shaker has a usable frequency range of 500-25000Hz and can provide a maximum 100 lbs. of force. Both shakers were collocated, and attached via a stinger 7 inches from both the right and top edges of the panel (Figure 2-10). To monitor the total input force at any given time, a PCB Piezotronics model 288D01 impedance head was attached at the end of the stinger to the plate (Figure 2-12). The measured surface velocities from the vibrometer, along with the input force from the impedance

head provided the necessary frequency response data needed to estimate the structural intensity at every grid location.

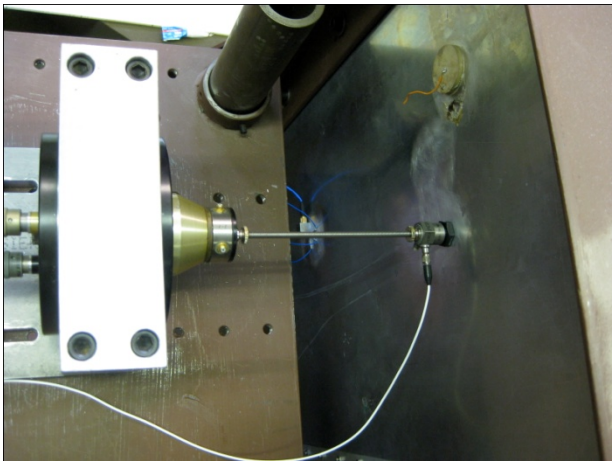

Figure 2-12: Orientation of the impedance head in relation to the aluminum panel test bed. The shaker was attached via a stinger, and the impedance head was used to measure the continuous force output from the shaker. These measurements were used a reference for the frequency response data needed to calculate the structural intensity field on the entire structure.

A point-damper was added to the plate to provide a dominant sink for the energy path to dissipate. The damper was constructed as a constrained layer beam, made of a brass 260 alloy and viscoelastic material, had dimensions 2 in × 24 in × 0.125 in. The beam was located 7 in from the left edge and 11 in from the bottom edge of the panel, and is pictured in Figure 2-10. Damping values added by the constrained layer beam ranged η=.0138 @ 50Hz to η=.00133 @ 10000Hz. Damage was introduced to the system by loosening rows of fasteners attaching the stiffener to the plate. Since the behavior of isotropic plates is well understood, this test bed served as the primary structure for algorithm development for intensity-based SHM metrics.

2.4.2 Composite Stiffened Panels

To investigate the potential for applying SI techniques to advanced composite airframe design, two composite panels were fabricated, with damage introduced into one as a 1”

delamination present at the truncation of the stiffener on the damaged panel (Figure 2-13). The panels were made from S-Glass and ACG VTM 264 toughened epoxy resin. The stiffener was cut from commercially available extrusion of cross-ply carbon fiber, and bonded to the panel using Epoxy 907. The material properties of the panel and stiffener are listed in Table **2-2**.

Table 2-2: Composite Stiffened Panel Material Properites

	Composite Panel		**Box Stiffener**	
	English Units	**SI Units**	**English Units**	**SI Units**
Length (in, m)	37.00	.94	12.00	.30
Width (in, m)	25.00	.64	1.50	.038
Height (in, m)	-	-	1.50	.038
Thickness (in, m)	.25	.0064	.25	.0064
Density, ρ ($slug/ft^3$, kg/m^3)	2.31	1190.00	2.72	1400.00
Young's Modulus, E (Msi, GPa)	12.33	85.00	18.85	130
Shear Modulus, G (Msi, GPa)	.56	3.87	-	-
Poisson's Ratio (υ)	.32	.32	-	-

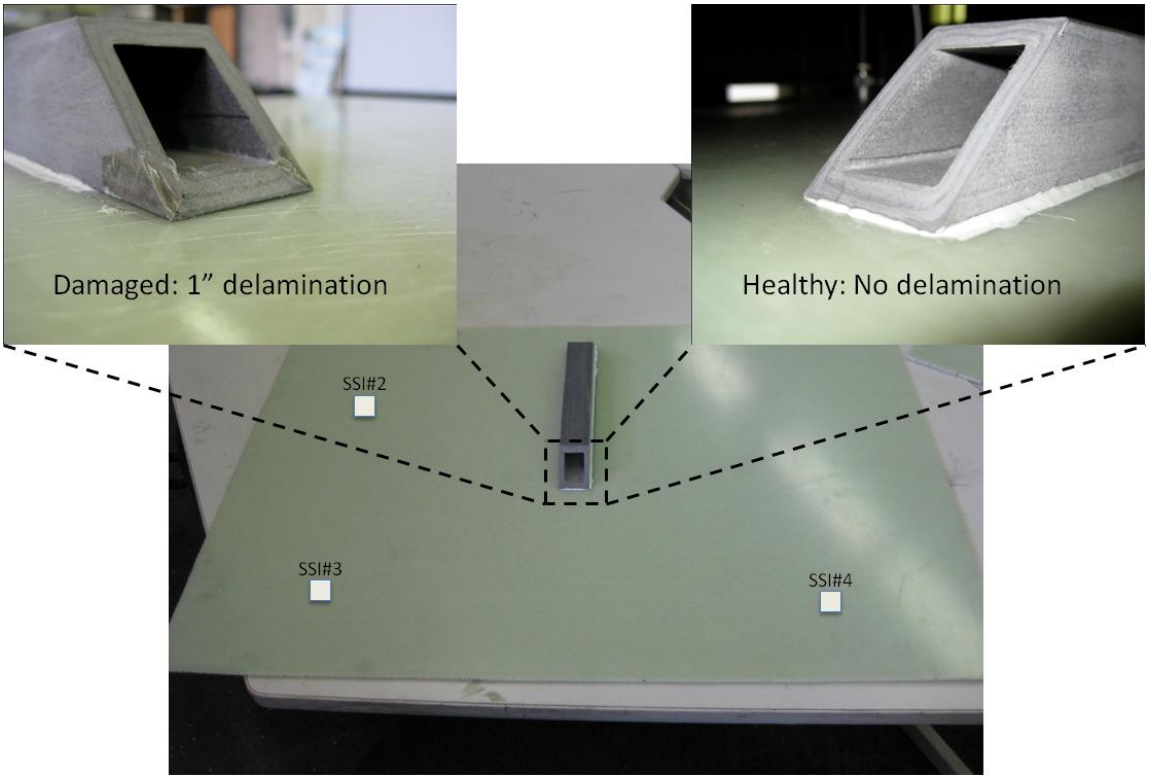

Figure 2-13: Composite Stiffened Panels ([0/90 +45/-45]s 37” x 25” x .25” S-glass/ACG VTM264 toughened epoxy resin). There is a 1" delamination manufactured into the damaged panel at the stiffener termination to simulate a relevant stiffened composite damage type.

The composite stiffened panels were also instrumented similar to the aluminum stiffened panel, with SSI suites located 7 inches from each corner, seen graphically in Figure 2-13. Excitation was again provided by the Wilcoxon F4/F7 matched shaker pair. However, boundary conditions for the panel were provided by two single pins, as seen in Figure 2-14. The right side pin location was 15.5 inches from the bottom of panel. Similarly the left side pin location was 14 inches from the bottom. Because this particular type of composite material had a low optical reflectivity, Magnaflux Spotcheck SKD-S2 Developer was used to coat the panel to make it easier to acquire vibrometer scan data. This coating has no effect on the material properties of the panel, and is similar in substance to chalk dust.

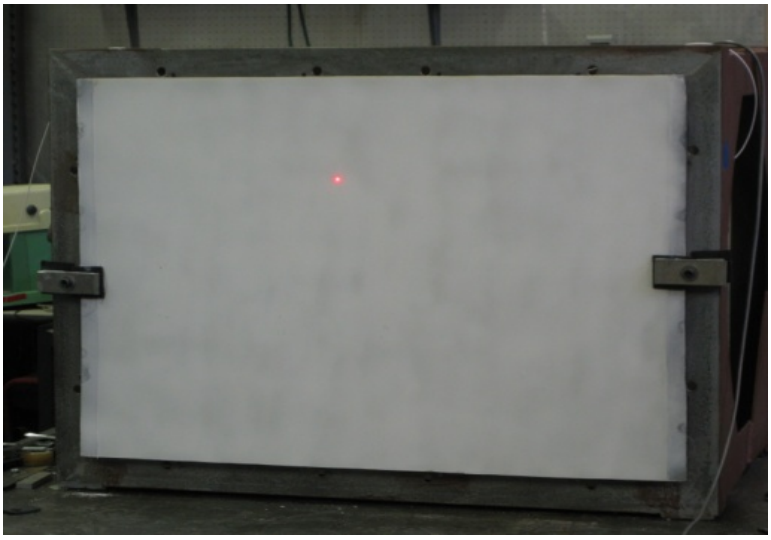

Figure 2-14: Composite stiffened panel in a heavy steel fixture. The panel is pinned at two locations, and coated with Magnaflux Spotcheck SKD-S2 Developer to make scanning with a vibrometer easier.

2.4.3 OH-58D Kiowa Warrior Tail Boom

In order to transition each intensity-based damage detection metric to a complex airframe structure, an OH-58 tail boom (Figure 2-15) was instrumented and used for exploratory measurements. To reduce the vibration signature complexity, and have a viable baseline with a low noise floor, several components were modified/removed from the structure. The rivet lines running lengthwise along the structure were drilled out, as were mounting heads along the bottom of the structure. All loose nut plates where the horizontal stabilizer is located (attaching to the rectangular hole near the mid bulkhead) were filled in with screws and tightened down. The standard hanger bearing brackets that normally secure the drive shaft were simulated with manufactured aluminum blocks able to be loosened, which introduced damage. Boundary conditions were considered to be “free-free”, as the tail boom was suspended at both ends by bungee cords.

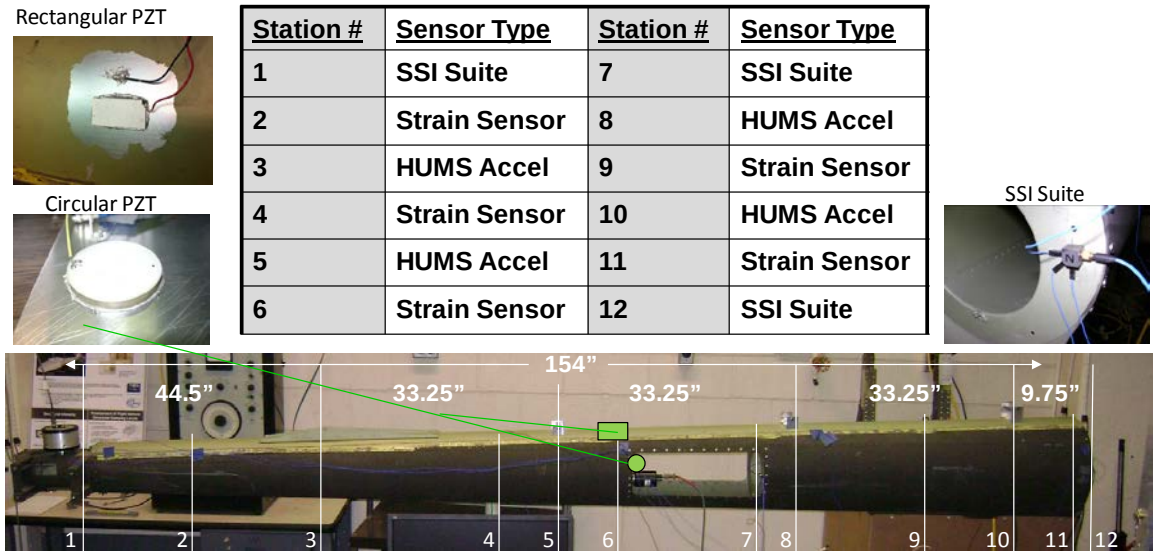

Station #	Sensor Type	Station #	Sensor Type
1	SSI Suite	7	SSI Suite
2	Strain Sensor	8	HUMS Accel
3	HUMS Accel	9	Strain Sensor
4	Strain Sensor	10	HUMS Accel
5	HUMS Accel	11	Strain Sensor
6	Strain Sensor	12	SSI Suite

Figure 2-15: OH-58 Kiowa Warrior Tail boom. Structure was instrumented with a Wilcoxon F4 electrodynamic shaker aft, F7 piezoelectric shaker at the mid location, SSI suites at the aft, mid and forward locations, lateral accelerometers mounted to the hanger bearing brackets, and skin strain gages across the length of the tail boom. Additionally, embedded PZT actuators were located at the mid location on the bulkhead and also on the outer skin.

The structure was excited via two different actuation methods; a Wilcoxon F4 shaker mounted on the aft bulkhead and F7 shaker mounted on the mid bulkhead provided out-of-plane excitation, and a rectangular piezoelectric transducer (PZT) was embedded on the upper skin above the mid bulkhead, and a circular PZT embedded on the mid bulkhead. Both the rectangular and circular PZT actuators were manufactured by PiezoKinetics Inc. Their properties are listed in Table 2-3.

Table 2-3: Piezoelectic Actuator Properties

	Circular	**Rectangular**
Material	Navy Type II	Navy Type II
Length (m)	Radius=.038	.038
Width (m)	-	.020
Thickness (m)	.0051	.0025
Capacitance, C_x (pF)	3575.10	3135.80
Transverse Mode (kHz)	-	41.00
Radial Mode (kHz)	54.00	-
Thickness Mode (kHz)	390.00	792.60

The tail boom was also instrumented with a variety of different sensors across the length. SSI suites were mounted at the aft, mid, and forward bulkheads, as these are the most likely locations the sensor arrays would be mounted on the flight vehicle. Lateral accelerometers (PCB model 352C66) were mounted to each hanger bearing bracket, and were used to simulate the presence of HUMS accelerometers already present on most OH-58 airframes. Lastly, five strain gages (PCB model 740B02) were mounted on the skin between each bearing bracket.

Each specific test bed strove to compare the performance of the previously developed intensity based SHM detection algorithms, and serve as a development platform to evaluate new methods. The stiffened panel structures provided valuable insight into how CAN will manifest with different types of damage. The OH-58 tail boom was used to show that intensity-based health monitoring techniques can be transitioned to complex airframe structures. Results investigating the presence of CAN on both the aluminum and composite stiffened panels are presented in Chapter 3. Results detecting similar types of nonlinear behavior showcasing the new hybrid technique, NSSI-MW, are presented in Chapter 4, and results combining both single tone and interrogation via NWMS for the OH-58 Kiowa Warrior tail boom are presented in Chapter 5.

Chapter 3

Investigation of CAN on Aluminum and Composite Stiffened Panels

3.1 Introduction

In order to evaluate the effectiveness of each SI-based damage detection metric, a series of experimental case studies were performed on a variety of test structures described previously in Chapter 2. The stiffened panel test beds served as platforms for algorithm development, and provided insight into how contact acoustic nonlinearities will manifest with relevant damage types. Results from these experiments were used to evaluate the relative performance of each technique with the methods described in Sections 2.2 and 2.3.

NSI visualization results for the aluminum stiffened panel are presented in Section 3.2, showcasing the advantage nonlinear visualization techniques have over conventional linear ultrasonic methods. The motivation for transitioning to a discrete sensor measurement technique, and highlights the effect of damping on NSSI is described in Section 3.3. In addition, discrete sensor measurements are presented for the composite stiffened panel test beds, proving NSSI can be transitioned to more complex structural components. The hysteresis characteristics of CAN with respect to frequency and amplitude changes using NSSI is covered in Section 3.4, and highlights the motivation for transitioning to a hybrid interrogation technique with a more stable response.

3.2 NSI Damage Visualization Results - Aluminum Stiffened Panel

Nonlinear Structural Intensity (NSI) has proved to be a powerful tool for visualizing damage present in structures. As stated previously, the damaged response of a contact interface will redistribute energy from the driving frequency into nonlinear harmonics, which act as a virtual "source" at the damage location. NSI is used to evaluate the active energy flow that occurs at these nonlinear harmonic frequencies. By taking the divergence of this NSI field, the nonlinear energy source present from damage effects can be localized. These intensity and divergence maps help illustrate how CAN will manifest with incremental damage present at a given location on an aluminum stiffened panel. To calculate the nonlinear structural intensity field present on this panel, MATLAB codes were developed to post-process the data using the finite difference approximations described in Chapter 2. These codes are contained in Appendix A.

Activating a contact acoustic nonlinearity sub-harmonic response requires careful selection of frequency and drive amplitude, as the phenomenon is inherently unstable. While it is possible to choose potential interrogation frequencies by using quarter- or half- bending wavelengths proportional to the damage feature size (by calculating wave dispersion curves based off the material properties), this does not always yield a driving condition that will create a CAN sub-harmonic response. In this case, several driving conditions were found for the aluminum stiffened panel that activated a CAN. A drive frequency of 3000 Hz (bending half-wavelength = 1.75 in.) and driving amplitude of .734 A was chosen, as this driving condition showed the strongest nonlinear response with respect to the damage condition on the structure.

To understand how a CAN will manifest with damage, NSI visualization was first applied to the aluminum stiffened panel test bed (Figure 2-10) with damage introduced as loose fasteners connecting the plate to the stiffener. When actively excited using a single frequency, the healthy condition (no loose fasteners) exhibits none of the characteristic nonlinear behavior present with

the damaged condition. In comparison, a strong nonlinear response appears in the damaged response spectra ($nf/2$ harmonics), shown in Figure 3-1. Note that nf nonlinear harmonics appear in both the healthy and damaged conditions. For the healthy condition, nf harmonics are due to harmonic distortion in the drive / actuator.

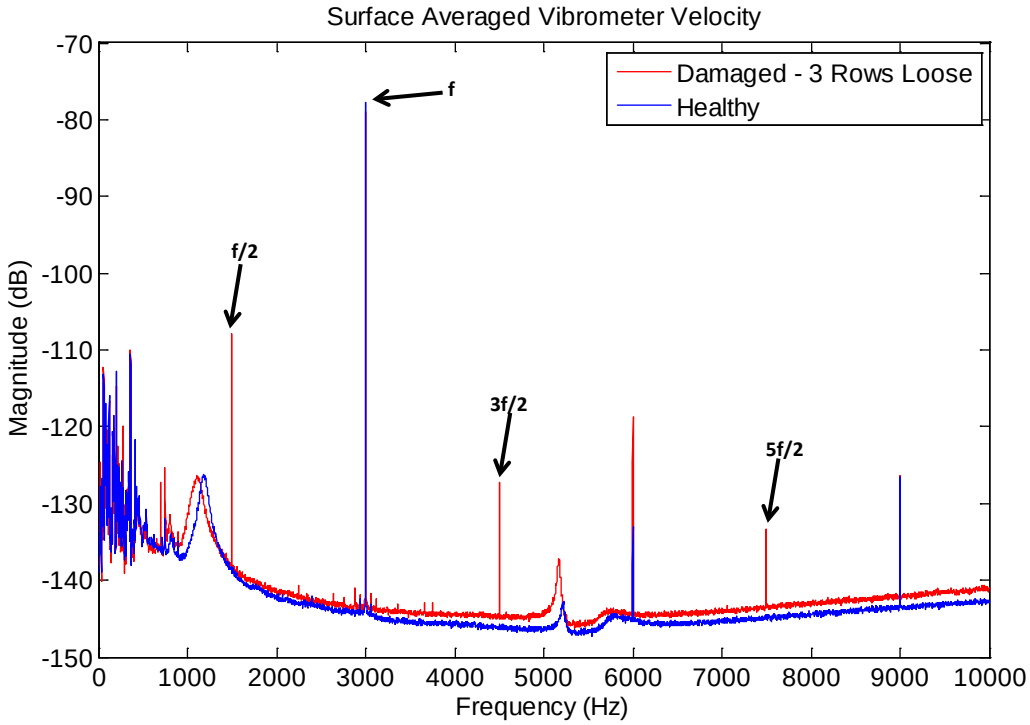

Figure 3-1: Stiffened aluminum panel healthy and damaged surface averaged velocity autospectra. Note the presence of sub and ultra-subharmonics in the damaged state.

By exploiting the information present in these nonlinear harmonics, NSI maps provide valuable insight into how CAN will manifest with different types and increments. The SI field is very complex at the driving frequency of 3000 Hz (Figure 3-2), with energy reverberating throughout the structure. Despite the complexity, energy at the drive frequency can be seen flowing from the source location (blue dot) to the sink location (green dot) through the stiffener (Figure 3-2 – upper left). This is verified in the divergence plot (Figure 3-2 – upper right), where the driving source and sink are localized.

While no source is visible at the damage location by evaluating NSI at the driving frequency, a clear nonlinear energy source is present when NSI is evaluated at the 3f/2 ultra-subharmonic. Again, the NSI field (Figure 3-2 - lower left) at this frequency is very complex, but the highest magnitude is located within the damage footprint (dotted box), and energy can be seen flowing away from the damage location at the center of the panel. The corresponding divergence plot (Figure 3-2 -lower right) for the 3f/2 ultra-subharmonic proves the existence of the "virtual" energy source that occurs as fasteners are loosened on the stiffened-plate system. Previous NSI results evaluated at a super-harmonic frequency [19] showed a localized a source due to damage (Figure 1-6), but were corrupted by the presence of harmonic distortion in the actuator system. Since NSI was evaluated in this case at an ultra-subharmonic frequency, these new results are not affected by harmonic distortion, and clearly show the "source" location within the damage footprint.

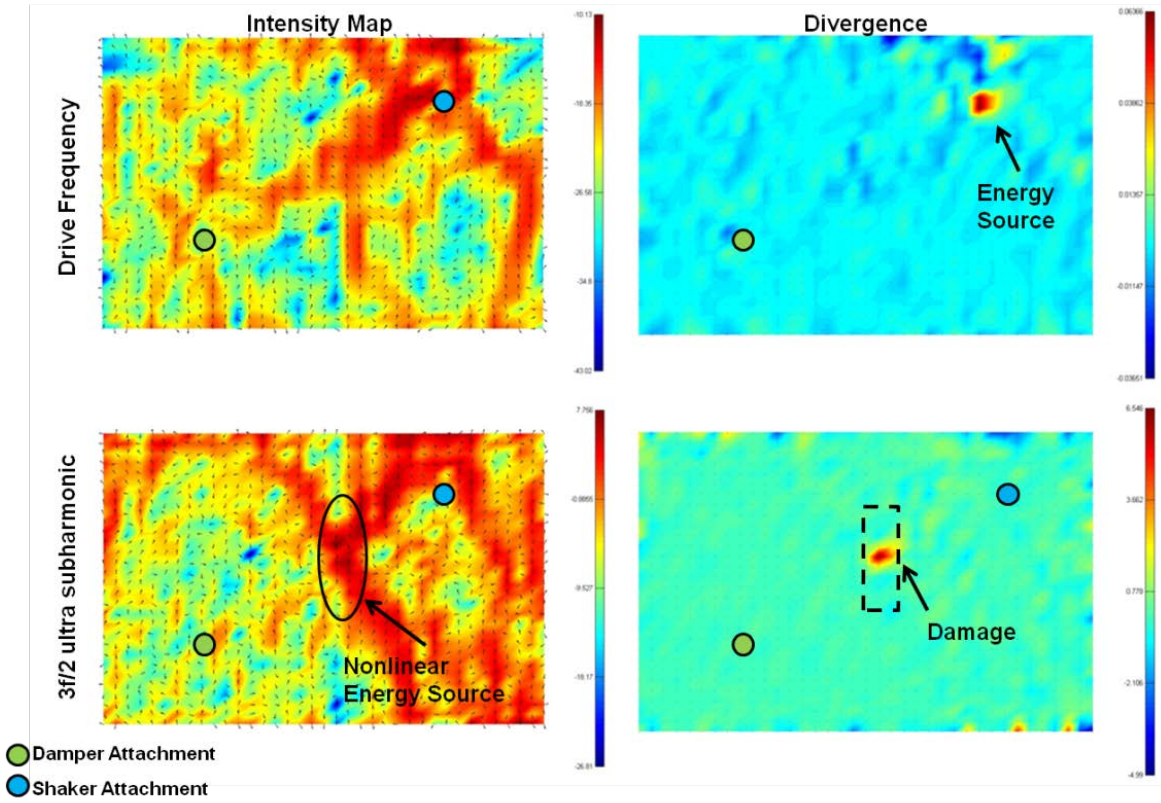

Figure 3-2: Stiffened aluminum plate nonlinear structural intensity maps for 3 rows of fasteners removed (upper maps - SI at the driven frequency 3 kHz, and associated divergence). The lower maps show the SI and associated divergence for the same drive frequency at the 3f/2 subharmonic. Despite the complex SI field, there is still clear identification of the shaker source in the upper map, and localization of the damage source in the lower divergence map.

While NSI is a powerful visualization tool to understand how CAN manifests with damage, use of the metric for practical airframe structural health monitoring applications is limited. The original formulation of SI is only valid for structures conforming to thin plate theory assumptions (isotropic, thin with respect to lengthwise dimensions). In addition, NSI visualization maps are difficult to measure on heavily reverberant (lightly damped) structures due to the extremely large reactive vibration component (standing waves) and relatively small active vibration (net energy flow) component. This makes the use of NSI for inspection of in-situ airframe components limited, as very few rotorcraft structures conform to these assumptions.

These concerns led to development of SI-based damage detection techniques using discrete sensors.

3.3 NSSI Measurement Results - Aluminum and Composite Stiffened Panels

Using the stiffened aluminum panel, NSI visualization was combined with NSSI's sensitivity to detect structural damage and visualize the key CAN effects. NSSI provides an extremely high sensitivity metric that employs discrete sensors that can detect and size damage. The physical foundation of the NSSI metric allowed for its use as a damage size parameter, as the energy produced by the CAN impact is related (for the same active interrogation drive) to the damage extent. Using NSSI arrays as discrete sensors to characterize the energy flow in structures has several distinct advantages. First, the formulation for NSSI allows for the technique to be applied on structures that do not conform to thin plate theory assumptions. This includes structures with varying levels of damping, and anisotropic composite materials. Additionally, the small footprint (1 in^2) of the sensor arrays lends itself well to on-aircraft SHM systems.

3.3.1 NSSI Time Domain vs. Frequency Domain Measurements

Previous work showed that NSSI exhibits a monotonic trend with damage extent [17], and Section 2.3 covered the corresponding measurement procedure using time averaged quantities from measured strains and accelerations. To fully evaluate the damage detection potential of the NSSI metric, a direct comparison between the frequency and time domain method was warranted.

To calculate NSSI in the time domain, data is processed similar to the signal flow diagram described in Chapter 2. However, because NSSI gives an estimate of the mechanical

energy transferred to nonlinear frequencies due to the damage, data must be band-pass filtered around each sub-harmonic. Simply due to the nature of digital filters, the pass band will have roll-off, including noise in the calculation. This noise can decrease the overall detection strength of the algorithm, or in some cases completely obscure it. In addition, with improper filter settings, the roll-off of some sub-harmonic filters can include a low amplitude component of the driving frequency, corrupting the calculation (Figure 3-3).

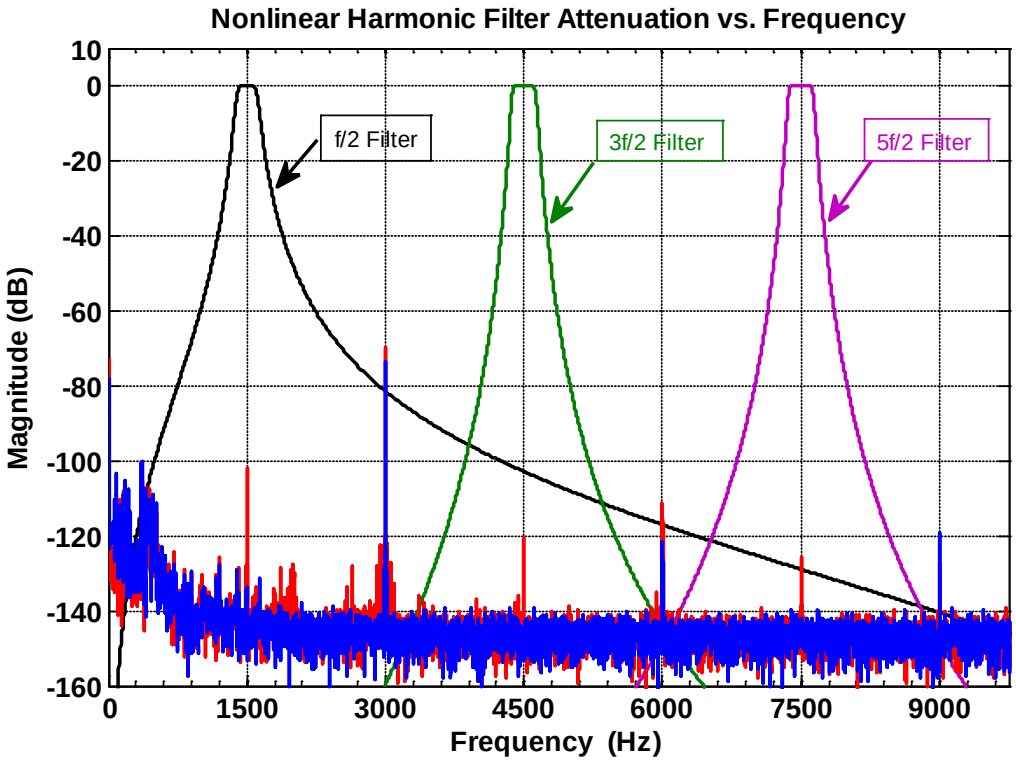

Figure 3-3: Example of an f/2 filter that corrupts the NSSI calculation. The filter includes a low amplitude component of the driving frequency and several overtones, which artificially raises the detection strength of the NSSI metric.

For lower frequencies (less than 2 kHz) that have closely spaced spectral harmonic components, designing a stable filter with low pass band ripple, tight roll off, and enough stopband attuenation can be extremely difficult. To overcome this, the frequency domain method does not use digital filtering around each nonlinear harmonic. Instead, a bounded integration is

used at the location where the nonlinear harmonic would appear (see Figure 2-7). To evaluate the differences between the frequency domain and time domain method, damage progression data was taken on the aluminum stiffened panel, and processed via both methods.

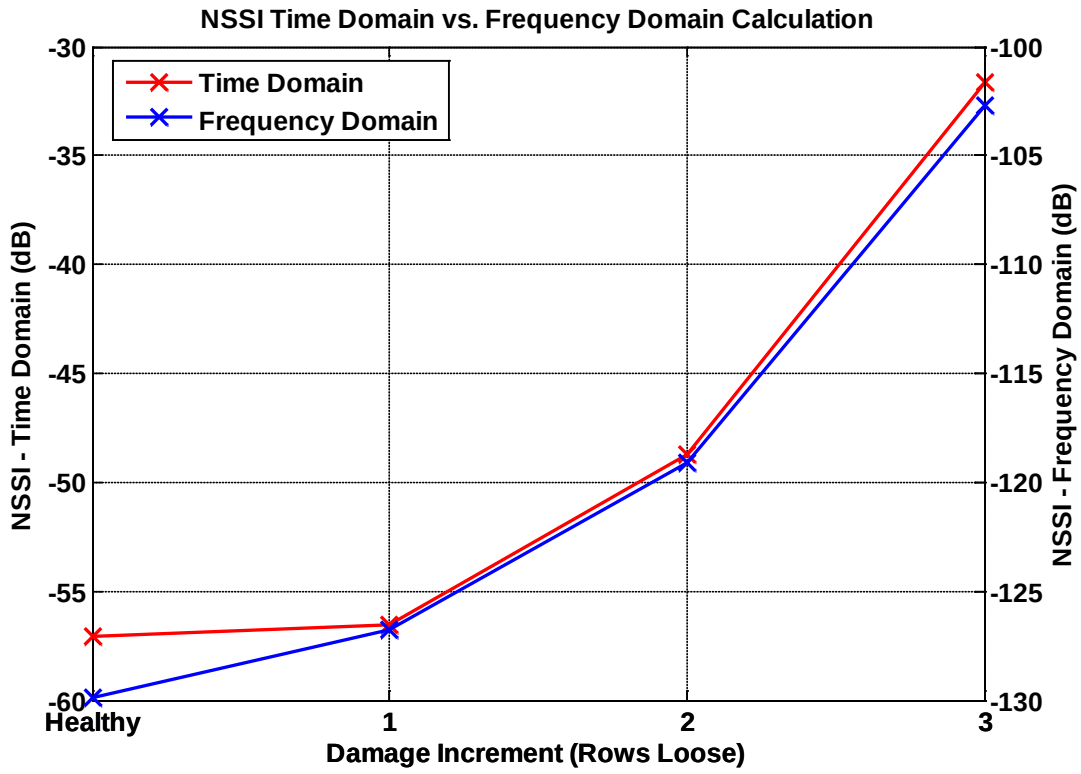

Figure 3-4: Time domain vs. frequency domain NSSI calculation for f_{drive} = 3kHz. Each method exhibits a monotonic trend, as expected. The frequency domain method has a lower noise floor, and a stronger detection of the first damage increment.

Figure 3-4 presents the damage progression trend for NSSI at a drive frequency of 3 kHz for the aluminum stiffened panel with no point damper present. While each method exhibits the same monotonic trend, a roughly 60dB difference can be seen between each data point. This is expected, as the time domain filters introduce more noise into the calculation, corresponding to a higher overall NSSI value. Additionally, the frequency domain method has higher detection strength of the first increment by 2.5dB, implying that using this method allows the NSSI metric to have a higher sensitivity than the time domain method. Currently, measurements for intensity-

based health monitoring are concerned only with the overall change between a healthy and damaged case. However, the stress level in the NSSI calculation could also be used for damage size evaluation.

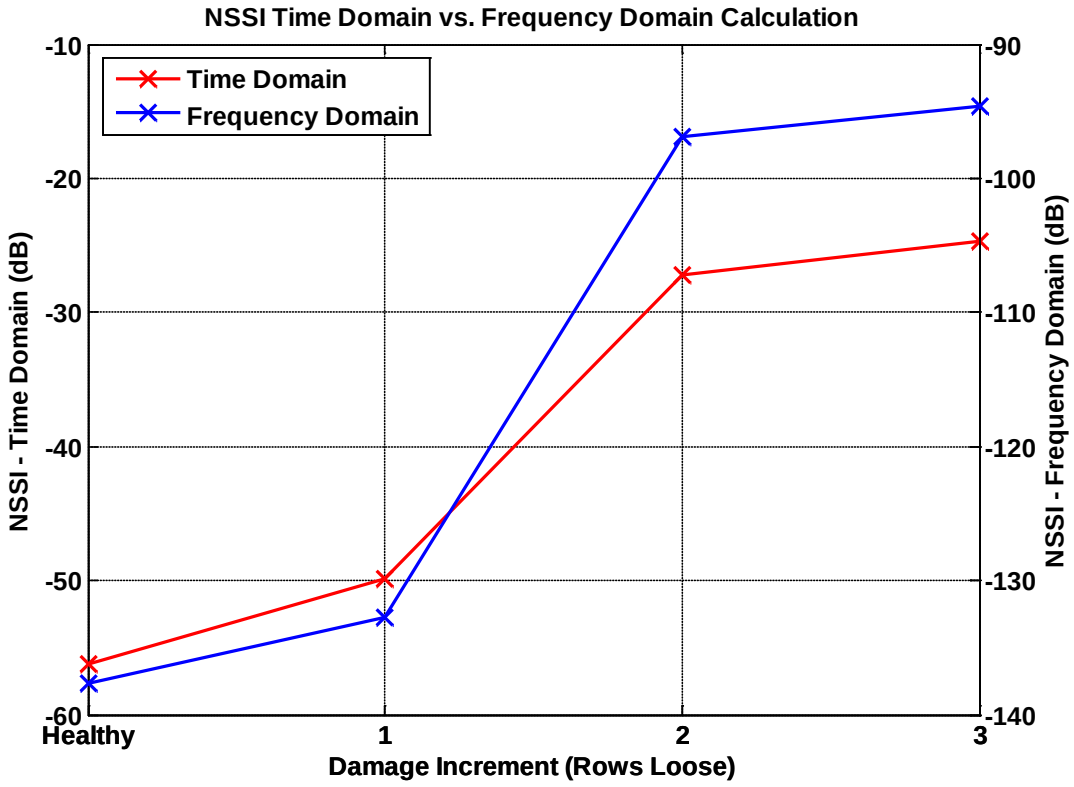

Figure 3-5: Time domain vs. frequency domain NSSI calculation for f_{drive} = 2.2kHz. Each method exhibits a monotonic trend, as expected. The frequency domain method has a lower noise floor, and a stronger overall sensitivity to damage.

Figure 3-5 shows the same damage progression trend for NSSI at a drive frequency of 2.2 kHz for the aluminum stiffened panel with no point damper present. Again, each method exhibits the same monotonic trend, but a larger difference of around 80 dB can be seen between the two methods at each successive damage progression. Additionally, for this driving condition, the frequency domain method has a higher overall detection strength by 11.6 dB.

While both methods are able to characterize the damage progression accurately, the frequency domain method has a greater sensitivity to individual damage size changes, and a

higher overall detection strength. For these reasons, the frequency domain method was chosen for use with all SI-based discrete sensor measurements measurements. All discrete sensor calculations present in this thesis hereafter are assumed to use the frequency domain method unless otherwise specified.

3.3.2 Sensitivity of NSSI to Structural Damping

To quantify the damage detection / sensitivity dependence on structural damping levels, NSSI damage progression trends were evaluated on the aluminum stiffened panel test bed with and without an added point damper (constrained layer beam) attached to the plate. Early laboratory experiments used lightly damped test structures (η less than .01), which proved difficult for measurement of NSI maps. Since airframe structures are anticipated to have much higher structural damping levels, further study was needed to fully characterize the sensitivity of the NSSI metric.

To measure the level of damping provided by the constrained layer beam (pictured in Figure 2-10) loss factors were calculated from roving hammer modal measurements using the time rate of decay of the structural impulse response at specific one third octave (OTO) band frequencies [27]. For OTO band, data was time reversed filtered to eliminate phase distortion, and a Hilbert Transform was applied to obtain the decay envelope. From this envelope, the decay rate is fit to the envelope, and the loss factor is then calculated similar to Reference [30]. Results from the measurements are presented in Figure 3-6, and the ratio between the damped and undamped cases is presented in Figure 3-7. At the lowest frequency band, the damper adds a factor η=.0138 @ 125Hz, and at the highest frequency band, the damper adds η=.00133 @ 10000Hz. On average, this is around 1.5-3 times greater than the un-damped case, providing a reasonable level of damping to simulate more complex structures.

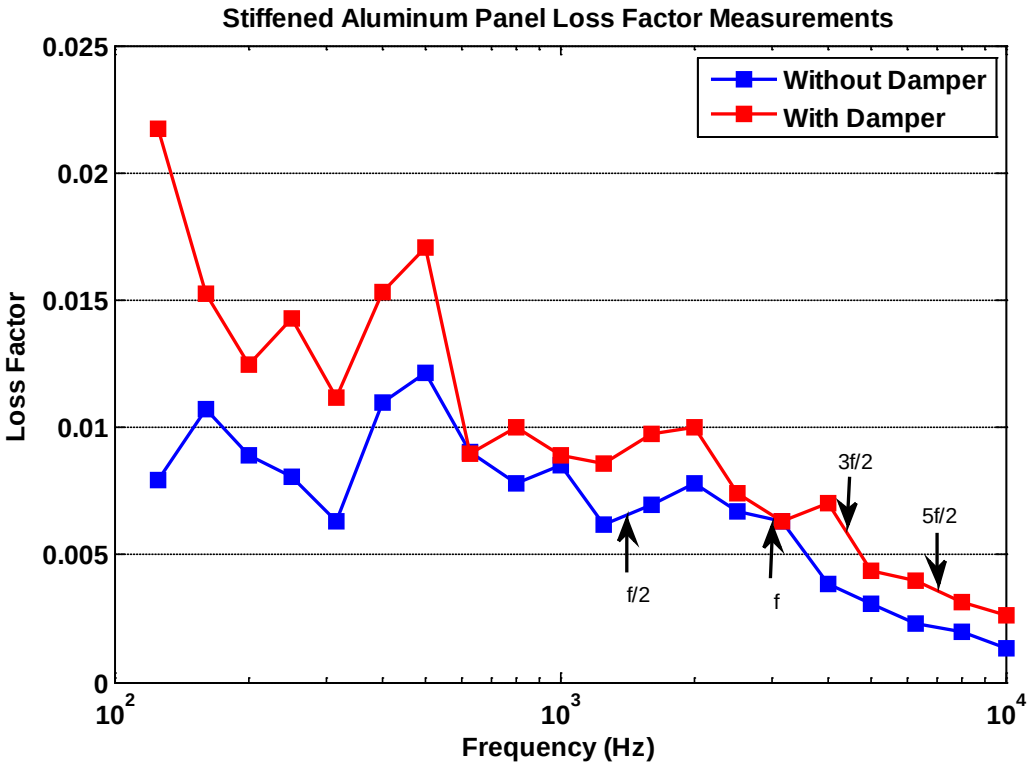

Figure 3-6: OTO band decay loss factor measurements for the aluminum stiffened panel test bed with and without an added point damper (constrained layer beam). Damping values added by the constrained layer beam ranged from η=.0138 @ 50Hz to η=.00133 @ 10000Hz. Arrows illustrate the difference in damping at each harmonic component for f_{drive} = 3 kHz.

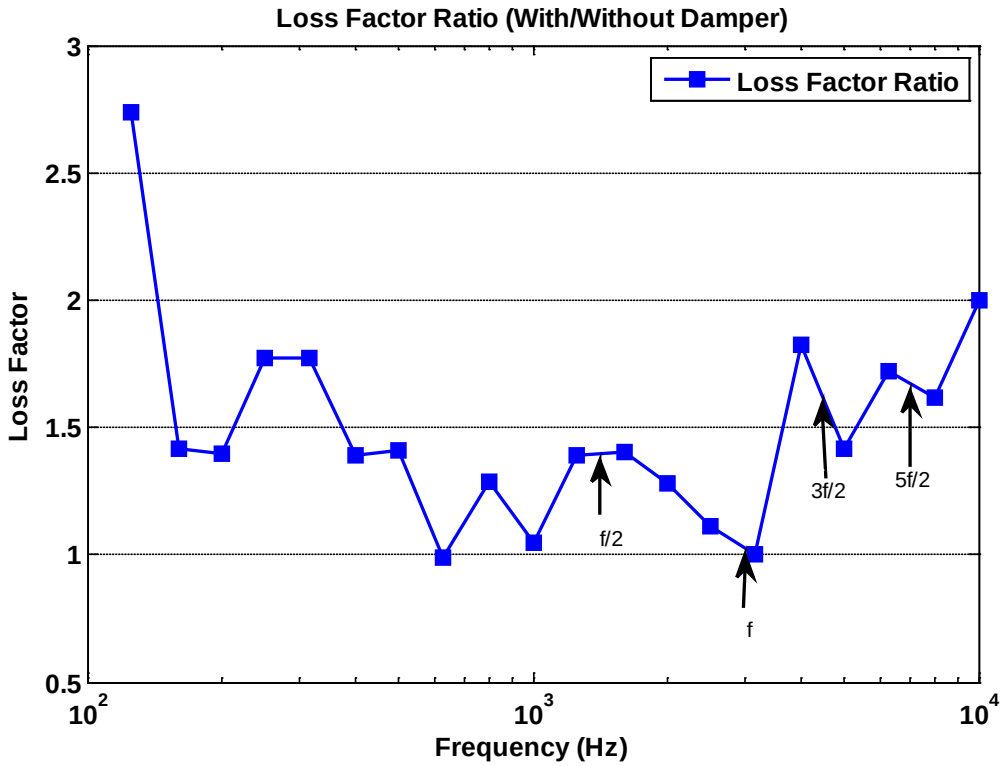

Figure 3-7: Ratio between OTO band decay loss factor measurements for the aluminum stiffened panel test bed in the damped and undamped case. On average, the increase in damping was 1.25-2 times the levels of the undamped case. Arrows illustrate the difference in damping at each harmonic component for f_{drive} = 3 kHz.

Once the amount of damping provided by the constrained layer beam was characterized, NSSI was evaluated at several frequencies, and multiple damage increments with and without the point damper attached to the panel. Experimental results were acquired for different driving frequencies and several different damage configurations. Damage was introduced as a progression; for each increment, successive rows of bolts were removed. Each damage increment corresponded to a footprint size of 4, 6, and 8 inches respectively. Damage was initiated from the center most row (row #6) of bolts on the stiffener. Each successive damage increment included rows loosened above the center row (rows #7 and #8). An example sensor spectra (Figure 3-8) is shown to illustrate the presence of nonlinear harmonic frequencies created from CAN occurring at the damage location. Damage progression results for NSSI evaluated with and without an

added point damper are presented for a driving frequency of 3 kHz (Figure 3-9) and 2.2 kHz (Figure 3-10).

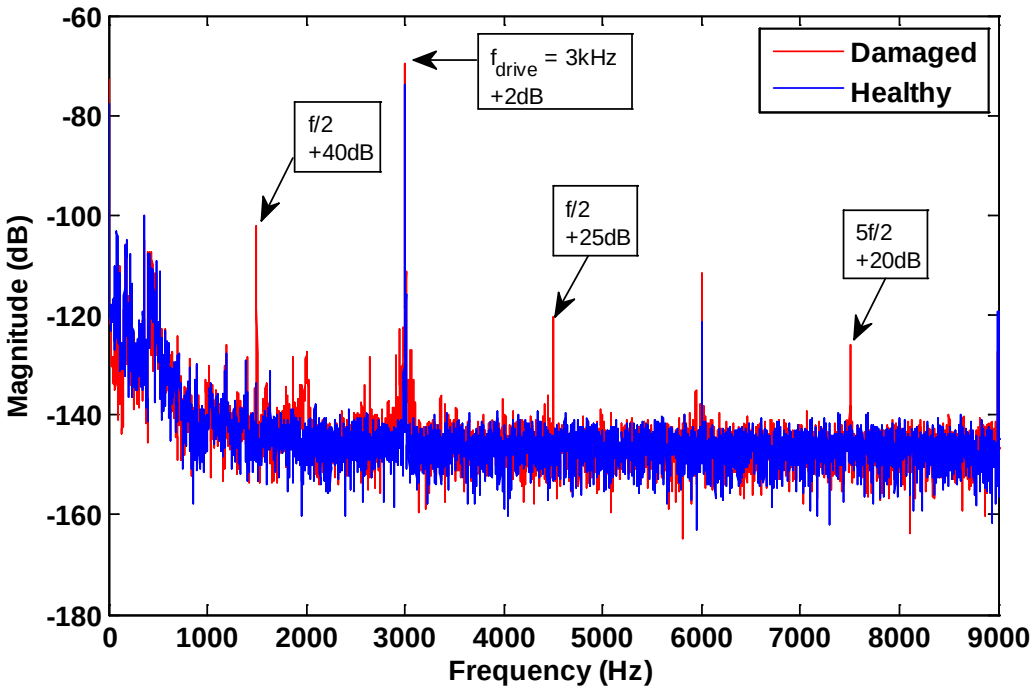

Figure 3-8: Stiffened aluminum panel 45 degree strain sensor autospectra showing the presence of nonlinear harmonics between the healthy and damaged panels. Note the large change in subharmonic response compared to the relatively small change in driving frequency.

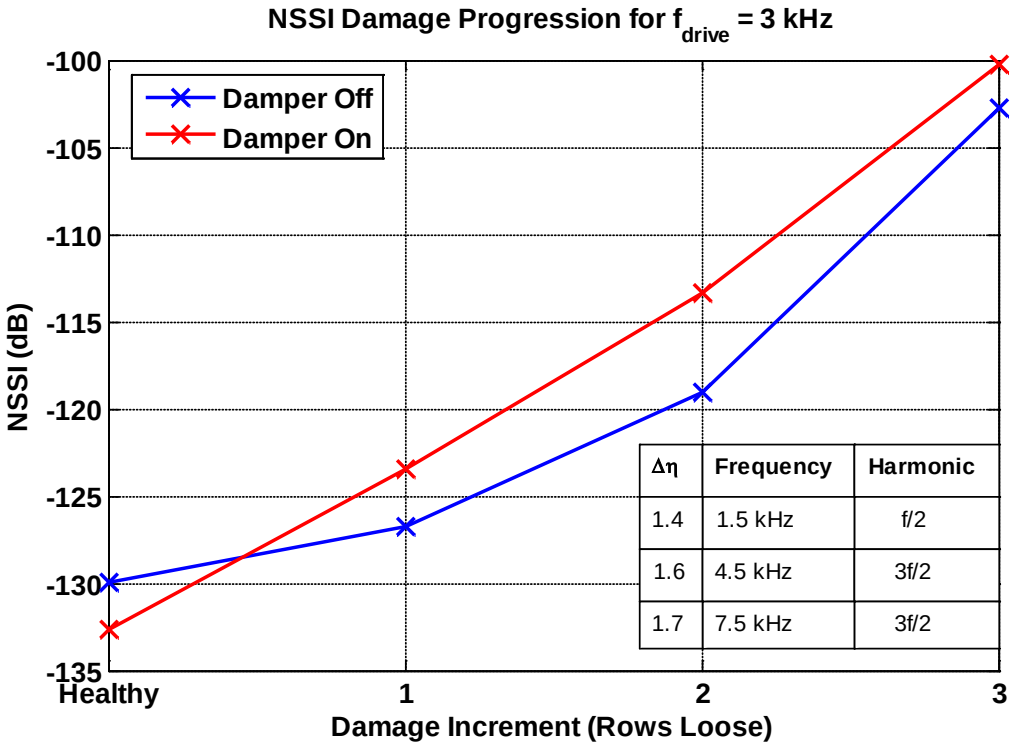

Figure 3-9: 3 kHz total NSSI results at each damage increment for a stiffened aluminum panel with and without added damping. The x-axis corresponds to the damage size (rows loose). A monotonic trend is seen for the damage progression at both damping conditions.

Results presented in Figure 3-9 show NSSI has a remarkable sensitivity to damage, and is able to accurately characterize a progression to each successive damage increment with a monotonic trend. A change of 27.2 dB was seen between the healthy and fully damaged case of 3 rows loose for the undamped case, and a larger change of 32.4 dB was present with the damper attached. Adding damping to the structure appears to make NSSI display a stronger monotonic trend, which is promising for the metric to be applied to more complex airframe structures with varying damping characteristics.

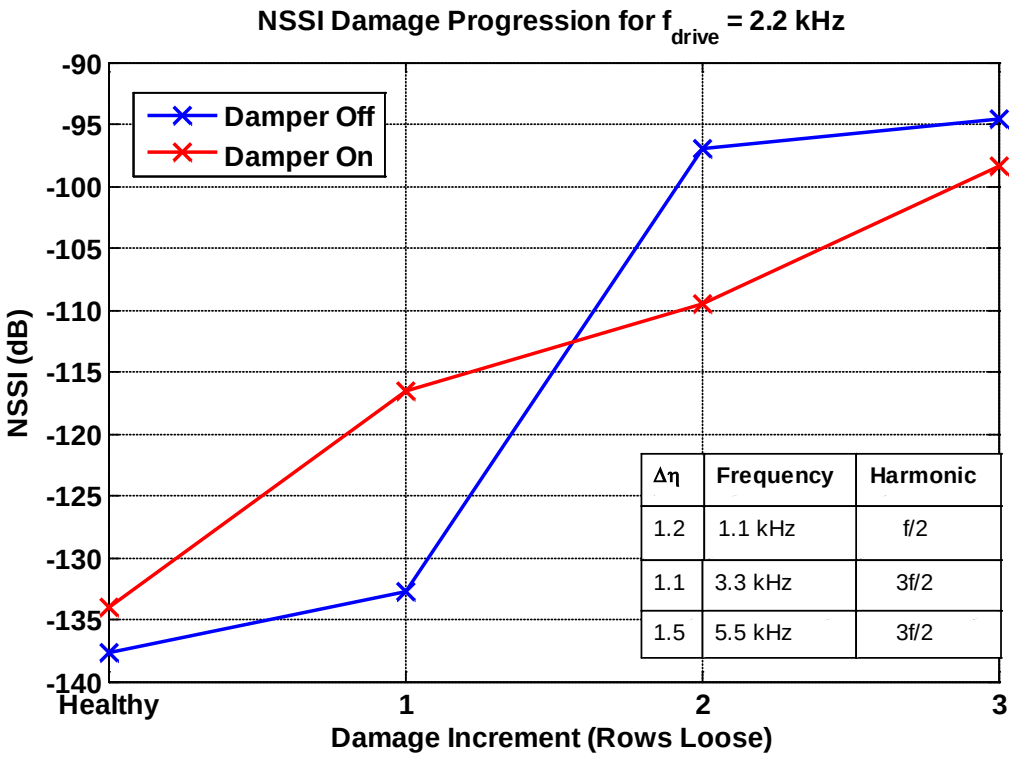

Figure 3-10: 2.2 kHz total NSSI results at each damage increment for a stiffened aluminum panel with and without added damping. The x-axis corresponds to the damage size (rows loose). A monotonic trend is seen for the damage progression at both damping conditions.

As expected, NSSI is again a monotonic function of the damage extent with f_{drive} = 2.2 khz (Figure 3-10), and this trend is relatively independent of the damping condition on the structure. A decrease in the detection of the smallest damage increment was present without the damper attached for this driving condition. This driving condition however, offered a larger overall sensitivity (43.1 dB undamped, 35.65 dB damper added) than what was previously presented in Figure 3-9.

In both cases, the addition of a point damper made NSSI display a *stronger* monotonic trend, and a remarkable sensitivity to damage. These results imply NSSI is a robust detection metric, and can be applied to structures with varying levels of damping while still maintaining a high detection strength and a monotonic relationship to the damage extent. These advantages, as

well as a small sensor footprint, make NSSI an attractive metric for complex flight vehicle structures.

3.3.3 NSSI Results for the Composite Stiffened Panels

Composite materials in particular are becoming more prevalent within the aerospace industry, and are desirable because they exhibit a high strength/stiffness while still being lightweight. Most composite materials however, will exhibit a higher level of distributed damping and display different relevant damage types from metallic structures, possibly making intensity-based damage detection metrics difficult to apply. Previous results in Section 3.3.2 proved the detection strength of NSSI is relatively independent of damping provided by a constrained layer beam attached as a point damper to an aluminum stiffened panel. The level of damping present on this test bed however, is much less than what would be seen on a composite airframe structure. In addition, the energy flow through composite materials can be very complex due in part to how the fibers are woven.

In order to examine the effectiveness of NSSI on composite stiffened panels, several experiments were performed utilizing the test beds described in Section 2.4.2 and pictured in Figure 2-13 and Figure 2-14. Two panels were tested, with damage introduced into one as a 1” delamination present at the termination of the stiffener. Excitation was provided in the out of plane direction by an electrodynamic/piezoelectric shaker pair. Consistent with measurements from the aluminum stiffened panel, the damaged composite panel exhibited a similar nonlinear behavior, with sub and ultra-subharmonics visible at a variety of different frequencies. Results show NSSI can be used to detect delaminations in the bond line of an integrally stiffened composite plate structure with a high degree of sensitivity. NSSI results for single tone harmonic

excitations of 2600 Hz (using the F4 electrodynamic shaker) and 3100 Hz (using the F7 piezoelectric shaker) are presented in Figure 3-11 and Figure 3-12 respectively.

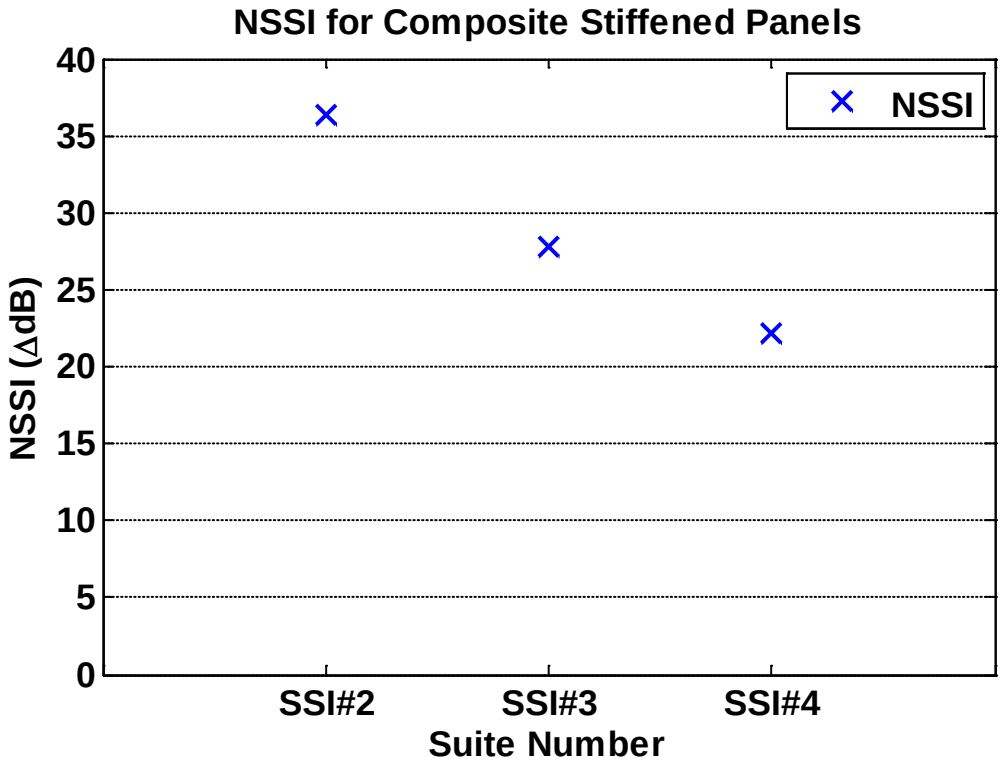

Figure 3-11: NSSI detection strength for a drive frequency of 2.6 kHz at a drive amplitude of 1.05 A. Results prove NSSI is able to detect a 1" delamination present in the bond line of the composite stiffener to a high degree of sensitivity.

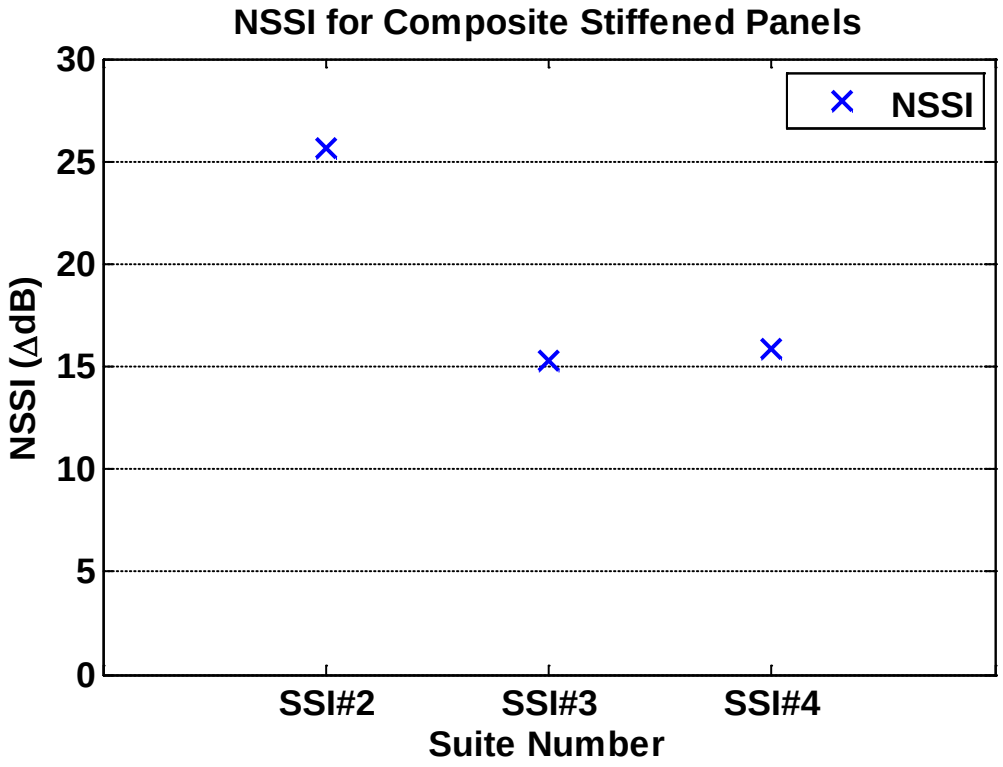

Figure 3-12: NSSI detection strength for a drive frequency of 3.1 kHz and drive amplitude of 1.43Vpp. Results prove NSSI is able to detect a 1" delamination present in the bond line of the composite stiffener to a high degree of sensitivity.

The 1" delamination present in the bond line at the trunctation of the stiffener was detected with a high degree of sensitivity using NSSI at several different frequencies, as presented in Figure 3-11 and Figure 3-12. NSSI had a total detection strength (the sum of all sensor values) of 28.89 dB for the 2.6 kHz driving condition,, and 19.5 dB for the 3.1 kHz case. This reinforces the concept that NSSI is an extremely sensitive metric and can be applied to more complex airframe structures exhibiting higher levels of distributed damping, giving valuable insight into new applications for SI-based measurement techniques. Composite airframe structures are becoming increasingly common in the aerospace industry, and intensity based health monitoring techniques can play an important role in improving condition based maintenance programs already in place for composite airframes.

3.4 Hysteresis Results - Aluminum Stiffened Panel

Previous work [9-11] has shown that a CAN displays a high instability, and the sub-harmonic behavior created by the contact of the two surfaces at the damage location can be described as a parametric resonance. The presence of nonlinear sub-harmonic frequencies indicates the vibrations have transitioned to a region of instability [9]. When activated via single tone harmonic excitation, the parametric resonance displays a nonlinear hysteretic behavior. While operating in this region, amplitude changes high-to-low vs. low-to-high are not equivalent, and will display large and sudden changes. This behavior is due to the asymmetric dynamics occurring at the contact interface. As the system is excited, a phase difference occurs between the two contact surfaces, creating 'clapping' and causing nonlinear harmonics to appear.

One major positive attribute of the NSI and NSSI methods as implemented with a single interrogation frequency was that each could be implemented as a baseline free method [21]. This implementation however, requires careful selection of the excitation force and frequency to activate the CAN sub-harmonic response. Knowing the hysteresis characteristics of a structure, for applying the NSI and NSSI approaches, allows for specific selection of the ideal driving condition (force and frequency) that will give the strongest nonlinear response. Because nonlinear structural intensity methods rely on the presence of sub- and ultra-subharmonics created by damage, understanding the hysteresis behavior of the structure at these frequencies (with respect to both changing frequency and amplitude) has important implications for SI-based techniques to be implemented in an automated or semi-automated SHM system.

Hysteresis for the aluminum stiffened panel was first investigated by tracking the increasing raw amplitude response of the SSI suite accelerometers at the first three sub-harmonic

frequencies (f / 2, 3f / 2, 5f / 2) and the first two super harmonic frequencies ($2f$, $3f$) for a 3 kHz single tone harmonic excitation. The nonlinear harmonic response as a function of the fundamental frequency (f) amplitude is shown in Figure 3-13. The experiment looked at the only the largest damage increment (3 rows loose), and excitation was provided by the F4 electrodynamic shaker in the out of plane direction.

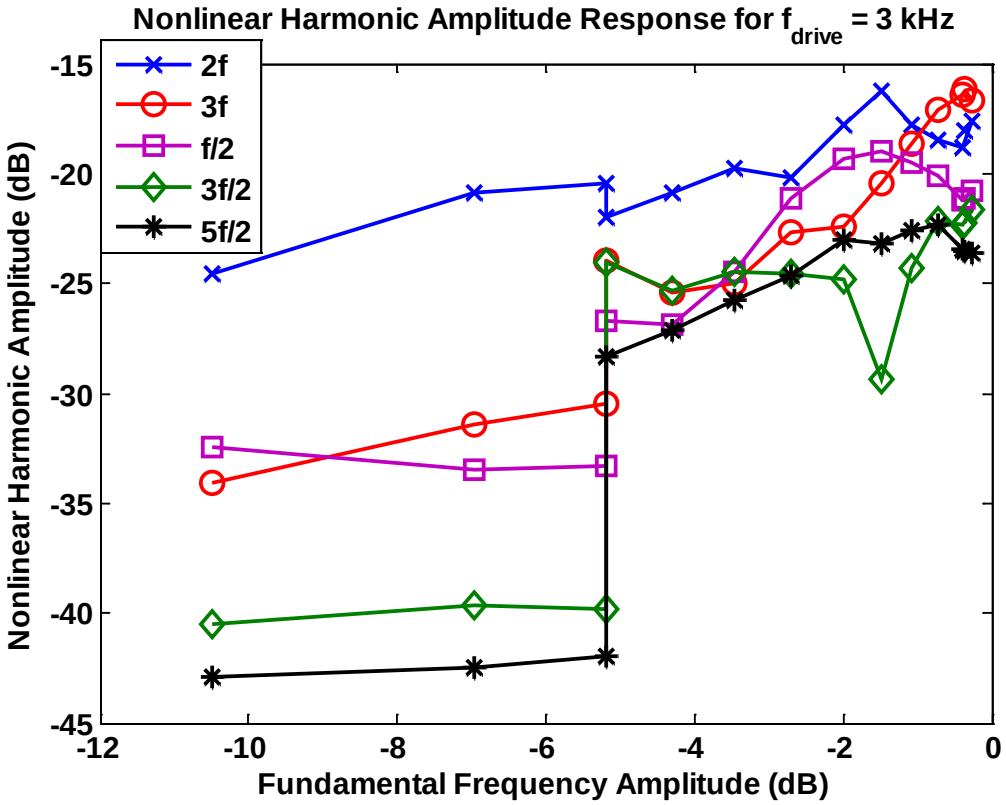

Figure 3-13: Nonlinear harmonic amplitude response of the aluminum stiffened panel for a driving frequency of 3 kHz. Note the large jump in amplitude (~15dB) for the sub-harmonic components, and relatively monotonic trend of the super-harmonic response.

Results illustrate that while both super-harmonic components have a relatively monotonic trend with no large jumps in response, the sub-harmonic frequency components display an extremely large change in response (~15dB) for a small change in driving amplitude (less than 1dB). This jump in response enables health monitoring via nonlinear SI-based metrics to be extremely sensitive, but also very difficult to use. Health monitoring via tracking changes in the

super harmonics may provide a more stable response, but these frequencies are corrupted by harmonic distortion in the drive signal, and cannot be implemented as a “baseline-free” metric. For these reasons, only changes in fractional harmonics ($nf\ /\ 2$) were monitored with nonlinear SI methods.

Finding the ideal driving condition, even when knowing the hysteresis characteristics of the structure, can require judicious selection amplitude to activate CAN. Because nonlinear SI methods rely on an inherent physical instability, they could be potentially difficult to use in an automated SHM system. Rather than simply relying on changes in the raw amplitude response of a single nonlinear harmonic component, NSSI combines these into a single metric displaying high sensitivity while still retaining a relation to the mechanical power flow in the structure. However, because NSSI relies on detecting the nonlinear sub-harmonics created by CAN, understanding the structure’s response to both frequency and amplitude hysteresis warranted further study. Using NSSI to track the amplitude hysteresis of the panel provided a stronger indication of when CAN was occurring than simply tracking amplitude changes in individual sub-harmonic components. Results tracking the amplitude hysteresis of the aluminum stiffened panel via NSSI are presented in Figure 3-14 for a single tone harmonic excitation of 3 kHz at the maximum damage extent of 3 rows loose.

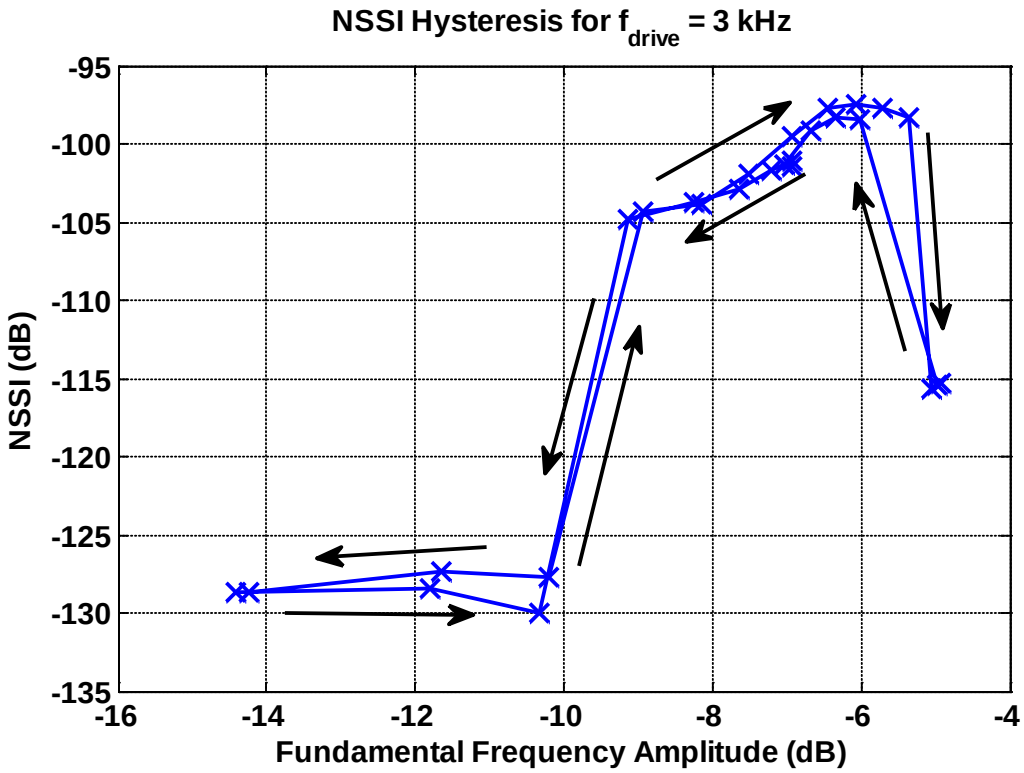

Figure 3-14: Nonlinear hysteresis curve of a stiffened aluminum panel for a single tone excitation f_{drive} = 3 kHz with 3 rows of stiffener bolts loose. Note the large jump in response between at fundamental frequency amplitude -10dB. The complexity of triggering the CAN sub-harmonics make it more selective for determining the ideal drive conditions for active interrogation.

Results show a large change in NSSI occurs (~25dB) as the fundamental frequency amplitude increases from -10dB to -9dB due to the inherent instability of the CAN mechanism to the applied force. Additionally, the decreasing amplitude response did not roll off smoothly as expected [11]. Instead, once the activation amplitude for CAN was reached, the response decreased to a similar level for what was measured while increasing the drive amplitude. Because of sudden change in response amplitude, it can potentially be difficult to determine the ideal amplitude needed to trigger the damage indicative vibration response nonlinearities in the system during active interrogation.

Additionally, activation of the CAN sub-harmonic response is heavily dependent on the chosen driving frequency. While it is possible to choose potential interrogation frequencies

corresponding to the damage size, these are only educated guesses, and can require slight changes to find the ideal driving condition to activate the strongest nonlinear response. To examine CAN's dependence on driving frequency, the stiffened aluminum panel was driven at constant amplitude (.734 A) for a frequency range from 2800 Hz to 3200 Hz at 50 Hz increments. Results for the frequency sensitivity study are presented in Figure 3-15, and are representative of only the largest damage increment (3 rows loose).

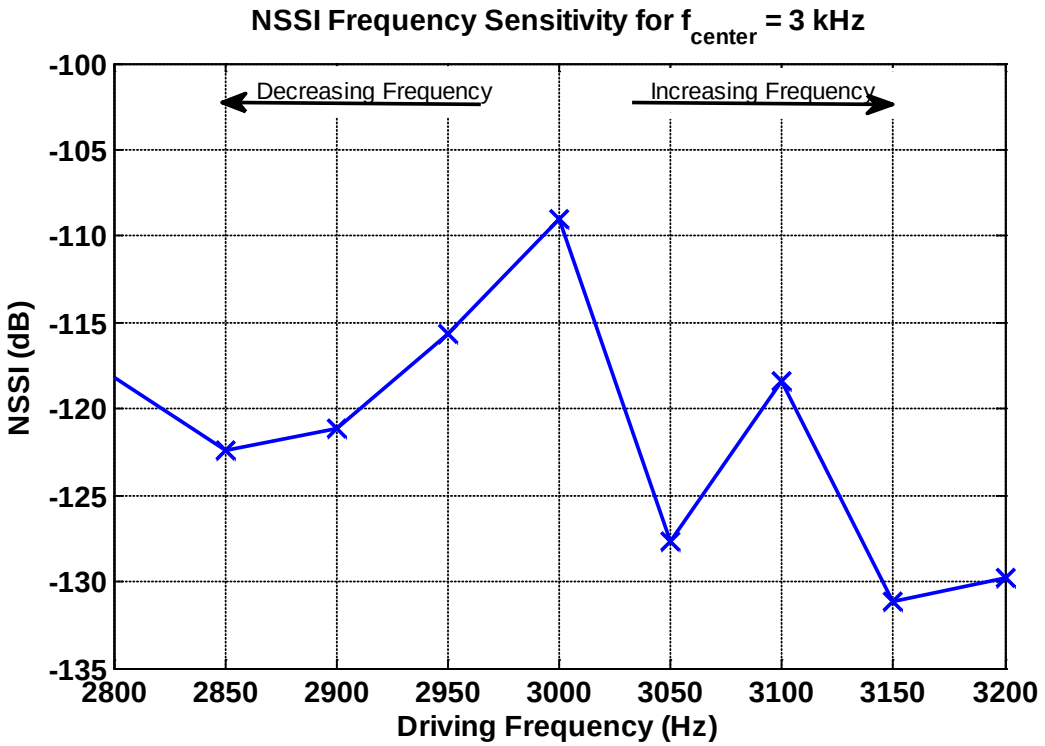

Figure 3-15: Aluminum stiffened panel frequency sensitivity tracked via NSSI at a constant amplitude of .734 A. Note the large decrease in response as the driving frequency moves away from 3000 Hz.

It is evident from the results that activation of CAN sub-harmonics is heavily dependent on the driving frequency. A large decrease (~25dB) is seen when evaluating NSSI even 50 Hz away from the ideal driving frequency. These results can be correlated with the damage progression NSSI trend presented previously in Figure 3-9. If the NSSI level at 3kHz is indicative of a damage condition of 3 rows loose, moving 50 Hz away from the optimal driving frequency

reduces this detection to the level of 1 row loose. This plays a major role for NSSI's implementation in automated SHM systems. If the frequency or amplitude choice of a single tone interrogation signal are slightly different from the ideal driving condition, a damage signature might not be detected, leaving the structure vulnerable to failure.

Because the single tone approach is very selective with respect to driving conditions, a new method was developed utilizing Nonlinear Modulated Wave Spectroscopy (NWMS) to form a more stable approach that still retains the high sensitivity and physical meaning of NSSI. This metric, denoted Nonlinear Structural Surface Intensity – Modulated Wave (NSSI-MW), utilizes two interrogation waves, and relies on detecting the interactions (in the form of combinational frequencies) created as they excite a nonlinear damage feature. This hybrid technique is examined in more detail on a variety of test beds in Chapter 4.

Chapter 4

Hybrid Techniques – Investigation of Nonlinear Damage Features via Nonlinear Wave Modulation Spectroscopy

4.1 Introduction

Previous results proved NSSI is a high sensitivity metric which can be used to detect multiple types of relevant damage to airframe structures. Because NSSI relies on detecting the nonlinear harmonics created by the CAN sub-harmonic response (an inherent instability), finding the ideal driving conditions (force and frequency) to create the strongest nonlinear response on the structure can be challenging. This makes the single tone approach hard to implement on in-situ airframe structures, even when knowing their hysteresis characteristics. This led to the development of a new damage detection metric combining nonlinear wave modulation spectroscopy (NWMS) and SI-based health monitoring technology into the new metric known as Nonlinear Structural Surface Intensity – Modulated Wave (NSSI-MW).

NSSI-MW is a hybrid technique, and combines the methods developed within the fields of nonlinear acoustics and noise control/vibrations to form a novel approach to damage detection that is more stable, but still retains the high sensitivity and physical meaning of NSSI. This technique utilizes two interrogation (drive) waves, and relies on detecting the interactions (appearing as combinational frequencies) created as a nonlinear damage feature is excited. To investigate the potential damage detection sensitivity of this new metric, results comparing both the single-tone and modulated wave techniques are presented in this Chapter. Damage detection results and hysteresis characteristics of the aluminum stiffened panel test bed tracked via NSSI-MW are covered in Section 4.2, and a comparison of the relative sensitivity for the single-tone to modulated wave approach on the composite stiffened panels is presented in Section 4.3.

4.2 NSSI-MW Results - Aluminum Stiffened Panel

4.2.1 NSSI-MW Damage Progression Trends

To quantify the damage detection and sensitivity of the modulated approach, NSSI-MW damage progression trends were evaluated on the aluminum stiffened panel test bed, and compared to results tracking damage progression as a function of NSSI. An example of an example sensor spectra for modulated wave interrogation frequencies of f_{high}=3 kHz and f_{low}=500 Hz is presented in Figure 4-1. The damaged spectrum (red) is rich with multiple wave interactions created by the nonlinear damage feature at the center of the panel. Large changes can be seen between the healthy and damaged conditions at the sidebands compared to the relatively small changes in the driving frequencies. Also present in this case are sub- and ultra-subharmonics from the low driving frequency. Note that while these sub-harmonics are indicative of damage, they are not used as damage indicators in the NWMS approach. Only the combinational tones present from the wave interactions are used in the NSSI-MW calculation (see Figure 2-8).

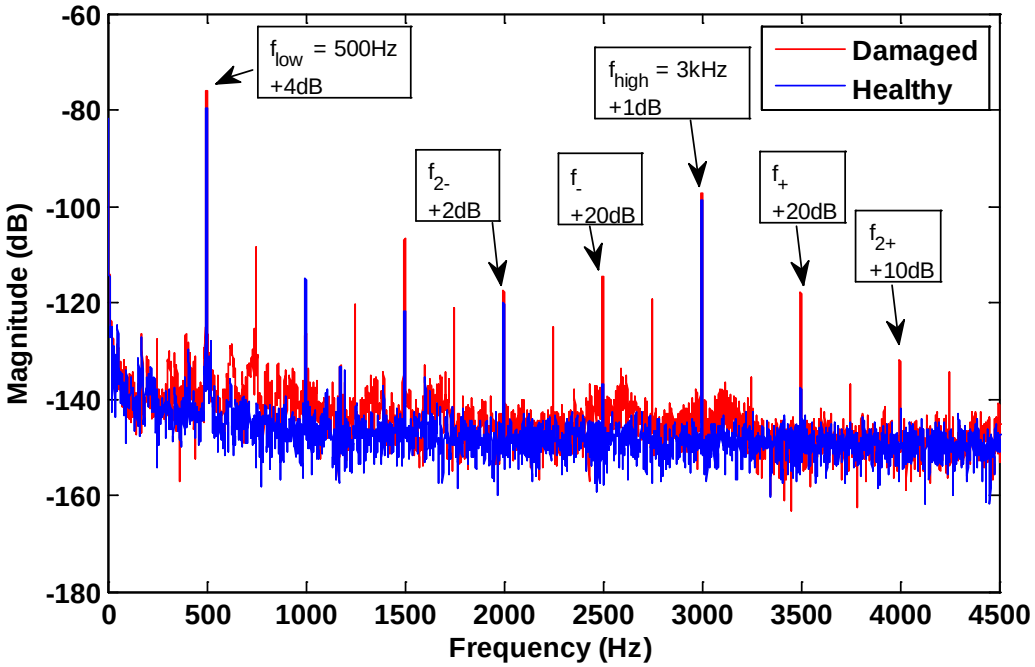

Figure 4-1: Healthy and damaged (3 rows loose) strain spectra from SSI suite #2 ε_x for a modulated wave interrogation signal f_{high}=3 kHz and f_{low}=500 Hz. Note the large changes in first-order combinational tones f_+ and f_- between the healthy and damaged conditions.

Since the presence of these combinational tones is indicative of a nonlinear damage feature, NSSI-MW can be used to evaluate its severity. To accomplish this, the aluminum stiffened panel was interrogated with modulated wave input signals (collocated shakers) at several different frequencies, and for various damage conditions. Similar to the single-tone interrogation approach, damage was again introduced as loose bolts at the center of the stiffener (simulating the presence of a loose rivet). Each successive damage increment loosened 1 row of fasteners, with a maximum of 3 rows of bolts loose (footprint of 8 inches). Results tracking NSSI-MW for driving conditions of f_{low} = 500 Hz / f_{high} = 3 kHz f_{low} = 500 Hz / f_{high} = 4 kHz are presented in Figure 4-2 and Figure 4-3 respectively. Each of the modulated wave cases are compared to the single tone results previously shown in Section 3.2. For both of the modulated wave driving conditions, parameters were arbitrarily chosen, and were not optimized for either frequency or amplitude.

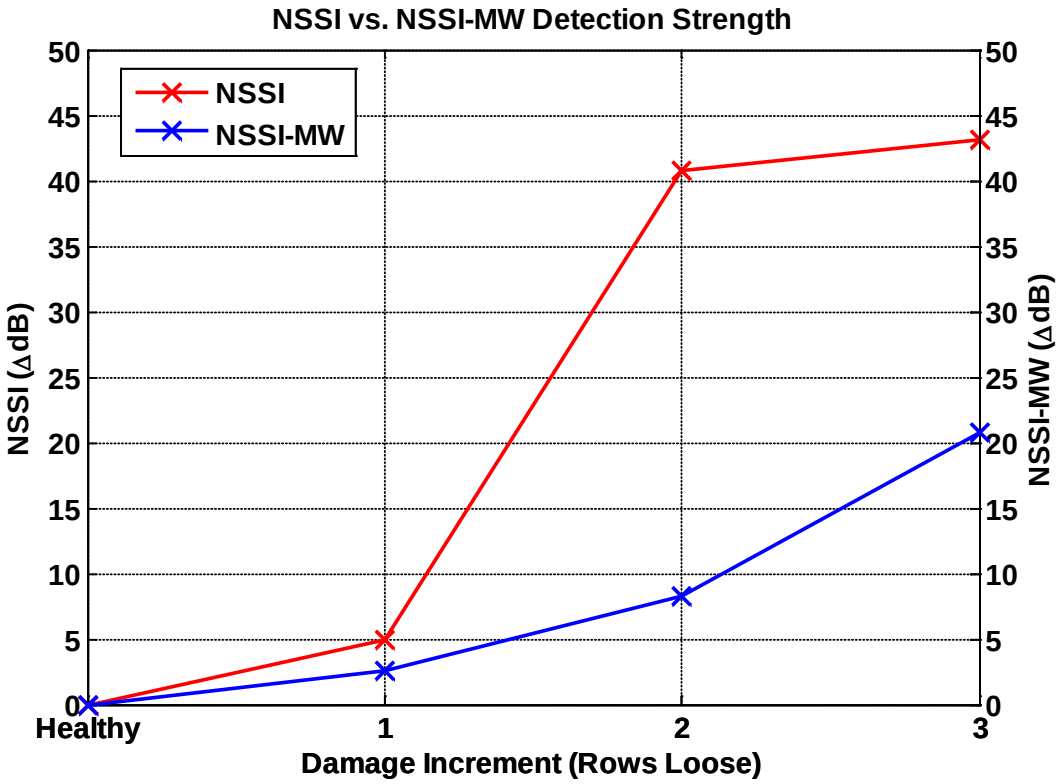

Figure 4-2: NSSI-MW Damage progression trend (blue line) for a modulated wave interrogation signal f_{high}=4 kHz and f_{low}=500 Hz. Results from the single tone interrogation frequency of f_{drive} = 2.2 kHz (red line) are overlayed. Note while both metrics are able to characterize damage, NSSI-MW displays a lower overall sensitivity.

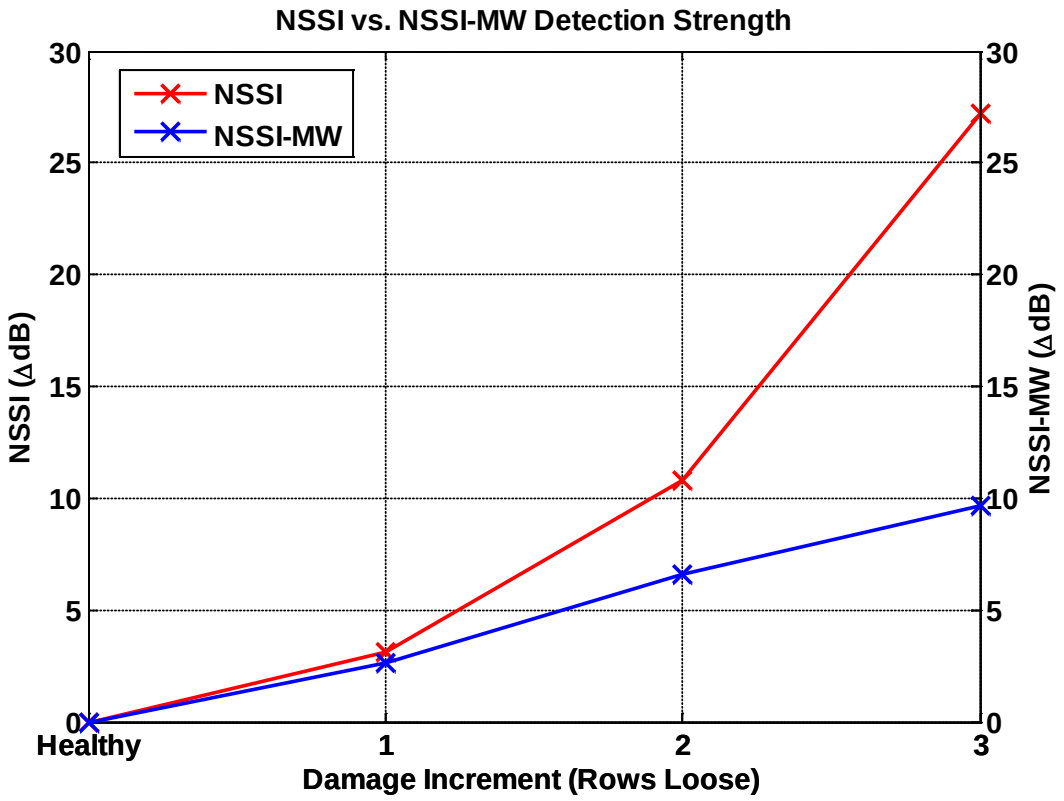

Figure 4-3: NSSI-MW Damage progression trend for a modulated wave interrogation signal f_{high}= 3 kHz and f_{low}= 500 Hz. Results from the single tone interrogation frequency of f_{drive} = 3 kHz (red line) are overlayed. Note while both metrics are able to characterize damage, NSSI-MW displays a lower overall sensitivity.

Results show that like the single tone approach, NSSI-MW is monotonic function relative to the damage extent. However, the relative sensitivity of the NSSI-MW metric is lower, as the single tone interrogation method displays an overall sensitivity anywhere from ~2-3 times greater than NSSI-MW. The change in NSSI vs. NSSI-MW for the driving conditions shown in Figures 4-2 and Figure 4-3 is presented in Table 4-1 and Table 4-2 respectively.

Table 4-1: Overall sensitivity of NSSI vs. NSSI-MW for the driving conditions presented in Figure 4-2.

	NSSI (dB)	**NSSI-MW (dB)**
Healthy	-137.7	-114.0
3 Rows Loose	-94.6	-93.2
ΔdB	43.1	20.8

Table 4-2: Overall sensitivity of NSSI vs. NSSI-MW for the driving conditions presented in Figure 4-3.

	NSSI (dB)	**NSSI-MW (dB)**
Healthy	-129.9	-100.9
3 Rows Loose	-102.7	-91.3
Δ dB	27.2	9.6

NSSI had a total detection strength (the sum of all sensor values) of 43.1 dB for the 2.2 kHz driving condition, and 27.2 dB for the 3 kHz case. In comparison NSSI-MW had a total detection strength of 20.77 dB for the f_{high}=3 kHz / f_{low}=500 Hz driving condition, and 9.64 dB for the f_{high}=4 kHz / f_{low}=500 Hz case. Despite the loss in sensitivity, NSSI-MW is still able to accurately characterize the damage progression trend, and using a modulated wave active interrogation signal proved to be less selective with respect to driving conditions to induce a nonlinear response. Both the frequency and amplitude parameters for the single tone approach need to be finely tuned, and operate on very sensitive hysteresis curves.

While NSSI-MW has a lower overall sensitivity to damage, the metric shows strong detection of the maximum damage increment, even with relatively arbitrarily chosen frequencies and amplitudes. This shows the modulated wave approach could be a more stable method to interrogate nonlinear damage features. The stable response and monotonic relationship to damage (regardless of the choice for driving conditions) make NSSI-MW a promising technique for use with automated SHM systems.

4.2.2 NSSI-MW Hysteresis Characteristics

Use of a modulated wave input was anticipated to provide an alternate approach that would offer the benefit of being less selective to the drive condition(s), but still maintain the

robust characteristics of the NSSI metric. Section 3.4 proved that CAN activated with a single-tone excitation operates on a very unstable hysteresis curve. Amplitude changes back and forth were not equivalent, and large and sudden changes were seen in the response for a small increase in driving force. Results in Section 4.2.1 showed that NSSI-MW was less sensitive than NSSI, but was able to detect damage with a high sensitivity with arbitrarily chosen driving conditions. This implied that the modulated wave approach was a more stable interrogation method, and was less selective of driving conditions than the single-tone approach.

To fully understand the hysteresis characteristics of nonlinear damage features excited by a modulated wave active interrogation, the hysteresis of the aluminum panel was tracked via NSSI-MW measurements with respect to both frequency and amplitude changes. These experiments looked at the only the largest damage increment (3 rows removed), and excitation was provided by an electrodynamic shaker in the out of plane direction. Results tracking NSSI-MW for changes in amplitude are presented in Figure 4-4 for an excitation of f_{high}= 6 kHz / f_{low}= 1 kHz. This driving condition was again chosen arbitrarily to reinforce the assumption that the damage indicative nonlinear response is much less selective to driving conditions when actively excited using a modulated wave interrogation signal.

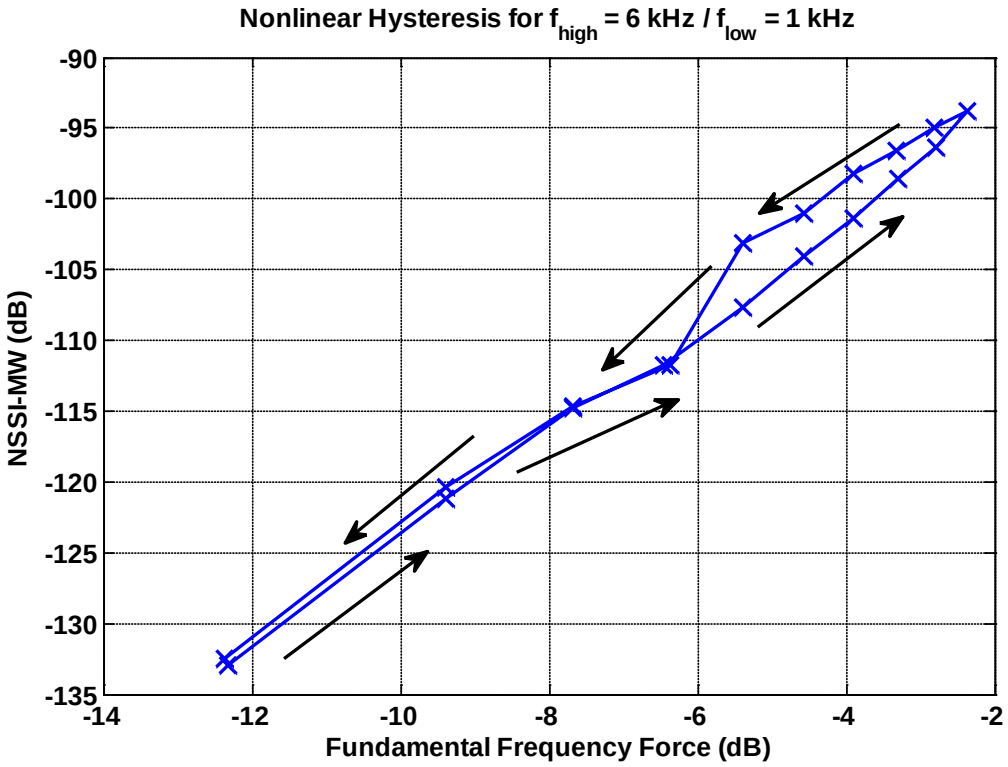

Figure 4-4: Nonlinear hysteresis curve for driving frequencies f_{high}= 6 kHz / f_{low}= 1 kHz (varying the amplitude of f_{high}). Note the very stable response, with no sudden changes in response for any change in amplitude.

The nonlinear hysteresis curve presented in Figure 4-4 shows a remarkably stable trend, with no sudden changes in amplitude present anywhere within the measured range. As the driving conditions were again chosen arbitrarily, and not optimized for detection strength in any way, these results show promise for NSSI-MW to be used within an automated SHM system. To directly compare the hysteresis response of the modulated wave approach to the single-tone approach, NSSI-MW was tracked for driving frequencies of f_{high}= 3 kHz / f_{low}= 500 Hz (Figure 4-5). The results are presented against the NSSI frequency response for f_{drive}= 3 kHz (previously presented in Figure 3-14).

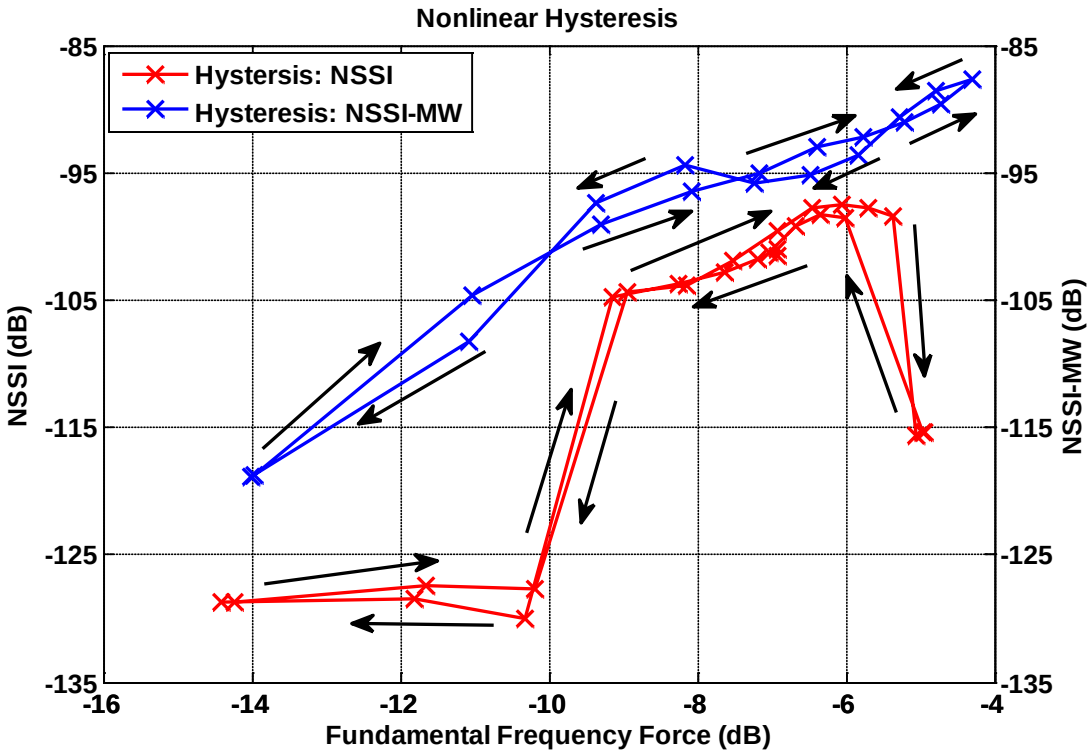

Figure 4-5: Nonlinear hysteresis curve of a stiffened aluminum panel for a single tone excitation f_{drive} = 3 kHz and modulated wave excitation f_{low}=500 Hz, f_{high} = 3 kHz (varying the amplitude of f_{high}). Note the large jump in response between at a fundamental frequency force of -9dB for the single tone harmonic excitation, compared to the relatively stable response of NSSI-MW.

As seen previously, the single tone approach exhibits a large jump in response for a slight change in drive amplitude due to the inherent instability of the CAN sub-harmonic response mechanism to the applied force. Because of this, it can potentially be difficult to determine the ideal amplitude needed to trigger the damage indicative vibration response nonlinearities in the system during active interrogation. However, the NSSI-MW hysteresis displays a much more stable response (even with arbitrarily chosen driving conditions). This reinforced the assumption that modulated wave interrogation may be a more robust SHM technique.

To determine the frequency dependence of the aluminum stiffened panel using a modulated wave excitation, the NSSI-MW response was also tracked (varying the frequency of f_{high}). NSSI results in Section 3.4 proved the activation of CAN is heavily dependent on the

chosen driving frequency. NSSI-MW is anticipated to be more stable with respect to frequency, as no optimization was needed for the metric to detect damage. To examine the frequency hysteresis for a modulated wave active interrogation, the stiffened aluminum panel was driven at constant amplitude for a frequency range from 2800 Hz to 3200 Hz at 50 Hz increments. Results are presented in Figure 4-6, and are representative of only the largest damage increment (3 rows loose). Additionally, results from the single-tone approach (presented previously in Figure 3-15) are overlaid to provide a comparison between both methods of interrogation.

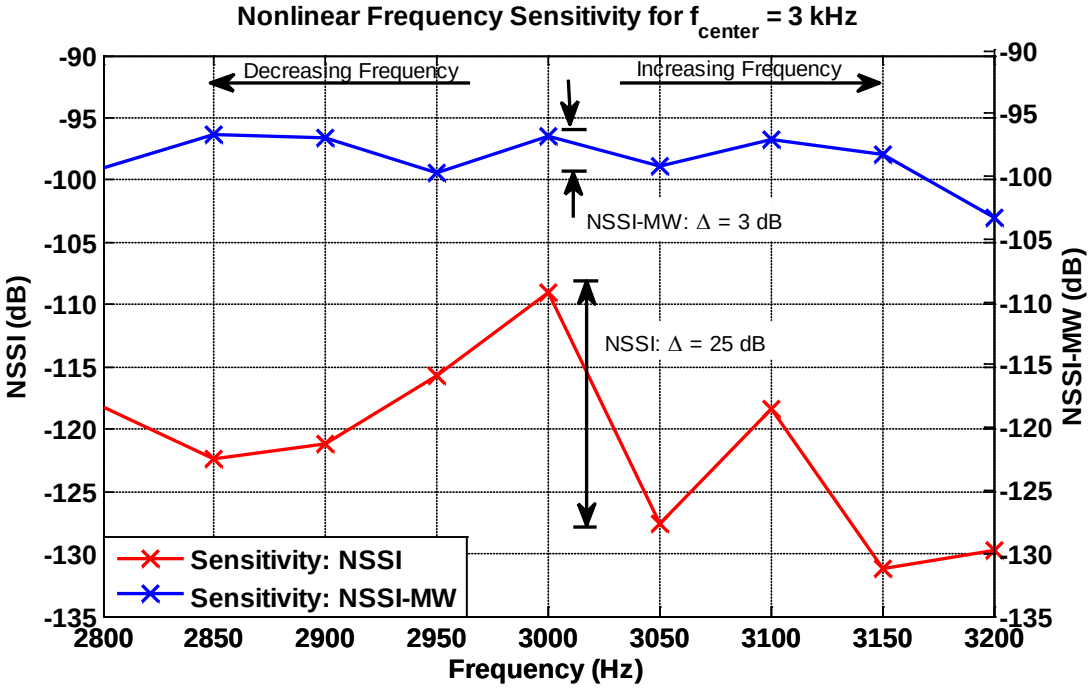

Figure 4-6: Aluminum stiffened panel frequency sensitivity tracked via NSSI-MW with driving conditions fhigh= 3 kHz / flow= 500 Hz (varying f_{high}). Note the relatively small changes in NSSI-MW as compared to the large decrease in response of NSSI as the driving frequency moves away from 3000 Hz.

It is evident from the results that the modulated wave performance is much less selective with respect to interrogation/drive frequency choice than the single tone approach. NSSI-MW displays a relatively flat response over the entire frequency range, and is at the level of detection for 3 rows of loose bolts (as presented in Figure 4-2), with fluctuations less than 3 dB for all

increments. In comparison, a large decrease (~25dB) is seen when evaluating NSSI even 50 Hz away from the ideal driving frequency, confirming the assumption that the modulated approach is much more stable method of interrogation with respect to frequency choice.

These results have a major positive implication towards implementing SI-based damage detection metrics relying on the modulated wave interrogation technique in automated SHM systems. The complexity of triggering a CAN make it more selective for determining the ideal drive conditions for active interrogation (with respect to both force and frequency). Using a modulated wave interrogation signal allows for much less selective drive conditions for active damage detection, and still shows a strong detection of the nonlinear damage feature. This makes NSSI-MW an attractive metric for practical airframe implementation. While the damage indicative nonlinear response may be easier to trigger with a modulated wave, it may require a baseline approach due to nonlinear effects from the drive / actuator system.

4.3 NSSI-MW Results - Composite Stiffened Panels

Previous results in Section 3.3.3 proved NSSI is a high sensitivity metric that can be applied to composite stiffened panels. Composite materials are becoming increasingly common within the aerospace industry, and the detection capability of the NSSI-MW metric warranted investigation on these materials. Previous results in Section 4.2 showed that NSSI-MW is a high sensitivity metric that is less selective to driving conditions than NSSI. Section 3.3.2 showed that intensity-based SHM techniques were able to be applied to composite materials, and were successful in detecting damage in the form of a delamination in the bond line of an integrally stiffened composite panel. In order to examine the effectiveness of NSSI-MW applied to composite materials, several experiments were performed utilizing the test beds described in Section 2.4.2 and pictured in Figure 2-13 and Figure 2-14.

Excitation was provided in the out-of-plane direction by an electrodynamic/piezoelectric shaker pair. Consistent with measurements from the aluminum stiffened panel, the damaged composite panel exhibited a similar nonlinear behavior under modulated wave excitation, with combinational tones visible for a variety of frequency pairs. Results prove NSSI-MW can be used to detect relevant damage types on a stiffened composite plate structure with a high degree of sensitivity. NSSI-MW results for modulated wave excitations of f_{low} = 700 Hz / f_{high} = 5.7 kHz and f_{low} = 900 Hz / f_{high} = 5 kHz are presented in Figure 4-7 and Figure 4-8 respectively. Overlaid for comparison are results for a single tone active interrogation, originally presented in Figure 3-11 and Figure 3-12. Driving conditions for the modulated wave excitation were again chosen arbitrarily, with no optimization performed for either frequency or driving amplitude.

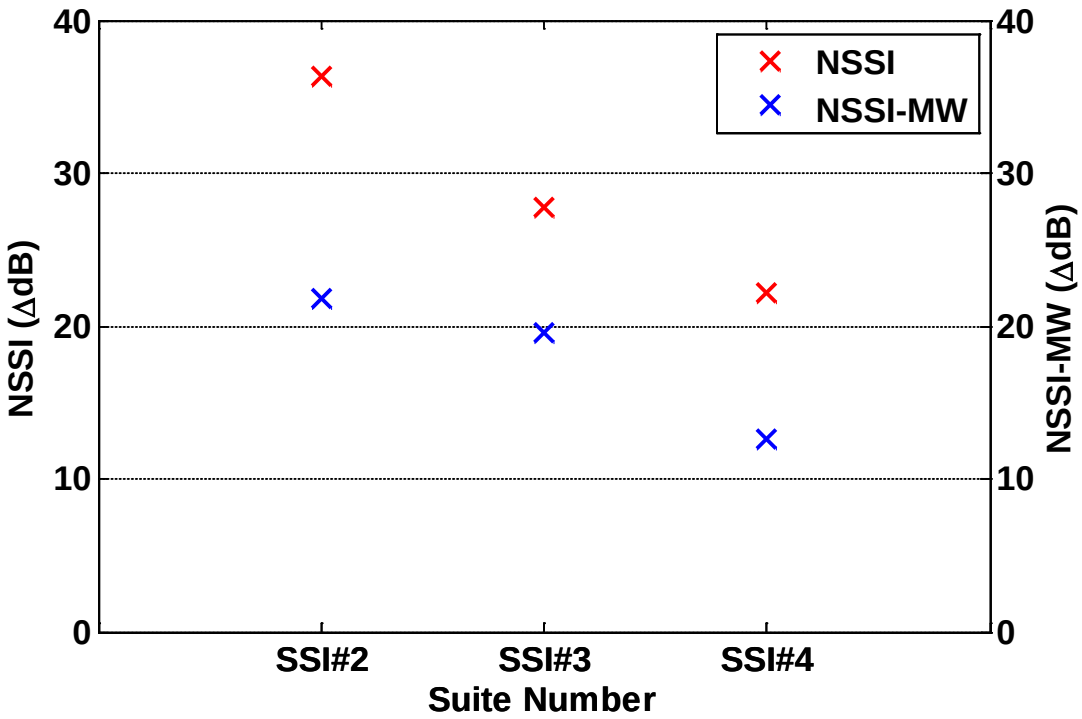

Figure 4-7: Stiffened composite panel change in NSSI for f_{drive} = 2.6 kHz vs. change in NSSI-MW for f_{low} = 700Hz, f_{high} = 5.7 kHz. NSSI displays a greater change between healthy and damaged cases, but is much more sensitive to frequency and amplitude selection. NSSI-MW displays less change between healthy and damaged cases, but is less selective with respect to drive frequency and amplitude.

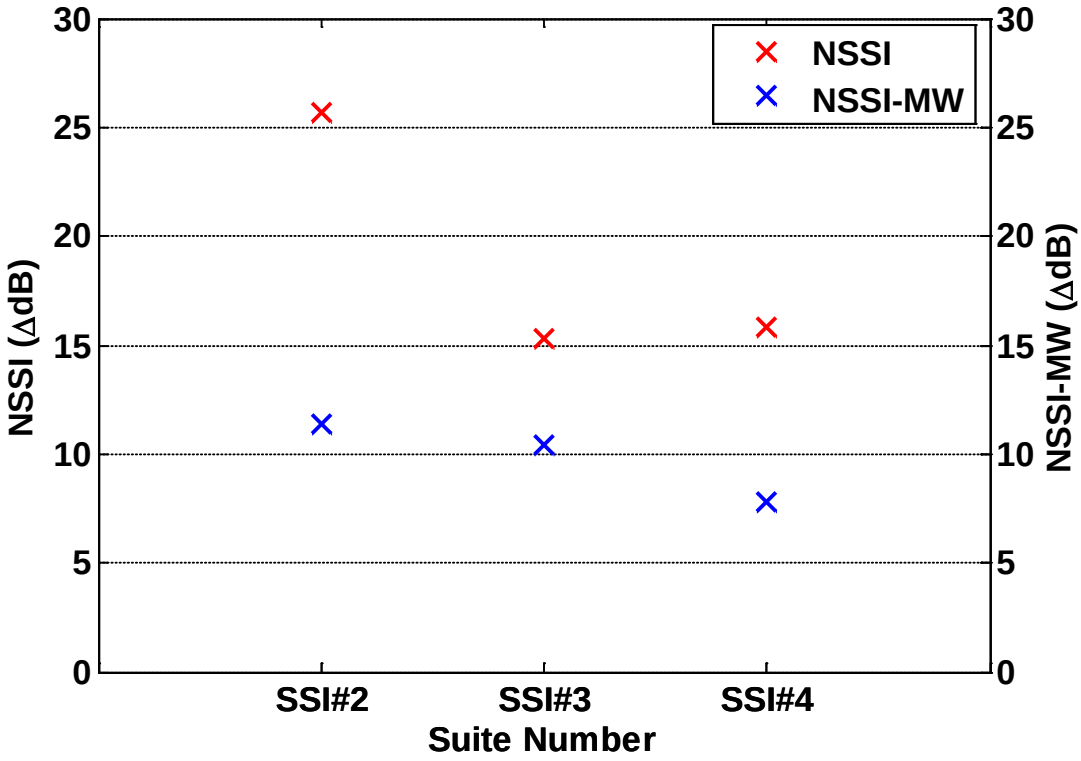

Figure 4-8: Stiffened composite panel change in NSSI for f_{drive} = 3.1 kHz vs. change in NSSI-MW for f_{low} = 900Hz, f_{high} = 5 kHz. NSSI shows a greater change between healthy and damaged cases, but is much more sensitive to frequency and amplitude selection. NSSI-MW displays less change between healthy and damaged cases, but is less selective with respect to drive frequency and amplitude.

Results in Figure 4-7 and Figure 4-8 prove the 1" delamination present in the bond line at the trunctation of the stiffener was detected to a high degree of sensitivity using NSSI-MW with several different frequencies pairs. While both metrics are able to detect damage, NSSI had higher detection strength than NSSI-MW in both cases. The change in NSSI vs. NSSI-MW at each sensor suite for the driving conditions shown in Figure 4-7 and Figure 4-8 is presented in Table 4-4 and Table 4-3 respectively.

Table 4-3: Sensitivity of NSSI vs. NSSI-MW for the driving conditions presented in Figure 4-7.

	NSSI (ΔdB)	**NSSI-MW (ΔdB)**	**Difference (ΔdB)**
SSI#2	36.36	21.79	14.57
SSI#3	27.77	19.56	8.21
SSI#4	22.13	12.65	9.48

Table 4-4: Sensitivity of NSSI vs. NSSI-MW for the driving conditions presented in Figure 4-8.

	NSSI (ΔdB)	**NSSI-MW (ΔdB)**	**Difference (ΔdB)**
SSI#2	25.68	11.4	14.28
SSI#3	15.32	10.42	4.89
SSI#4	15.82	7.78	8.03

A clear difference can be seen between the detection strength of the single tone approach compared to the modulated wave method. While NSSI is able to detect damage with an extremely high sensitivity, it relies on careful selection of driving conditions to trigger the characteristic nonlinear response of CAN sub-harmonics. NSSI-MW is able to detect damage to a high degree of sensitivity, and even though the overall detection strength is somewhat lower than NSSI, it is much less selective with respect to driving condition choice. This reinforces the assumption that NSSI-MW is a much more stable method of interrogation, and could potentially be implemented more easily in an automated SHM system.

The results presented in Chapters 3 and 4 explicitly show that intensity-based healthy monitoring techniques are extremely sensitive, and can be applied to more complex airframe structures. To fully investigate the damage detection potential NSSI and NSSI-MW on complex airframe structures, a set of experiments was completed on an OH-58D Kiowa Warrior tail boom. A summary of results from those experiments is presented in Chapter 5.

Chapter 5

Experimental Case Study: OH-58D "Kiowa Warrior" Tail Boom

5.1 Introduction

The need for SHM systems on rotorcraft is continuously increasing, as aging platforms require an ever increasing maintenance hour to flight hour ratio. The results presented in this work prove that intensity based-health monitoring metrics display a high sensitivity to damage on both composite and metal structures. These methods (both NSSI and NSSI-MW) aim to provide more extensive information for SHM systems that is critical to implementing a CBM approach. This allows for more efficient maintenance of critical rotorcraft systems, and reduces the associated cost and downtime of mission capable aircraft.

To perform a more rigorous evaluation of both the NSSI and NSSI-MW techniques on a complex airframe structure, an experimental case study was performed using an OH-58D Kiowa Warrior tail boom (Figure 2-15). This structure served as a metric comparison test bed, and was used to evaluate both NSSI/NSSI-MW and single sensor damage detection sensitivity with typical damage features seen on a real, complex airframe structure. Several changes were made to the structure for laboratory use, and are described in Section 2.4.3.

To fully investigate the potential damage detection sensitivity of the metrics developed in Chapters 3 and 4 on a real airframe structure, results comparing both the single-tone and modulated wave techniques are presented in this Chapter. In order to assess the potential increase in sensitivity the data fusion methods of NSSI/NSSI-MW offer, results on the tail boom are also compared to analogous single-sensor nonlinear metrics. The application of this single sensor technique for both Nonlinear Strain and Nonlinear Acceleration is developed in Section 5.2.

Section 5.3 covers the damage detection results of both NSSI and NSSI-MW, and their comparison results using only single sensors (acceleration and strain).

5.2 Single-Sensor Application: Nonlinear Strain (NLS) and Nonlinear Acceleration (NLA)

The discrete sensors (strain and acceleration) that make up an SSI suite (Figure 1-7) can also be used individually for nonlinear damage detection. These single-sensor metrics, denoted Nonlinear Strain (NLS) and Nonlinear Acceleration (NLA), are applied in a similar manner to NSSI and NSSI-MW in the frequency domain (see Section 2.3, Figures 2-8 and 2-9). Equations 5.1 and 5.2 describe how NLA/NLS are applied for a single tone interrogation, and Equations 5.3 and 5.4 describe how each metric is applied for a modulated wave interrogation signal.

$$NLA = \sum_{n=1,3,5} \frac{1}{\Delta f} \int_{\frac{nf}{2}-.01f}^{\frac{nf}{2}+.01f} [a_z{}^2]\, df \tag{5.1}$$

$$NLS = \sum_{n=1,3,5} \frac{1}{\Delta f} \int_{\frac{nf}{2}-.01f}^{\frac{nf}{2}+.01f} [\varepsilon_i{}^2]\, df \tag{5.2}$$

$$NLA - MW = \sum_{n=1,2,3} \frac{1}{\Delta f} \int_{(f_{high} \pm n f_{low})+.01 f_{low}}^{(f_{high} \pm n f_{low})+.01 f_{low}} [a_z{}^2]\, df \tag{5.3}$$

$$NLS - MW = \sum_{n=1,2,3} \frac{1}{\Delta f} \int_{(f_{high} \pm n f_{low})-.01 f_{low}}^{(f_{high} \pm n f_{low})+.01 f_{low}} [\varepsilon_i{}^2]\, df \tag{5.4}$$

The use of single sensors offers several distinct simplifications. The formulation of the nonlinear metric is much less complicated than using SI-based measurement techniques; instead

of evaluating the active energy flow through the structure, single-sensor metrics look at the total vibration field at a single point (active and reactive). Since weight and space savings are a major concern for flight vehicles, the relatively small sensors needed for the calculation can be placed in flexible locations without taking up valuable space needed for other equipment. In addition, single-sensors use less power than a typical 5-channel SSI suite, causing less burden on the data acquisition system.

To evaluate the sensitivity of the single-sensor based methods against both NSSI and NSSI-MW, results comparing all metrics are presented for the OH-58 tail boom in Section 5.3.

5.3 Tail boom damage detection results

To evaluate the effectiveness of each nonlinear damage detection metric, exploratory measurements were performed on an OH-58 tail boom. SSI sensors were mounted at three locations on the structure, as well as several skin strain gages and accelerometers. Simulated damage was introduced by loosening bolts attaching hanger bearing brackets, and excitation was provided with several electrodynamic shakers and piezoelectric actuators mounted on the structure (see Figure 2-15). A typical response spectrum for an SSI suite strain gage is presented in Figure 5-1, comparing responses for both the healthy and damaged condition (rectangular PZT actuator drive).

Consistent with measurements taken on both the aluminum and composite stiffened panels, introducing this type of damage into the system creates a strong nonlinear sub-harmonic response. Additionally, the CAN sub-harmonic response was detected at the aft end of the structure, the farthest location from the damage. Damage was introduced for this case at Station 5, which is 66.5 inches away from the sensor location (Station 1). Detection results for each SSI

suite and individual sensors are presented in Figure 5-2 for all stations across the length of the structure.

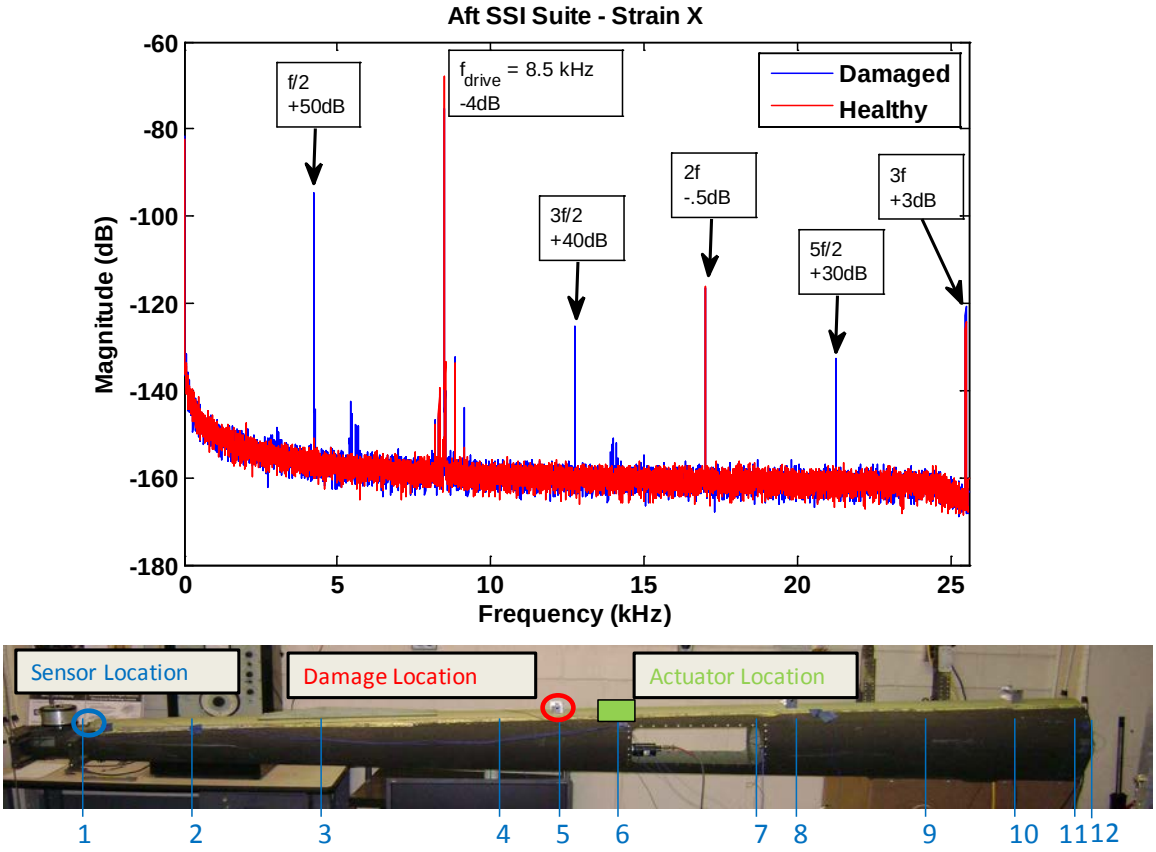

Figure 5-1: OH-58 tail boom strain sensor autospectra for f_{drive} = 8.5 kHz. Damage is introduced by loosening hanger bearing brackets. When the damage is present in the system, a strong nonlinear response occurs, creating sub and ultra-subharmonics

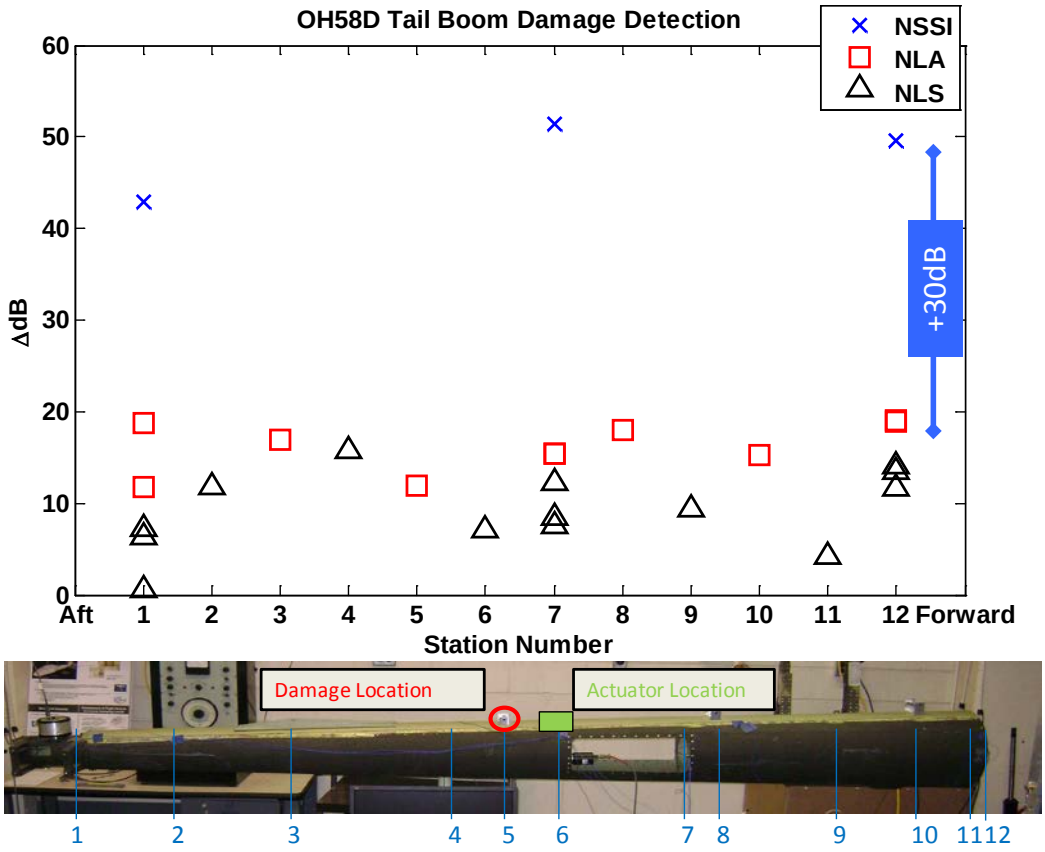

Figure 5-2: OH-58 tail boom NSSI, Nonlinear Strain, and Nonlinear Acceleration results for f_{drive} = 8.5 kHz with an embedded rectangular PZT actuator. NSSI has a much greater damage sensitivity via data fusion of the strains and accelerations vs. using strain or acceleration individually. Note damage is detected globally (all sensor locations) using an embedded actuator at station 6.

The damage detection results for a single tone drive presented in Figure 5-2 confirm that damage in the form of a loose hanger bearing bracket is detectable throughout the length of the structure. Additionally, while single-sensor NLA and NLS are able to detect the damage (showing on average ~15 dB detection strength), NSSI (active energy flow) has a much greater sensitivity, showing an increase of 30 dB over single-sensor NLA and NLS (total vibration field) metrics. These results imply that NSSI is able to detect damage with a much higher degree of sensitivity over the entire tail boom with an actuator embedded at the middle of the structure, while still using a minimal amount of sensors. Additionally, the extremely high sensitivity of the

NSSI metric allows for early detection of developing damage, and decreases the likelihood of "false positive" detections.

To investigate the potential for use of NWMS on a complex airframe structure, a modulated wave excitation was applied to the structure, and the damaged response was tracked via NSSI-MW. A typical response spectrum for a laterally mounted accelerometer is presented in Figure 5-3, comparing the driven and harmonic responses for both the healthy and damaged condition when driven with the F4/F7 shakers. It is important to note that for this research, the modulated wave excitation was provided using only out-of-plane direction shakers. However, the technique can be applied using two separate piezoelectric actuators as well, and would be similar to what would be implemented with onboard SHM system. Detection results for each SSI suite and individual sensors are presented in Figure 5-4 for all stations across the length of the structure.

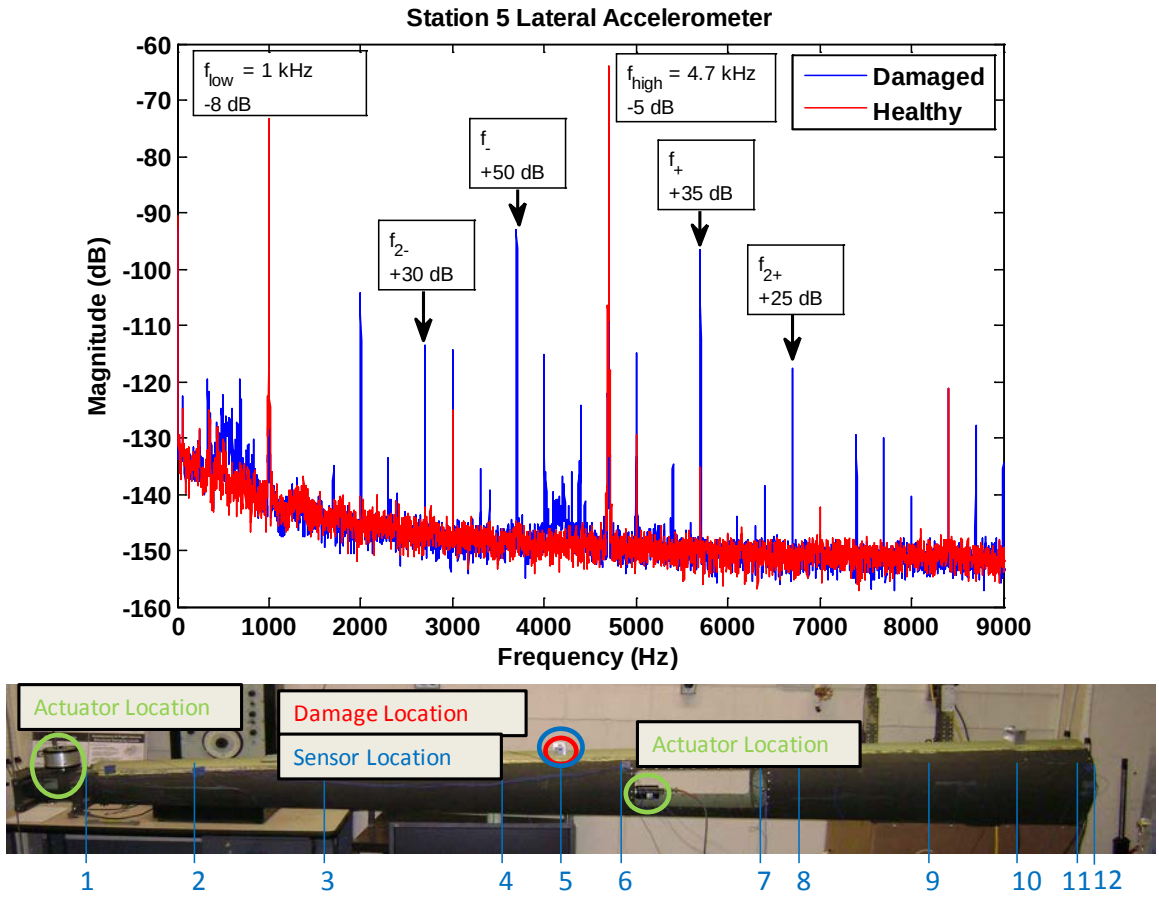

Figure 5-3: OH-58 tail boom strain sensor autospectra for f_{low} = 1 kHz / f_{high} = 4.7 kHz. Damage is introduced by loosening hanger bearing brackets. When damage is present in the system, a strong nonlinear response occurs, creating multiple wave interactions that can be seen in the response spectra.

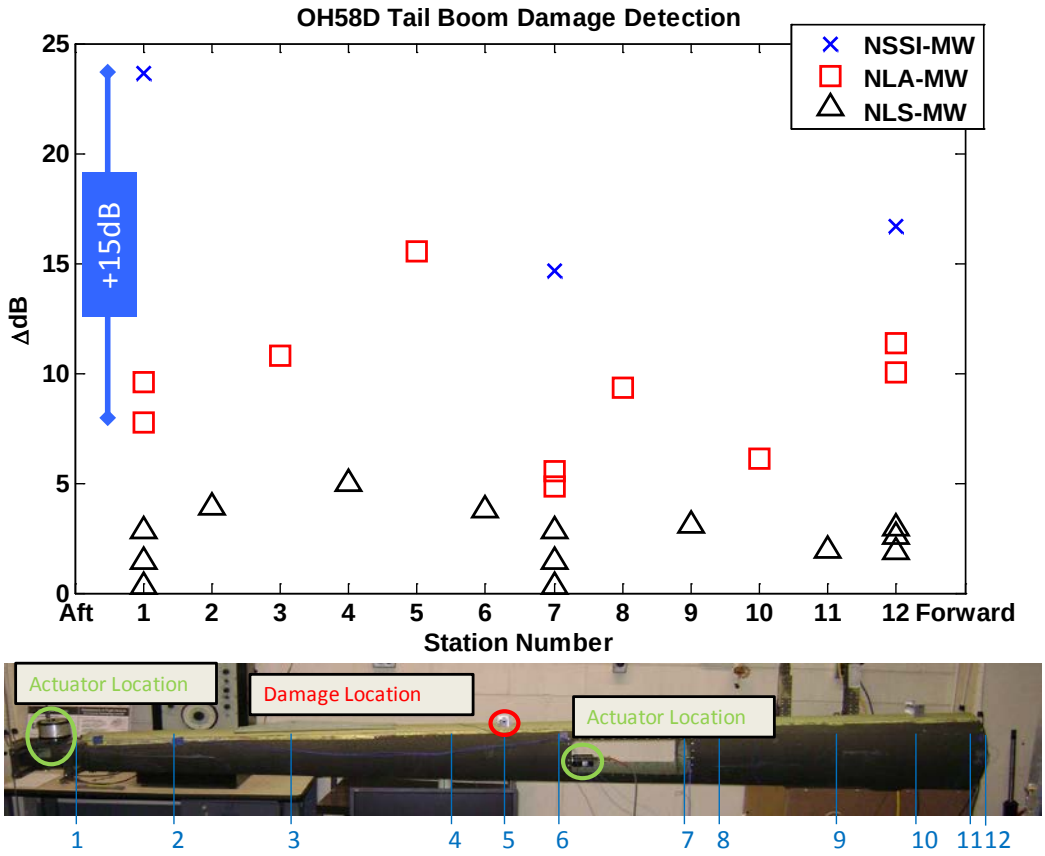

Figure 5-4: OH-58 tail boom NSSI-MW, NLS-MW, and NLA-MW results for f_{low} = 1 kHz / f_{high} = 4.7 kHz with the F4/F7 shakers. NSSI-MW has a much greater damage sensitivity via data fusion of the strains and accelerations vs. using strain or acceleration individually. Note damage is detected globally (all sensor locations).

Like previous driving conditions for modulated wave excitations on the aluminum and composite stiffened panels, both the frequencies (f_{low} = 1 kHz / f_{high} = 4.7 kHz) and amplitudes were chosen arbitrarily, and not optimized. The damage detection results for a modulated wave excitation presented in Figure 5-4 confirm that detection of a loose hanger bearing bracket is global throughout the length of the structure. Note that while the NLA-MW detection strength is highest at station 5, the accelerometer is located directly on the damaged bearing bracket. Additionally, NSSI-MW is somewhat lower at station 7 due to losses through the bulkhead of the structure. While NLA-MW is able to detect damage with a threshold above 5 dB, NLS-MW displays a relatively low detection results across the length of the entire structure. Overall, NSSI-

MW displays greater detection strength than the single sensor metrics with an increase of 15 dB over NLA-MW.

To quantitatively compare the detection strength of all detection metrics for both single tone and modulated wave interrogation, results from Figure 5-2 and Figure 5-4 can be shown together on a single scatter plot (Figure 5-5). Results prove that the all single tone metrics (NSSI/NLA/NLS) have higher relative detection strength than those utilizing combinational tones created by modulated wave excitation (NSSI-MW/NLA-MW/NLS-MW).

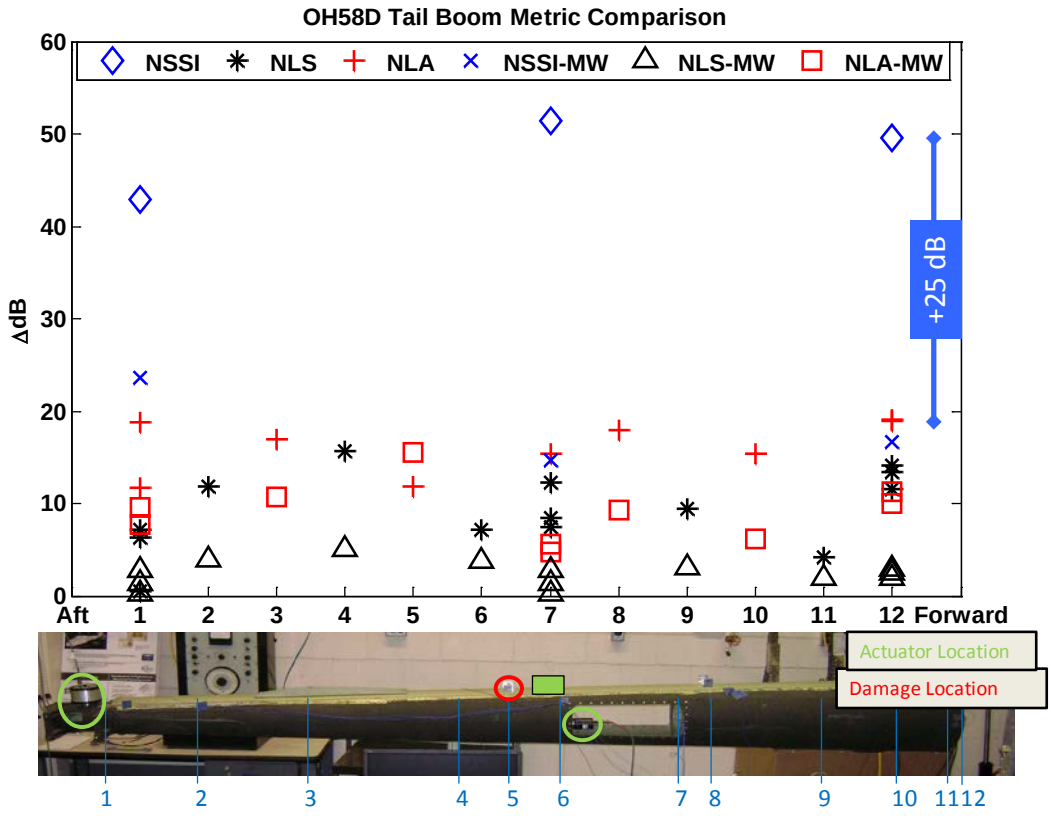

Figure 5-5: Detection strength for a modulated wave input (f_{low} = 1 kHz / f_{high} = 4.7 kHz with the F4/F7 shakers) and single tone harmonic excitation (f_{drive} = 8.5 kHz with the rectangular PZT). Results show that both SI-based metrics have a higher sensitivity than single-sensor metrics.

NSSI clearly exhibits the highest detection strength, and is ~25dB higher than the NSSI-MW at each station. However, driving conditions for single tone interrogation case required careful selection of force and frequency to activate a CAN sub-harmonic response. Driving

conditions for the modulated wave excitation were chosen arbitrarily, but still were able to detect the presence of a nonlinear damage feature to a high degree of sensitivity. This reinforces results presented in Chapters 3 and 4; while NSSI is an extremely high sensitivity metric, it requires careful selection of driving conditions to activate the characteristic nonlinear response which it depends on. Modulated wave excitation however, provides a more stable method of interrogation while still maintaining a high sensitivity to nonlinear damage features.

Chapter 6

Conclusions and Future Work

6.1 Summary and Key Results

This chapter presents a summary of the research and key experimental results presented in this thesis. The main focus of this research was to investigate contact acoustic nonlinearity characteristics in damaged structures, develop structural intensity-based damage detection approaches that key off CAN effects, and evaluate the performance of the techniques as they are applied to airframe structures with relevant damage types. To accomplish this, several experimental test beds were designed and instrumented. These ranged from simple stiffened aluminum panels to more complicated integrally stiffened composite panels. An OH-58D "Kiowa Warrior" tail boom was also used for development testing and experimentation evaluating "on-platform" sensor requirements and performance.

The SI-based damage detection techniques explored in this thesis included Nonlinear Structural Intensity (NSI), Nonlinear Structural Surface Intensity (NSSI), and NSSI-Modulated Wave (NSSI-MW). Additionally, several single-sensor damage detection metrics were developed, including Nonlinear Acceleration (NLA) and Nonlinear Strain (NLS). Each of these SI-based metrics was applied to all test beds in order to determine their effectiveness for evaluating nonlinear damage features in relevant types of airframe structures.

Using the stiffened aluminum plate, NSI visualization was used to illustrate how a CAN will manifest with damage. Results presented in Section 3.2 proved that NSI can be used to localize a nonlinear damage source at an ultra-subharmonic frequency in a baseline-free approach. This result proves the existence of the nonlinear source (created by redistribution of

energy from the driving signal) present when damage is introduced into a system. However, while NSI is a powerful visualization tool to understand how a CAN sub-harmonic response will manifest with damage, its use for practical airframe (structure) implementation is limited. The original formulation of SI is only valid for idealized isotropic structures, and NSI proved difficult to measure on more lightly damped structures ($\eta<.01$). Since very few practical rotorcraft structures conform to these assumptions, this led to the development of SI-based damage detection techniques using discrete sensor arrays.

To overcome the limitations of the original SI formulation, a different technique utilizing discrete sensor arrays, but still retaining a relation to the energy flow through the structure was used for damage detection. This technique, NSSI, was originally formulated in the time domain. However, results in Section 2.2 proved that NSSI as formulated in the frequency domain had a higher signal-to-noise ratio (60 dB lower noise floor), as well as a greater overall sensitivity to damage in the form of loose fasteners (11.6 dB increase). Additionally, the application of NSSI to the aluminum stiffened panel (presented in Section 3.3.1) had extremely high sensitivity to damage (43.1 dB detection strength), and maintained a monotonic relation to damage extent relatively independent from the damping condition present on the structure (Section 3.3.2). This result was promising, as more complex airframe structures can have varying levels of damping.

The presence of the CAN sub-harmonic response is not necessarily limited to damage features involving loose rivets. NSSI was also applied to integrally stiffened composite panels, with damage introduced as a delamination in the bond line at the stiffener termination. In Section 3.3.3, NSSI was able to detect this damage with an extremely high sensitivity (30 dB detection strength). This also reinforced the conclusion that NSSI is relatively independent of structural damping, as the composite stiffened panels had a much higher level of distributed damping than metallic structures. As composite materials are becoming more commonly used within the

aerospace community, these results show promise for SI-based damage detection metrics to be implemented within existing SHM programs for composite materials.

A major positive attribute of the single-tone interrogation method was that it could be implemented as a baseline-free approach. However, to activate the CAN sub-harmonic response, careful selection of the driving both force and frequency was needed. The dependence of the CAN sub-harmonic response on frequency and amplitude choice was presented in Section 3.4 for the aluminum stiffened panel. Results proved because the sub-harmonic response relies on the activation of an inherent instability (parametric resonance), small changes in driving force or frequency can cause the characteristic nonlinear response that NSSI relies on to be difficult to detect.

Because of this, a new formulation of intensity based damage detection (NSSI-MW) was developed utilizing two interrogation waves, and relied on detecting interactions (in the form of combinational frequencies) created as the waves excited a nonlinear damage feature. NSSI-MW proved to be a high sensitivity metric as well, displaying a detection strength of 27.2 dB on the aluminum stiffened panel. Driving conditions for the modulated wave interrogation were chosen arbitrarily and not optimized in any way. Detection results using NSSI-MW were able to detect damage on both the aluminum and composite stiffened panels to a high degree of sensitivity. The major advantage of the modulated wave interrogation approach was that it was much less selective with respect to driving conditions than using a single-tone harmonic excitation. The disadvantage of this technique however, was that it exhibited a lower sensitivity to damage (-15dB) than interrogation using a single-tone harmonic excitation as the active NSSI feature. Even with arbitrarily chosen driving conditions, NSSI-MW displayed a much more stable hysteresis response compared to NSSI, as seen in Section 4.2.2, which may be attractive for the technique to be implemented in an automated SHM system.

Further developing the intensity-based damage detection metrics gave positive results proving both NSSI and NSSI-MW can be applied to complex airframe structures. When applied to an OH-58 tail boom, each metric was able to detect damage in the form of a loose hanger bearing bracket to a high degree of sensitivity. Consistent with measurements taken on the stiffened panels, NSSI had higher detection strength than NSSI-MW (40 dB vs. 20 dB respectively), but the driving conditions required careful tuning to optimize the CAN sub-harmonic response. The data fusion of the intensity formulation provided a distinct advantage, as both NSSI and NSSI-MW exhibited a considerably higher sensitivity to damage (+30 dB and +15 dB respectively) than using single-sensor (strain or acceleration) nonlinear detection metrics.

6.2 Future Work

There is a need to continue to enhance damage detection techniques for all aerospace structures and relevant damage types. Results presented in Chapters 3-5 highlight the remarkable sensitivity to multiple damage types and increments shown by intensity-based SHM techniques. The surface intensity techniques were able to accurately characterize damage progression trends, and NSI was able to localize damage. To further advance intensity-based SHM techniques, particular sensor and actuator design requirements are needed to mature the technology for embedded airframe platform integration. Use of piezoelectric (PZT) actuators to actively interrogate structures showed promise when applied to an OH-58D tail boom. However, these actuators typically operate in the ultrasonic frequency range (greater than 20 kHz), much higher than the interrogation frequencies that are currently used for intensity-based measurements. To avoid operating below the resonant modes of the actuators, proper material choice and sizing is key when designing an actuator to work within an SHM system.

NSSI/NSSI-MW both proved to be robust health monitoring techniques able to detect a variety of different damage types. To further expand these techniques, future work will focus on detecting delaminations caused by impact damage (a common failure mode in composite airframes) in both stiffened and un-stiffened panels. Delaminations are a major issue for aging composite structures because they are difficult (if not impossible) to visually inspect, and can cause a drastic decrease in material strength which puts the airframe at risk for failure.

Throughout this thesis, it has been demonstrated that use of a single-tone interrogation requires careful calibration of driving force and frequency to activate a CAN sub-harmonic response. Because of this, implementing the single-tone approach may be difficult to apply to an on-aircraft SHM system. While modulated wave interrogation proved to be less sensitive to driving conditions, it displayed a lower sensitivity to damage, and could possibly benefit from optimizing driving conditions for the structure. Developing semi-automated interrogation frequency and drive force selection algorithms / procedures would enable SI-based damage detection technology to be more easily transitioned to real airframe systems. This would enable a true transition to a CBM approach, greatly increasing the time where aircraft are mission-capable, and significantly reducing the associated maintenance costs.

Appendix A

MATLAB Post-Processing Codes

To process raw data (velocities/accelerations/strains) into intensity components, several MATLAB codes were written applying the formulations for SI and SSI developed in Chapter 2. This appendix contains only the codes needed for a kernel. More detailed information can be found in Appendix B of Reference [18]. All scripts listed in this appendix were written using MATLAB 7.3.0 (R2007b).

A.1.1 Script to calculate SI components

This script takes the experimental cross-spectral data, and processes it into the needed intensity components for the SI visualization technique. Here, the variable Ixs denotes the shear component in the x-direction, Ixb denotes the bending component in the x-direction, Ixt denotes the twisting component in the x-direction, Iys denotes the shear component in the y-direction, Iyb denotes the bending component in the y-direction, Iyt denotes the twisting component in the y-direction for all regions.

```
% Region 1: Forward-Forward Differencing
for ii=region{1,1}
    Ixs(ii,1)=-(D/(excitationFreq^3*h))*imag((1+i*matLoss)*...
        ((-3*G(ii+4,ii)+14*G(ii+3,ii)-24*G(ii+2,ii)+18*G(ii+1,ii)-
5*G(ii,ii))/(2*deltaX^3)...
        +(-(-G(ii+3*y+2,ii)+4*G(ii+3*y+1,ii)-3*G(ii+3*y,ii))...
        +4*(-G(ii+2*y+2,ii)+4*G(ii+2*y+1,ii)-3*G(ii+2*y,ii))...
        -5*(-G(ii+1*y+2,ii)+4*G(ii+1*y+1,ii)-3*G(ii+1*y,ii))...
        +2*(-G(ii+2,ii)+4*G(ii+1,ii)-
3*G(ii,ii)))/(2*deltaX*deltaY^2)));
    Ixb(ii,1)=(D/(excitationFreq^3*h))*imag((1+i*matLoss)*...
        ((-(G(ii+3,ii+1)-G(ii+3,ii))+4*(G(ii+2,ii+1)-G(ii+2,ii))...
       -5*(G(ii+1,ii+1)-G(ii+1,ii))+2*(G(ii,ii+1)-
G(ii,ii)))/deltaX^3+...
```

```
       poisson*(-(G(ii+3*y,ii+1)-G(ii+3*y,ii))+4*(G(ii+2*y,ii+1)-
G(ii+2*y,ii))...
        -5*(G(ii+1*y,ii+1)-G(ii+1*y,ii))+2*(G(ii,ii+1)-
G(ii,ii)))/(deltaY^2*deltaX)));
    Ixt(ii,1)=(D*(1-
poisson)/(excitationFreq^3*h))*imag((1+i*matLoss)*...
        (G(ii+y+1,ii+y)-G(ii+y+1,ii)...
        -G(ii+y,ii+y)+G(ii+y,ii)...
        -G(ii+1,ii+y)+G(ii+1,ii)...
        +G(ii,ii+y)-G(ii,ii))/(deltaX*deltaY^2));

    Iys(ii,1)=-(D/(excitationFreq^3*h))*imag((1+i*matLoss)*...
        ((-3*G(ii+4*y,ii)+14*G(ii+3*y,ii)-
24*G(ii+2*y,ii)+18*G(ii+1*y,ii)-5*G(ii,ii))/(2*deltaY^3)...
        +(-(-G(ii+3+2*y,ii)+4*G(ii+3+1*y,ii)-3*G(ii+3,ii))...
        +4*(-G(ii+2+2*y,ii)+4*G(ii+2+1*y,ii)-3*G(ii+2,ii))...
        -5*(-G(ii+1+2*y,ii)+4*G(ii+1+1*y,ii)-3*G(ii+1,ii))...
        +2*(-G(ii+2*y,ii)+4*G(ii+1*y,ii)-
3*G(ii,ii)))/(2*deltaX^2*deltaY)));
    Iyb(ii,1)=(D/(excitationFreq^3*h))*imag((1+i*matLoss)*...
        ((-(G(ii+3*y,ii+1*y)-G(ii+3*y,ii))+4*(G(ii+2*y,ii+1*y)-
G(ii+2*y,ii))...
       -5*(G(ii+1*y,ii+1*y)-G(ii+1*y,ii))+2*(G(ii,ii+1*y)-
G(ii,ii)))/deltaY^3+...
       poisson*(-(G(ii+3,ii+1*y)-G(ii+3,ii))+4*(G(ii+2,ii+1*y)-
G(ii+2,ii))...
        -5*(G(ii+1,ii+1*y)-G(ii+1,ii))+2*(G(ii,ii+1*y)-
G(ii,ii)))/(deltaX^2*deltaY)));
    Iyt(ii,1)=(D*(1-
poisson)/(excitationFreq^3*h))*imag((1+i*matLoss)*...
        (G(ii+y+1,ii+1)-G(ii+y+1,ii)...
        -G(ii+1,ii+1)+G(ii+1,ii)...
        -G(ii+y,ii+1)+G(ii+y,ii)...
        +G(ii,ii+1)-G(ii,ii))/(deltaX^2*deltaY));
end

% Region 2: Central X - Forward Y Differencing
for ii=region{1,2}
    Ixs(ii,1)=-(D/(excitationFreq^3*h))*imag((1+i*matLoss)*...
        ((G(ii+2,ii)-2*G(ii+1,ii)+2*G(ii-1,ii)-G(ii-
2,ii))/(2*deltaX^3)...
        +(-(G(ii+3*y+1,ii)-G(ii+3*y-1,ii))...
        +4*(G(ii+2*y+1,ii)-G(ii+2*y-1,ii))...
        -5*(G(ii+1*y+1,ii)-G(ii+1*y-1,ii))...
        +2*(G(ii+1,ii)-G(ii-1,ii)))/(deltaY^2*2*deltaX)));
    Ixb(ii,1)=(D/(excitationFreq^3*h))*imag((1+i*matLoss)*...
        ((G(ii+1,ii+1)-G(ii+1,ii-1)-2*(G(ii,ii+1)-G(ii,ii-1))+G(ii-
1,ii+1)-G(ii-1,ii-1))/(2*deltaX^3)...
        +poisson*(-(G(ii+3*y,ii+1)-G(ii+3*y,ii-1))...
        +4*(G(ii+2*y,ii+1)-G(ii+2*y,ii-1))...
        -5*(G(ii+1*y,ii+1)-G(ii+1*y,ii-1))...
        +2*(G(ii,ii+1)-G(ii,ii-1)))/(2*deltaX*deltaY^2)));
    Ixt(ii,1)=(D*(1-
poisson)/(excitationFreq^3*h))*imag((1+i*matLoss)*...
```

```
        (G(ii+1+y,ii+y)-G(ii+1+y,ii)...
        -(G(ii-1+y,ii+y)-G(ii-1+y,ii))...
        -(G(ii+1,ii+y)-G(ii+1,ii))...
        +G(ii-1,ii+y)-G(ii-1,ii))/(2*deltaX*deltaY^2));

    Iys(ii,1)=-(D/(excitationFreq^3*h))*imag((1+i*matLoss)*...
        ((-3*G(ii+4*y,ii)+14*G(ii+3*y,ii)-
24*G(ii+2*y,ii)+18*G(ii+1*y,ii)-5*G(ii,ii))/(2*deltaY^3)...
        +(-G(ii+2*y+1,ii)+4*G(ii+1*y+1,ii)-3*G(ii+1,ii)...
        -2*(-G(ii+2*y,ii)+4*G(ii+1*y,ii)-3*G(ii,ii))...
        +(-G(ii+2*y-1,ii)+4*G(ii+1*y-1,ii)-3*G(ii-
1,ii)))/(deltaX^2*2*deltaY)));
    Iyb(ii,1)=(D/(excitationFreq^3*h))*imag((1+i*matLoss)*...
        ((-(G(ii+3*y,ii+y)-G(ii+3*y,ii))+4*(G(ii+2*y,ii+y)-
G(ii+2*y,ii))...
        -5*(G(ii+y,ii+y)-G(ii+y,ii))+2*(G(ii,ii+y)-
G(ii,ii)))/(deltaY^3)+...
        poisson*((G(ii+1,ii+y)-G(ii+1,ii))-2*(G(ii,ii+y)-G(ii,ii))...
        +(G(ii-1,ii+y)-G(ii-1,ii)))/(deltaX^2*deltaY)));
    Iyt(ii,1)=(D*(1-
poisson)/(excitationFreq^3*h))*imag((1+i*matLoss)*...
        (((G(ii+1+y,ii+1)-G(ii+1+y,ii-1))-(G(ii+1,ii+1)-G(ii+1,ii-
1))...
        -(G(ii-1+y,ii+1)-G(ii-1+y,ii-1))+G(ii-1,ii+1)-G(ii-1,ii-
1))/(4*deltaX^2*deltaY)));
end

% Region 3: Backward X - Backward Y Differencing
for ii=region{1,3}
    Ixs(ii,1)=-(D/(excitationFreq^3*h))*imag((1+i*matLoss)*...
        ((3*G(ii-4,ii)-14*G(ii-3,ii)+24*G(ii-2,ii)-18*G(ii-
1,ii)+5*G(ii,ii))/(2*deltaX^3)...
        +(-(G(ii+3*y-2,ii)-4*G(ii+3*y-1,ii)+3*G(ii+3*y,ii))...
        +4*(G(ii+2*y-2,ii)-4*G(ii+2*y-1,ii)+3*G(ii+2*y,ii))...
        -5*(G(ii+1*y-2,ii)-4*G(ii+1*y-1,ii)+3*G(ii+1*y,ii))...
        +2*(G(ii-2,ii)-4*G(ii-1,ii)+3*G(ii,ii)))/(2*deltaX*deltaY^2)));
    Ixb(ii,1)=(D/(excitationFreq^3*h))*imag((1+i*matLoss)*...
        ((-(-G(ii-3,ii-1)+G(ii-3,ii))+4*(-G(ii-2,ii-1)+G(ii-2,ii))...
       -5*(-G(ii-1,ii-1)+G(ii-1,ii))+2*(-G(ii,ii-
1)+G(ii,ii)))/deltaX^3+...
       poisson*(-(-G(ii+3*y,ii-1)+G(ii+3*y,ii))+4*(-G(ii+2*y,ii-
1)+G(ii+2*y,ii))...
        -5*(-G(ii+1*y,ii-1)+G(ii+1*y,ii))+2*(-G(ii,ii-
1)+G(ii,ii)))/(deltaY^2*deltaX)));
    Ixt(ii,1)=(D*(1-
poisson)/(excitationFreq^3*h))*imag((1+i*matLoss)*...
        (-G(ii+y-1,ii+y)+G(ii+y-1,ii)...
        +G(ii+y,ii+y)-G(ii+y,ii)...
        +G(ii-1,ii+y)-G(ii-1,ii)...
        -G(ii,ii+y)+G(ii,ii))/(deltaX*deltaY^2));

    Iys(ii,1)=-(D/(excitationFreq^3*h))*imag((1+i*matLoss)*...
        ((-3*G(ii+4*y,ii)+14*G(ii+3*y,ii)-
24*G(ii+2*y,ii)+18*G(ii+1*y,ii)-5*G(ii,ii))/(2*deltaY^3)...
```

```
        +(-(-G(ii-3+2*y,ii)+4*G(ii-3+1*y,ii)-3*G(ii-3,ii))...
        +4*(-G(ii-2+2*y,ii)+4*G(ii-2+1*y,ii)-3*G(ii-2,ii))...
        -5*(-G(ii-1+2*y,ii)+4*G(ii-1+1*y,ii)-3*G(ii-1,ii))...
        +2*(-G(ii+2*y,ii)+4*G(ii+1*y,ii)-
3*G(ii,ii)))/(2*deltaX^2*deltaY)));
    Iyb(ii,1)=(D/(excitationFreq^3*h))*imag((1+i*matLoss)*...
        ((-(G(ii+3*y,ii+y)-G(ii+3*y,ii))+4*(G(ii+2*y,ii+y)-
G(ii+2*y,ii))...
        -5*(G(ii+1*y,ii+y)-G(ii+1*y,ii))+2*(G(ii,ii+y)-
G(ii,ii)))/(deltaY^3)...
        +poisson*(-(G(ii-3,ii+y)-G(ii-3,ii))+4*(G(ii-2,ii+y)-G(ii-
2,ii))...
        -5*(G(ii-1,ii+y)-G(ii-1,ii))+2*(G(ii,ii+y)-
G(ii,ii)))/(deltaX^2*deltaY)));
    Iyt(ii,1)=(D*(1-
poisson)/(excitationFreq^3*h))*imag((1+i*matLoss)*...
        ((-(-G(ii-1+y,ii-1)+G(ii-1+y,ii))...
        +(-G(ii-1,ii-1)+G(ii-1,ii))...
        +(-G(ii+y,ii-1)+G(ii+y,ii))...
        -(-G(ii,ii-1)+G(ii,ii)))/(deltaX^2*deltaY)));
end

% Region 4: Forward X - Central Y Differencing
for ii=region{1,4}
    Ixs(ii,1)=-(D/(excitationFreq^3*h))*imag((1+i*matLoss)*...
        ((-3*G(ii+4,ii)+14*G(ii+3,ii)-24*G(ii+2,ii)+18*G(ii+1,ii)-
5*G(ii,ii))/(2*deltaX^3)+...
        ((-1)*(G(ii+2+y,ii)-2*G(ii+2,ii)+G(ii+2-y,ii))...
        +4*(G(ii+1+y,ii)-2*G(ii+1,ii)+G(ii+1-y,ii))...
        -3*(G(ii+y,ii)-2*G(ii,ii)+G(ii-y,ii)))/(2*deltaX*deltaY^2)));
    Ixb(ii,1)=(D/(excitationFreq^3*h))*imag((1+i*matLoss)*...
        (((-1)*(G(ii+3,ii+1)-G(ii+3,ii))+4*(G(ii+2,ii+1)-G(ii+2,ii))...
        -5*(G(ii+1,ii+1)-G(ii+1,ii))+2*(G(ii,ii+1)-
G(ii,ii)))/(deltaX^3)+...
        poisson*(G(ii+y,ii+1)-G(ii+y,ii)-2*(G(ii,ii+1)-G(ii,ii))...
        +G(ii-y,ii+1)-G(ii-y,ii))/(deltaX*deltaY^2)));
    Ixt(ii,1)=(D*(1-
poisson)/(excitationFreq^3*h))*imag((1+i*matLoss)*...
        ((G(ii+1+y,ii+y)-G(ii+1+y,ii-y))...
        -(G(ii+1-y,ii+y)-G(ii+1-y,ii-y))...
        -(G(ii+y,ii+y)-G(ii+y,ii-y))...
        +(G(ii-y,ii+y)-G(ii-y,ii-y)))/(4*deltaX*deltaY^2));

    Iys(ii,1)=-(D/(excitationFreq^3*h))*imag((1+i*matLoss)*...
        ((G(ii+2*y,ii)-2*G(ii+y,ii)+2*G(ii-y,ii)-G(ii-
2*y,ii))/(2*deltaY^3)+...
        (-(G(ii+3+y,ii)-G(ii+3-y,ii))+4*(G(ii+2+y,ii)-G(ii+2-y,ii))...
        -5*(G(ii+1+y,ii)-G(ii+1-y,ii))+2*(G(ii+y,ii)-G(ii-
y,ii)))/(2*deltaY*deltaX^2)));
    Iyb(ii,1)=(D/(excitationFreq^3*h))*imag((1+i*matLoss)*...
        ((G(ii+y,ii+y)-G(ii+y,ii-y)-2*(G(ii,ii+y)-G(ii,ii-y))...
        +G(ii-y,ii+y)-G(ii-y,ii-y))/(2*deltaY^3)+...
        poisson*(-(G(ii+3,ii+y)-G(ii+3,ii-y))+4*(G(ii+2,ii+y)-
G(ii+2,ii-y))...
```

```
        -5*(G(ii+1,ii+y)-G(ii+1,ii-y))+2*(G(ii,ii+y)-G(ii,ii-
y)))/(deltaX^2*2*deltaY)));
    Iyt(ii,1)=(D*(1-
poisson)/(excitationFreq^3*h))*imag((1+i*matLoss)*...
        ((G(ii+1+y,ii+1)-G(ii+1+y,ii))-(G(ii+y,ii+1)-G(ii+y,ii))...
        -(G(ii+1-y,ii+1)-G(ii+1-y,ii))+G(ii-y,ii+1)-G(ii-
y,ii))/(2*deltaY*deltaX^2));
end

% Region 5: Central X - Central Y Differencing
for ii=region{1,5}
    % calculate shear intensity magnitude in x dir sign has been
changed
    Ixs(ii,1)=-(D/(2*excitationFreq^3*h*deltaX))*imag((1+i*matLoss)*...
        ((G(ii+2,ii)-2*G(ii+1,ii)+2*G(ii-1,ii)-G(ii-
2,ii))/(deltaX^2)+...
        (G(ii+y+1,ii)-G(ii+y-1,ii)-2*G(ii+1,ii)+2*G(ii-1,ii)+G(ii-
y+1,ii)-G(ii-y-1,ii))/(deltaY^2)));
    % calculate bending intensity magnitude in x dir sign has been
changed
    Ixb(ii,1)=(D/(2*excitationFreq^3*h*deltaX))*imag((1+i*matLoss)*...
        ((G(ii+1,ii+1)-2*G(ii,ii+1)+G(ii-1,ii+1)-G(ii+1,ii-
1)+2*G(ii,ii-1)-G(ii-1,ii-1))/(deltaX^2)+...
        (G(ii+y,ii+1)-2*G(ii,ii+1)+G(ii-y,ii+1)-G(ii+y,ii-1)+2*G(ii,ii-
1)-G(ii-y,ii-1))*(poisson/deltaY^2)));
    % calculate twisting intensity magnitude in x dir sign has been
changed
    Ixt(ii,1)=-((D*(1-
poisson))/(8*excitationFreq^3*h*deltaX*deltaY^2))*imag((1+i*matLoss)*..
.
        (G(ii+y,ii-y-1)+G(ii+y,ii+y+1)-G(ii+y,ii-y+1)-G(ii+y,ii+y-1)...
        -G(ii-y,ii-y-1)-G(ii-y,ii+y+1)+G(ii-y,ii-y+1)+G(ii-y,ii+y-1)));

    % calculate shear intensity magnitude in y dir
    Iys(ii,1)=-(D/(2*excitationFreq^3*h*deltaY))*imag((1+i*matLoss)*...
        ((G(ii+(2*y),ii)-2*G(ii+y,ii)+2*G(ii-y,ii)-G(ii-
(2*y),ii))/(deltaY^2)+...
        (G(ii+y+1,ii)-G(ii-y+1,ii)-2*G(ii+y,ii)+2*G(ii-y,ii)+G(ii+y-
1,ii)-G(ii-y-1,ii))/deltaX^2));
    % calculate bending intensity magnitude in y dir
    Iyb(ii,1)=(D/(2*excitationFreq^3*h*deltaY))*imag((1+i*matLoss)*...
        ((G(ii+y,ii+y)-2*G(ii,ii+y)+G(ii-y,ii+y)-G(ii+y,ii-
y)+2*G(ii,ii-y)-G(ii-y,ii-y))/deltaY^2+...
        (G(ii+1,ii+y)-2*G(ii,ii+y)+G(ii-1,ii+y)-G(ii+1,ii-y)+2*G(ii,ii-
y)-G(ii-1,ii-y))*(poisson/deltaX^2)));
    % calculate twisting intensity magnitude in y dir
    Iyt(ii,1)=-((D*(1-
poisson))/(8*excitationFreq^3*h*deltaX^2*deltaY))*imag((1+i*matLoss)*..
.
        (G(ii+1,ii-y-1)+G(ii+1,ii+y+1)-G(ii+1,ii-y+1)-G(ii+1,ii+y-1)...
        -G(ii-1,ii-y-1)-G(ii-1,ii+y+1)+G(ii-1,ii-y+1)+G(ii-1,ii+y-1)));
end

% Region 6: Backward X - Central Y Differencing
```

```
for ii=region{1,6}
    Ixs(ii,1)=-(D/(excitationFreq^3*h))*imag((1+i*matLoss)*...
        ((3*G(ii-4,ii)-14*G(ii-3,ii)+24*G(ii-2,ii)-18*G(ii-
1,ii)+5*G(ii,ii))/(2*deltaX^3)+...
        ((1)*(G(ii-2+y,ii)-2*G(ii-2,ii)+G(ii-2-y,ii))...
        -4*(G(ii-1+y,ii)-2*G(ii-1,ii)+G(ii-1-y,ii))...
        +3*(G(ii+y,ii)-2*G(ii,ii)+G(ii-y,ii)))/(2*deltaX*deltaY^2)));
    Ixb(ii,1)=(D/(excitationFreq^3*h))*imag((1+i*matLoss)*...
        (((1)*(G(ii-3,ii-1)-G(ii-3,ii))-4*(G(ii-2,ii-1)-G(ii-2,ii))...
        +5*(G(ii-1,ii-1)-G(ii-1,ii))-2*(G(ii,ii-1)-
G(ii,ii)))/(deltaX^3)+...
        poisson*(-G(ii+y,ii-1)+G(ii+y,ii)+2*(G(ii,ii-1)-G(ii,ii))...
        -G(ii-y,ii-1)+G(ii-y,ii))/(deltaX*deltaY^2)));
    Ixt(ii,1)=(D*(1-
poisson)/(excitationFreq^3*h))*imag((1+i*matLoss)*...
        (-(G(ii-1+y,ii+y)-G(ii-1+y,ii-y))...
        +(G(ii-1-y,ii+y)-G(ii-1-y,ii-y))...
        +(G(ii+y,ii+y)-G(ii+y,ii-y))...
        -(G(ii-y,ii+y)-G(ii-y,ii-y)))/(4*deltaX*deltaY^2));

    Iys(ii,1)=-(D/(excitationFreq^3*h))*imag((1+i*matLoss)*...
        ((G(ii+2*y,ii)-2*G(ii+y,ii)+2*G(ii-y,ii)-G(ii-
2*y,ii))/(2*deltaY^3)+...
        (-(G(ii-3+y,ii)-G(ii-3-y,ii))+4*(G(ii-2+y,ii)-G(ii-2-y,ii))...
        -5*(G(ii-1+y,ii)-G(ii-1-y,ii))+2*(G(ii+y,ii)-G(ii-
y,ii)))/(2*deltaY*deltaX^2)));
    Iyb(ii,1)=(D/(excitationFreq^3*h))*imag((1+i*matLoss)*...
        ((G(ii+y,ii+y)-G(ii+y,ii-y)-2*(G(ii,ii+y)-G(ii,ii-y))...
        +G(ii-y,ii+y)-G(ii-y,ii-y))/(2*deltaY^3)+...
        poisson*(-(G(ii-3,ii+y)-G(ii-3,ii-y))+4*(G(ii-2,ii+y)-G(ii-
2,ii-y))...
        -5*(G(ii-1,ii+y)-G(ii-1,ii-y))+2*(G(ii,ii+y)-G(ii,ii-
y)))/(deltaX^2*2*deltaY)));
    Iyt(ii,1)=(D*(1-
poisson)/(excitationFreq^3*h))*imag((1+i*matLoss)*...
        ((G(ii-1+y,ii-1)-G(ii-1+y,ii))-(G(ii+y,ii-1)-G(ii+y,ii))...
        -(G(ii-1-y,ii-1)-G(ii-1-y,ii))+G(ii-y,ii-1)-G(ii-
y,ii))/(2*deltaY*deltaX^2));
end

% Region 7: Forward X - Backward Y Differencing
for ii=region{1,7}
    Ixs(ii,1)=-(D/(excitationFreq^3*h))*imag((1+i*matLoss)*...
        (-(3*G(ii+4,ii)-14*G(ii+3,ii)+24*G(ii+2,ii)-
18*G(ii+1,ii)+5*G(ii,ii))/(2*deltaX^3)...
        -(-(G(ii-3*y+2,ii)-4*G(ii-3*y+1,ii)+3*G(ii-3*y,ii))...
        +4*(G(ii-2*y+2,ii)-4*G(ii-2*y+1,ii)+3*G(ii-2*y,ii))...
        -5*(G(ii-1*y+2,ii)-4*G(ii-1*y+1,ii)+3*G(ii-1*y,ii))...
        +2*(G(ii+2,ii)-4*G(ii+1,ii)+3*G(ii,ii)))/(2*deltaX*deltaY^2)));
    Ixb(ii,1)=(D/(excitationFreq^3*h))*imag((1+i*matLoss)*...
        (((-G(ii+3,ii+1)+G(ii+3,ii))-4*(-G(ii+2,ii+1)+G(ii+2,ii))...
       +5*(-G(ii+1,ii+1)+G(ii+1,ii))-2*(-
G(ii,ii+1)+G(ii,ii)))/deltaX^3+...
```

```
       poisson*((-G(ii-3*y,ii+1)+G(ii-3*y,ii))-4*(-G(ii-2*y,ii+1)+G(ii-
2*y,ii))...
        +5*(-G(ii-1*y,ii+1)+G(ii-1*y,ii))-2*(-
G(ii,ii+1)+G(ii,ii)))/(deltaY^2*deltaX)));
    Ixt(ii,1)=(D*(1-
poisson)/(excitationFreq^3*h))*imag((1+i*matLoss)*...
        (G(ii-y+1,ii-y)-G(ii-y+1,ii)...
        -G(ii-y,ii-y)+G(ii-y,ii)...
        -G(ii+1,ii-y)+G(ii+1,ii)...
        +G(ii,ii-y)-G(ii,ii))/(deltaX*deltaY^2));

    Iys(ii,1)=-(D/(excitationFreq^3*h))*imag((1+i*matLoss)*...
        ((3*G(ii-4*y,ii)-14*G(ii-3*y,ii)+24*G(ii-2*y,ii)-18*G(ii-
1*y,ii)+5*G(ii,ii))/(2*deltaY^3)...
        +((-G(ii+3-2*y,ii)+4*G(ii+3-1*y,ii)-3*G(ii+3,ii))...
        -4*(-G(ii+2-2*y,ii)+4*G(ii+2-1*y,ii)-3*G(ii+2,ii))...
        +5*(-G(ii+1-2*y,ii)+4*G(ii+1-1*y,ii)-3*G(ii+1,ii))...
        -2*(-G(ii-2*y,ii)+4*G(ii-1*y,ii)-
3*G(ii,ii)))/(2*deltaX^2*deltaY)));
    Iyb(ii,1)=(D/(excitationFreq^3*h))*imag((1+i*matLoss)*...
        ((-(-G(ii-3*y,ii-y)+G(ii-3*y,ii))+4*(-G(ii-2*y,ii-y)+G(ii-
2*y,ii))...
        +5*(G(ii-1*y,ii-y)-G(ii-1*y,ii))-2*(G(ii,ii-y)-
G(ii,ii)))/(deltaY^3)...
        +poisson*((G(ii+3,ii-y)-G(ii+3,ii))-4*(G(ii+2,ii-y)-
G(ii+2,ii))...
        +5*(G(ii+1,ii-y)-G(ii+1,ii))-2*(G(ii,ii-y)-
G(ii,ii)))/(deltaX^2*deltaY)));
    Iyt(ii,1)=(D*(1-
poisson)/(excitationFreq^3*h))*imag((1+i*matLoss)*...
        (((-G(ii+1-y,ii+1)+G(ii+1-y,ii))...
        -(-G(ii+1,ii+1)+G(ii+1,ii))...
        -(-G(ii-y,ii+1)+G(ii-y,ii))...
        +(-G(ii,ii+1)+G(ii,ii)))/(deltaX^2*deltaY)));
end

% Region 8: Central X - Backward Y Differencing
for ii=region{1,8}
    Ixs(ii,1)=-(D/(excitationFreq^3*h))*imag((1+i*matLoss)*...
        ((G(ii+2,ii)-2*G(ii+1,ii)+2*G(ii-1,ii)-G(ii-
2,ii))/(2*deltaX^3)...
        +(-(G(ii-3*y+1,ii)-G(ii-3*y-1,ii))...
        +4*(G(ii-2*y+1,ii)-G(ii-2*y-1,ii))...
        -5*(G(ii-1*y+1,ii)-G(ii-1*y-1,ii))...
        +2*(G(ii+1,ii)-G(ii-1,ii)))/(deltaY^2*2*deltaX)));
    Ixb(ii,1)=(D/(excitationFreq^3*h))*imag((1+i*matLoss)*...
        ((G(ii+1,ii+1)-G(ii+1,ii-1)-2*(G(ii,ii+1)-G(ii,ii-1))+G(ii-
1,ii+1)-G(ii-1,ii-1))/(2*deltaX^3)...
        +poisson*(-(G(ii-3*y,ii+1)-G(ii-3*y,ii-1))...
        +4*(G(ii-2*y,ii+1)-G(ii-2*y,ii-1))...
        -5*(G(ii-1*y,ii+1)-G(ii-1*y,ii-1))...
        +2*(G(ii,ii+1)-G(ii,ii-1)))/(2*deltaX*deltaY^2)));
    Ixt(ii,1)=(D*(1-
poisson)/(excitationFreq^3*h))*imag((1+i*matLoss)*...
```

```
        (G(ii+1-y,ii-y)-G(ii+1-y,ii)...
        -(G(ii-1-y,ii-y)-G(ii-1-y,ii))...
        -(G(ii+1,ii-y)-G(ii+1,ii))...
        +G(ii-1,ii-y)-G(ii-1,ii))/(2*deltaX*deltaY^2));

    Iys(ii,1)=-(D/(excitationFreq^3*h))*imag((1+i*matLoss)*...
        (-(-3*G(ii-4*y,ii)+14*G(ii-3*y,ii)-24*G(ii-2*y,ii)+18*G(ii-
1*y,ii)-5*G(ii,ii))/(2*deltaY^3)...
        -(-G(ii-2*y+1,ii)+4*G(ii-1*y+1,ii)-3*G(ii+1,ii)...
        -2*(-G(ii-2*y,ii)+4*G(ii-1*y,ii)-3*G(ii,ii))...
        +(-G(ii-2*y-1,ii)+4*G(ii-1*y-1,ii)-3*G(ii-
1,ii)))/(deltaX^2*2*deltaY)));
    Iyb(ii,1)=-(D/(excitationFreq^3*h))*imag((1+i*matLoss)*...
        ((-(G(ii-3*y,ii-y)-G(ii-3*y,ii))+4*(G(ii-2*y,ii-y)-G(ii-
2*y,ii))...
        -5*(G(ii-y,ii-y)-G(ii-y,ii))+2*(G(ii,ii-y)-
G(ii,ii)))/(deltaY^3)+...
        poisson*((G(ii+1,ii-y)-G(ii+1,ii))-2*(G(ii,ii-y)-G(ii,ii))...
        +(G(ii-1,ii-y)-G(ii-1,ii)))/(deltaX^2*deltaY)));
    Iyt(ii,1)=-(D*(1-
poisson)/(excitationFreq^3*h))*imag((1+i*matLoss)*...
        (((G(ii+1-y,ii+1)-G(ii+1-y,ii-1))-(G(ii+1,ii+1)-G(ii+1,ii-
1))...
        -(G(ii-1-y,ii+1)-G(ii-1-y,ii-1))+G(ii-1,ii+1)-G(ii-1,ii-
1))/(4*deltaX^2*deltaY)));
end

% Region 9: Backward X - Backward Y Differencing
for ii=region{1,9}
    Ixs(ii,1)=(D/(excitationFreq^3*h))*imag((1+i*matLoss)*...
        ((-3*G(ii-4,ii)+14*G(ii-3,ii)-24*G(ii-2,ii)+18*G(ii-1,ii)-
5*G(ii,ii))/(2*deltaX^3)...
        +(-(-G(ii-3*y-2,ii)+4*G(ii-3*y-1,ii)-3*G(ii-3*y,ii))...
        +4*(-G(ii-2*y-2,ii)+4*G(ii-2*y-1,ii)-3*G(ii-2*y,ii))...
        -5*(-G(ii-1*y-2,ii)+4*G(ii-1*y-1,ii)-3*G(ii-1*y,ii))...
        +2*(-G(ii-2,ii)+4*G(ii-1,ii)-
3*G(ii,ii)))/(2*deltaX*deltaY^2)));
    Ixb(ii,1)=-(D/(excitationFreq^3*h))*imag((1+i*matLoss)*...
        ((-(G(ii-3,ii-1)-G(ii-3,ii))+4*(G(ii-2,ii-1)-G(ii-2,ii))...
       -5*(G(ii-1,ii-1)-G(ii-1,ii))+2*(G(ii,ii-1)-
G(ii,ii)))/deltaX^3+...
      poisson*(-(G(ii-3*y,ii-1)-G(ii-3*y,ii))+4*(G(ii-2*y,ii-1)-G(ii-
2*y,ii))...
        -5*(G(ii-1*y,ii-1)-G(ii-1*y,ii))+2*(G(ii,ii-1)-
G(ii,ii)))/(deltaY^2*deltaX)));
    Ixt(ii,1)=-(D*(1-
poisson)/(excitationFreq^3*h))*imag((1+i*matLoss)*...
        (G(ii-y-1,ii-y)-G(ii-y-1,ii)...
        -G(ii-y,ii-y)+G(ii-y,ii)...
        -G(ii-1,ii-y)+G(ii-1,ii)...
        +G(ii,ii-y)-G(ii,ii))/(deltaX*deltaY^2));

    Iys(ii,1)=(D/(excitationFreq^3*h))*imag((1+i*matLoss)*...
```

```
        ((-3*G(ii-4*y,ii)+14*G(ii-3*y,ii)-24*G(ii-2*y,ii)+18*G(ii-
1*y,ii)-5*G(ii,ii))/(2*deltaY^3)...
        +(-(-G(ii-3-2*y,ii)+4*G(ii-3-1*y,ii)-3*G(ii-3,ii))...
        +4*(-G(ii-2-2*y,ii)+4*G(ii-2-1*y,ii)-3*G(ii-2,ii))...
        -5*(-G(ii-1-2*y,ii)+4*G(ii-1-1*y,ii)-3*G(ii-1,ii))...
        +2*(-G(ii-2*y,ii)+4*G(ii-1*y,ii)-
3*G(ii,ii)))/(2*deltaX^2*deltaY)));
    Iyb(ii,1)=-(D/(excitationFreq^3*h))*imag((1+i*matLoss)*...
        ((-(G(ii-3*y,ii-1*y)-G(ii-3*y,ii))+4*(G(ii-2*y,ii-1*y)-G(ii-
2*y,ii))...
       -5*(G(ii-1*y,ii-1*y)-G(ii-1*y,ii))+2*(G(ii,ii-1*y)-
G(ii,ii)))/deltaY^3+...
      poisson*(-(G(ii-3,ii-1*y)-G(ii-3,ii))+4*(G(ii-2,ii-1*y)-G(ii-
2,ii))...
        -5*(G(ii-1,ii-1*y)-G(ii-1,ii))+2*(G(ii,ii-1*y)-
G(ii,ii)))/(deltaX^2*deltaY)));
    Iyt(ii,1)=-(D*(1-
poisson)/(excitationFreq^3*h))*imag((1+i*matLoss)*...
        (G(ii-y-1,ii-1)-G(ii-y-1,ii)...
        -G(ii-1,ii-1)+G(ii-1,ii)...
        -G(ii-y,ii-1)+G(ii-y,ii)...
        +G(ii,ii-1)-G(ii,ii))/(deltaX^2*deltaY));
end
```

A.1.2 SSI Calculation Script

This script takes the raw time acceleration and strain waveforms and uses them to calculate SSI components. This code was written as part of a larger MATLAB GUI written for the U.S. Army Research, Development and Engineering Command under Contract No. W911W6-08-C-0036, and can be seen in full in Appendix C of Reference [31].

```
function [Mag Ph Ix Iy Ixx Iyy]=ssi_m(data,fs,t_f,pplot,f1,f2,fc,E,v)
%ssi_m - compute structural surface intensity (SSI)
% function [Mag Ph Ix Iy Ixx Iyy]=ssi_m(data,fs,t_f,pplot,f1,f2,fc,E,v)
% Compute structural surface intensity using 2 accels and a rectangular
% rosette of strain gauges
% see G. Pavic, JSV 1987 for article with original SSI formulation
%
% 'data' is a matrix of calibrated time data stored in the following
format:
%   data(:,1)=Ax;     data(:,2)=Ay;     data(:,3)=Ex;     data(:,4)=Ey;
data(:,5)=E45;
% 'fs' is the sampling frequency
% 't_f' is 0 for time domain and 1 for frequency domain (default=1)
% 'pplot' displays a compass plot when equal to 1 (default=0)
% 'f1' and 'f2' are the integration range (default is 0 to Nyquist)
```

```
% 'fc' is the high pass filter cutoff frequency (default=25 Hz)
% 'Mag' and 'Ph' are the SSI magnitude and phase (degrees)
% 'Ix' and 'Iy' are the SSI x and y components
% 'Ixx' and 'Iyy' are the unintegrated SSI x and y components
% 'E' is Young's modulus and 'v' is Poisson's ratio
% NOTES:
% This function assumes the structural material is aluminum if no
material
% properties are given

% written by Micah Shepherd
% last modified December 2009
% see ssi_test1_m.m (?)
% could be updated for more versitle use
%   - user inputs averaging parameters (still hard coded)
%   - user inputs filter order (still hard coded)

% OTHER NOTES ON THIS IMPLEMENTATION OF SSI:
% 1) Original Pavic paper is missing the negative sign for the
frequency domain formulation
% 2) Factor of 2 is already taken into account when computing the
cross-spectra
% 3) Unintegrated quantities (Ixx & Iyy) represent the contribution to
the total
%    intensity from only that frequency portion of the time series

if nargin < 2
    data=[];
    fs=[];
elseif nargin==2
    t_f=1;
    pplot=0;
    fc=25;
elseif nargin==3
    pplot=0;
    fc=25;
elseif nargin==4
    f1=0;
    f2=fs/2;
    fc=25;
elseif nargin==6
    fc=25;
end

if isempty(data) || isempty(fs) || isempty(t_f) || isempty(pplot) ||
isempty(f1) || isempty(f2) || isempty(fc)
    errordlg('Invalid input arguments'); return;
end

if nargout==4 || (nargout==6 && t_f==0)
    Ixx=0;
    Iyy=0;
end
```

```
% define material properties
if nargin < 8
    E = 69e9;        % Al
    v = 0.33;
%     E = 200e9;       % Steel
%     v = 0.29;
    fprintf('assumed material is aluminum \n')
%     warndlg('assumed material is aluminum');
end
G=E/(2*(1+v));      % Shear Modulus

% define data
if length(data(1,:)') ~= 5
    error('Incorrect input matrix dimensions'); return;
end
Ax=data(:,1);
Ay=data(:,2);
Ex=data(:,3);
Ey=data(:,4);
E45=data(:,5);
Gxy=2*E45-Ex-Ey;

% NOTE: Segments must be time-aligned for correct averaging of time
% harmonic data.  This is most easily implemented by using L=N.
N=length(Ax);
fn=fs/2;
dt=1/fs;
L=N;
T=L*dt;
df=1/T;
f=0:df:fs-df;
t=dt:dt:T;
M=floor(N/L);
ax1=zeros(L,M);
ay1=ax1; ex1=ax1;
gxy1=ax1; ey1=ax1;
win=rectwin(L);
for m=1:M
    L1=L*(m-1)+1;
    L2=L*m;
    ax1(:,m)=Ax(L1:L2).*win;
    ay1(:,m)=Ay(L1:L2).*win;
    ex1(:,m)=Ex(L1:L2).*win;
    ey1(:,m)=Ey(L1:L2).*win;
    gxy1(:,m)=Gxy(L1:L2).*win;
end
win_cor=1;  % amplitude correction of window
% Hanning: sqrt(8/3) for stationary signals of nearly constant value
% Exact formulation should be used for non-stationary signals
ax1=mean(ax1,2)/win_cor;  % divide since applying in the time domain
ay1=mean(ay1,2)/win_cor;
ex1=mean(ex1,2)/win_cor;
ey1=mean(ey1,2)/win_cor;
gxy1=mean(gxy1,2)/win_cor;
```

```
% integrate acceleration (could have error when you don't start at
zero)
vx1 = cumtrapz(t,ax1);
vy1 = cumtrapz(t,ay1);

% apply Butterworth high-pass filter
% Model order and cut-off frequency will have some effects on the
beginning and
% ending samples of sinusoidal signals.  This effect can be minimized
by increasing
% either cutoff frequency or model order. This can also be eliminated
by throwing
% out the corrupted samples or not including them in the frequency
calculations.
if fc<=0 | fc>=fn
    warndlg('cut-off frequency must be greater than zero and less than
nyquist. f_c=50 was used instead.')
    fc=50;
end
filt_ord=5;
[B,A] = butter(filt_ord, fc/fn, 'high');
vx1 = filtfilt(B,A,vx1);
vy1 = filtfilt(B,A,vy1);
ex1 = filtfilt(B,A,ex1);
ey1 = filtfilt(B,A,ey1);
gxy1 = filtfilt(B,A,gxy1);

% % May need to check filter to ensure proper behavior
% figure;
% subplot(2,1,1); plot(vx1); hold on; plot(vy1,'r');
% subplot(2,1,2); plot(ex1); hold on; plot(ey1,'r');
% pause

% % make signals zero mean (not needed if high-pass filtering after
integration)
% vx1=vx1-mean(vx1);
% vy1=vy1-mean(vy1);
% ex1=ex1-mean(ex1);
% ey1=ey1-mean(ey1);
% gxy1=gxy1-mean(gxy1);

if t_f % frequency domain method

% % raw fft and PSD calculations
%     Vxf=fft(vx1)*dt;
%     Vyf=fft(vy1)*dt;
%     Exf=fft(ex1)*dt;
%     Eyf=fft(ey1)*dt;
%     Gxyf=fft(gxy1)*dt;
%
%     SExVx=Vxf.*conj(Exf)/T;
%     SEyVx=Vxf.*conj(Eyf)/T;
%     SxyVy=Vyf.*conj(Gxyf)/T;
```

```
%     SEyVy=Vyf.*conj(Eyf)/T;
%     SExVy=Vyf.*conj(Exf)/T;
%     SxyVx=Vxf.*conj(Gxyf)/T;

% % rms average, overlap and window to reduce noise in PSD estimate
%     N_e=2^12;
    N_e=2^15;
    [SExVx, f]=csd_ave_m(ex1,vx1,fs,0,'hann',N_e,50);
    [SEyVx, f]=csd_ave_m(ey1,vx1,fs,0,'hann',N_e,50);
    [SxyVy, f]=csd_ave_m(gxy1,vy1,fs,0,'hann',N_e,50);
    [SEyVy, f]=csd_ave_m(ey1,vy1,fs,0,'hann',N_e,50);
    [SExVy, f]=csd_ave_m(ex1,vy1,fs,0,'hann',N_e,50);
    [SxyVx, f]=csd_ave_m(gxy1,vx1,fs,0,'hann',N_e,50);
    N=N_e;

    GExVx=SExVx(1:N/2+1);
    GExVx(2:N/2)=2*SExVx(2:N/2);
    GEyVx=SEyVx(1:N/2+1);
    GEyVx(2:N/2)=2*SEyVx(2:N/2);
    GxyVy=SxyVy(1:N/2+1);
    GxyVy(2:N/2)=2*SxyVy(2:N/2);
    GEyVy=SEyVy(1:N/2+1);
    GEyVy(2:N/2)=2*SEyVy(2:N/2);
    GExVy=SExVy(1:N/2+1);
    GExVy(2:N/2)=2*SExVy(2:N/2);
    GxyVx=SxyVx(1:N/2+1);
    GxyVx(2:N/2)=2*SxyVx(2:N/2);

    if nargin==4
        f1=f(1);
        f2=fn;
    elseif f2<=f1 | f2>fn | f1<0
        h=warndlg('Check  frequency  integration  bounds.    Integration
performed over full range.', '');
        pause(2); close(h);
        f1=f(1);
        f2=fn;
    else
        f1b=find(f>=f1,1,'first');
        f2b=find(f<=f2,1,'last');
    end

    Ixx=zeros(2,length(f(f1b:f2b)));
    Ixx(1,:)=f(f1b:f2b);
    Iyy=Ixx;

    Ixx(2,:)=-G*(2/(1-
v)*(GExVx(f1b:f2b)+v*GEyVx(f1b:f2b))+GxyVy(f1b:f2b));
    Iyy(2,:)=-G*(2/(1-
v)*(GEyVy(f1b:f2b)+v*GExVy(f1b:f2b))+GxyVx(f1b:f2b));
    Ix=-G*real(trapz(f(f1b:f2b),2/(1-
v)*(GExVx(f1b:f2b)+v*GEyVx(f1b:f2b))+GxyVy(f1b:f2b)));
    Iy=-G*real(trapz(f(f1b:f2b),2/(1-
v)*(GEyVy(f1b:f2b)+v*GExVy(f1b:f2b))+GxyVx(f1b:f2b)));
```

```
% NOTES ON THIS IMPLEMENTATION OF SSI:
% 1) Original Pavic paper is missing the negative sign for the
frequency domain formulation
% 2) Factor of 2 is already taken into account when computing the
cross-spectra
% 3) Unintegrated quantities (Ixx & Iyy) represent the contribution to
the total
%    intensity from only that frequency portion of the signal
% 4) The time and frequency domain versions are equal due to Parsevals
%     theorem. However, when windowing and averaging, Parsevals theorem
no
%    longer holds and the quantities are only approximately equal.

    Mag=sqrt(abs(Ix)^2+abs(Iy)^2);
    Ph=atan2(Iy,Ix)*180/pi;

else % time domain method

    Ix=-G*(2/(1-v)*mean((ex1+v*ey1).*vx1)+mean(gxy1.*vy1));
    Iy=-G*(2/(1-v)*mean((ey1+v*ex1).*vy1)+mean(gxy1.*vx1));

    Mag=sqrt(abs(Ix)^2+abs(Iy)^2);
    Ph=atan2(Iy,Ix)*180/pi;

end

if pplot % create SSI figures
    figure
    compass(Ix+j*Iy)
    title('Surface Structural Intensity')

    if t_f
        figure

plot(Ixx(1,:),10*log10(abs(Ixx(2,:))),Iyy(1,:),10*log10(abs(Iyy(2,:))),
'r')
        title('Surface Structural Intensity')
        legend('x-dir','y-dir')
        xlabel('Frequency [Hz]')
        grid on
    end
end
```

A.1.3 Cross Spectral Density Calculation Script

```
function [Sxy, f]=csd_ave_m(data1,data2,fs,pplot,win_type,N_e,overlap)
%function psd_ave_m - compute cross spectral density
%                              function                              [Sxy,
f]=psd_ave_m(data1,data2,fs,pplot,win_type,N_e,overlap)
```

```
% Compute PSD using ensemble-averaged estimate with windowing and
% overlapping.    Data is the time waveform, fs is the sampling
frequency,
% pplot is whether to include a plot of the psd, win_type is the
windowing
% function (default is Hanning window, options are 'hann','rect' and
'hamm'),
% N_e is the ensemble length (default is 2^12), and overlap is the
percent
% overlap (default is 50%, 1 is no overlap).  Sxy is the complex, two-
sided Cross
% spectrum and 'f' is the appropriate frequency array. Input 0 to use
default values.
% See Bendat and Piersol p432-433

% written by Micah Shepherd
% last modified Mar 2009

% need to add error checks

error(nargchk(7,7,nargin));
error(nargoutchk(0,2,nargout));

if isempty(data1) || isempty(fs) || isempty(data1)
    return
end

if N_e == 0
    N_e=2^12;
    if length(data1)<N_e
        warndlg('ensemble length greater than number of data points')
        return
    end
end

if win_type==0 | win_type=='hann'
    wind=hanning(N_e);
elseif win_type=='rect'
    wind=rectwin(N_e);
end

if overlap==0
    overlap=50;
end

ave1=mean(data1);                   % Compute mean value and make data
zero-mean
data1=data1-ave1;
ave2=mean(data2);
data2=data2-ave2;
N=length(data1);                % total number of samples

fn=fs/2;                            % Nyquist Frequency
```

```
dt=1/fs;
T=dt*N_e;
df=1/T;
f=0:df:fs-df;                               % Frequency array

if overlap > 1
    overlap=overlap/100;          % Make percentage
    M=(1/overlap)*N./N_e-1;       % Num of ensembles w/ overlap
elseif overlap == 1
    M=(1/overlap)*N./N_e;         % Num of ensembles (no overlap)
else
    M=(1/overlap)*N./N_e-1;       % Num of ensembles w/ overlap
end
M=floor(M); % fprintf('%i averages\n',M);
var1=1;
var2=N_e;
x=zeros(N_e,M);
x_w=x; X=x;
for step=1:M
    x1(:,step)=data1(var1:var2);
    x_w1(:,step)=x1(:,step).*wind;          % Window the data
    X1(:,step)=fft(x_w1(:,step))*dt;           % N_e point DFT
    x2(:,step)=data2(var1:var2);
    x_w2(:,step)=x2(:,step).*wind;
    X2(:,step)=fft(x_w2(:,step))*dt;
    var1=var1+N_e.*overlap;                % Apply overlap
    var2=var2+N_e.*overlap;
end

X1=X1./sqrt(mean(wind.*conj(wind)));        % Adjust for window
X2=X2./sqrt(mean(wind.*conj(wind)));
Sxy=mean(X1.*conj(X2),2)./T;          % Compute the auto-spectral density
% Gxx=zeros(N_e/2,1);
% Gxx(1)=Sxx(1);
% Gxx(2:end)=2*Sxx(2:N_e/2);                % One-sided spectrum

if pplot
    figure
    plot(f,10.*log10(Sxy./2e-5^2))
    xlabel('Frequency [Hz]')
    ylabel('dB ref 20 \muPa')
end

if nargout == 0
    Sxy = 0;
end
```

Appendix B

Finite Differencing Equations for Plate Regions

In region 1, forward-forward differencing is used according the grid shown in Figure B-1, giving each SI component as Equations (B.1) – (B.6).

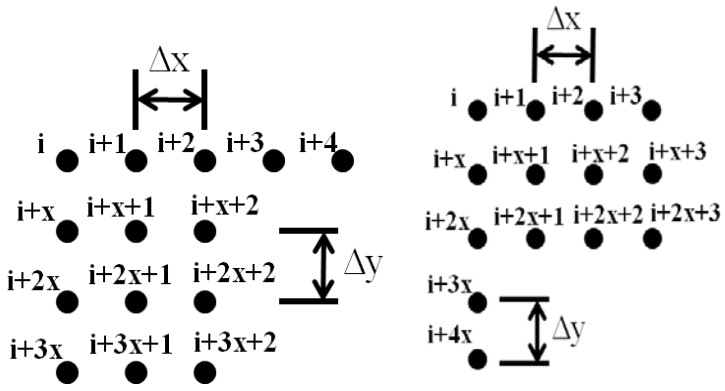

Figure B-1: Array used to calculate SI at any point within region 1 in the x- direction (left) and y - direction (right) on a plate. The SI vector at the center point (point #i) is calculated via finite differencing of the structural response matrix.

$$I_x^s = \frac{-D}{2\omega^3 h\Delta x} Im\left\{(1-i\eta)\left[\frac{-3G_{\ddot{w}_{i+4}\ddot{w}_i} + 14G_{\ddot{w}_{i+3}\ddot{w}_i} - 24G_{\ddot{w}_{i+2}\ddot{w}_i} + 18G_{\ddot{w}_{i+1}\ddot{w}_i} - 5G_{\ddot{w}_i\ddot{w}_i}}{\Delta x^2}\right.\right.$$

$$+ \frac{-(-G_{\ddot{w}_{i+3x+2}\ddot{w}_i} + 4G_{\ddot{w}_{i+3x+1}\ddot{w}_i} - 3G_{\ddot{w}_{i+3x}\ddot{w}_i}) + 4(-G_{\ddot{w}_{i+2x+2}\ddot{w}_i} + 4G_{\ddot{w}_{i+2x+1}\ddot{w}_i} - 3G_{\ddot{w}_{i+2x}\ddot{w}_i})}{\Delta y^2} \quad \text{(B.1)}$$

$$\left.\left. + \frac{-5(-G_{\ddot{w}_{i+x+2}\ddot{w}_i} + 4G_{\ddot{w}_{i+x+1}\ddot{w}_i} - 3G_{\ddot{w}_{i+x}\ddot{w}_i}) + 2(-G_{\ddot{w}_{i+2}\ddot{w}_i} + 4G_{\ddot{w}_{i+1}\ddot{w}_i} - 3G_{\ddot{w}_i\ddot{w}_i})}{\Delta y^2}\right]\right\}$$

$$I_x^b$$

$$= \frac{D}{\omega^3 h \Delta x} Im\left\{(1-i\eta)\left[\frac{-G_{\ddot{w}_{i+3}\ddot{w}_{i+1}} + G_{\ddot{w}_{i+3}\ddot{w}_i} + 4\left(G_{\ddot{w}_{i+2}\ddot{w}_{i+1}} - G_{\ddot{w}_{i+2}\ddot{w}_i}\right)}{\Delta x^2}\right.\right.$$

$$+ \frac{-5\left(G_{\ddot{w}_{i+1}\ddot{w}_{i+1}} - G_{\ddot{w}_{i+1}\ddot{w}_i}\right) + 2\left(G_{\ddot{w}_i\ddot{w}_{i+1}} - G_{\ddot{w}_i\ddot{w}_i}\right)}{\Delta x^2} \quad \text{(B.2)}$$

$$\left.\left. + \frac{1}{\upsilon}\frac{-G_{\ddot{w}_{i+3x}\ddot{w}_{i+1}} + G_{\ddot{w}_{i+3x}\ddot{w}_i} + 4\left(G_{\ddot{w}_{i+2x}\ddot{w}_{i+1}} - G_{\ddot{w}_{i+2x}\ddot{w}_i}\right) - 5\left(G_{\ddot{w}_{i+x}\ddot{w}_i} - G_{\ddot{w}_{i+x}\ddot{w}_i}\right) + 2\left(G_{\ddot{w}_i\ddot{w}_{i+1}} - G_{\ddot{w}_i\ddot{w}_i}\right)}{\Delta y^2}\right]\right\}$$

$$I_x^t = -\frac{D(1-v)}{\omega^3 h \Delta x \Delta y^2} Im\{(1+i\eta)[G_{\ddot{w}_{i+x+1}\ddot{w}_{i+x}} - G_{\ddot{w}_{i+x+1}\ddot{w}_i} - G_{\ddot{w}_{i+x}\ddot{w}_{i+x}} + G_{\ddot{w}_{i+x}\ddot{w}_i} - G_{\ddot{w}_{i+1}\ddot{w}_{i+x}} + G_{\ddot{w}_{i+1}\ddot{w}_i} + G_{\ddot{w}_i\ddot{w}_{i+x}} - G_{\ddot{w}_i\ddot{w}_i}]\} \quad \text{(B.3)}$$

$$I_y^s = \frac{-D}{2\omega^3 h \Delta y} Im\left\{(1-i\eta)\left[\frac{-3G_{\ddot{w}_{i+4x}\ddot{w}_i} + 14G_{\ddot{w}_{i+3x}\ddot{w}_i} - 24G_{\ddot{w}_{i+2x}\ddot{w}_i} + 18G_{\ddot{w}_{i+x}\ddot{w}_i} - 5G_{\ddot{w}_i\ddot{w}_i}}{\Delta y^2}\right.\right.$$

$$+ \frac{-(-G_{\ddot{w}_{i+2x+3}\ddot{w}_i} + 4G_{\ddot{w}_{i+x+3}\ddot{w}_i} - 3G_{\ddot{w}_{i+3}\ddot{w}_i}) + 4(-G_{\ddot{w}_{i+2x+2}\ddot{w}_i} + 4G_{\ddot{w}_{i+x+2}\ddot{w}_i} - 3G_{\ddot{w}_{i+2}\ddot{w}_i})}{\Delta x^2} \quad \text{(B.4)}$$

$$\left.\left. + \frac{-5(-G_{\ddot{w}_{i+2x+1}\ddot{w}_i} + 4G_{\ddot{w}_{i+x+1}\ddot{w}_i} - 3G_{\ddot{w}_{i+1}\ddot{w}_i}) + 2(-G_{\ddot{w}_{i+2x}\ddot{w}_i} + 4G_{\ddot{w}_{i+x}\ddot{w}_i} - 3G_{\ddot{w}_i\ddot{w}_i})}{\Delta x^2}\right]\right\}$$

$$I_y^b$$

$$= \frac{D}{\omega^3 h \Delta y} Im\left\{(1-i\eta)\left[\frac{-G_{\ddot{w}_{i+3x}\ddot{w}_{i+x}} + G_{\ddot{w}_{i+3x}\ddot{w}_i} + 4\left(G_{\ddot{w}_{i+2x}\ddot{w}_{i+x}} - G_{\ddot{w}_{i+2x}\ddot{w}_i}\right)}{\Delta y^2}\right.\right.$$

$$+ \frac{-5\left(G_{\ddot{w}_{i+x}\ddot{w}_{i+x}} - G_{\ddot{w}_{i+x}\ddot{w}_i}\right) + 2\left(G_{\ddot{w}_i\ddot{w}_{i+y}} - G_{\ddot{w}_i\ddot{w}_i}\right)}{\Delta y^2} \quad \text{(B.5)}$$

$$\left.\left. + \frac{1}{\upsilon}\frac{-G_{\ddot{w}_{i+3}\ddot{w}_{i+x}} + G_{\ddot{w}_{i+3}\ddot{w}_i} + 4\left(G_{\ddot{w}_{i+2}\ddot{w}_{i+x}} - G_{\ddot{w}_{i+2}\ddot{w}_i}\right) - 5\left(G_{\ddot{w}_{i+1}\ddot{w}_{i+x}} - G_{\ddot{w}_{i+1}\ddot{w}_i}\right) + 2\left(G_{\ddot{w}_i\ddot{w}_{i+x}} - G_{\ddot{w}_i\ddot{w}_i}\right)}{\Delta x^2}\right]\right\}$$

$$I_y^t = -\frac{D(1-v)}{\omega^3 h \Delta y \Delta x^2} Im\{(1+i\eta)[G_{\ddot{w}_{i+x+1}\ddot{w}_{i+1}} - G_{\ddot{w}_{i+x+1}\ddot{w}_i} - G_{\ddot{w}_{i+1}\ddot{w}_{i+1}} + G_{\ddot{w}_{i+1}\ddot{w}_i} - G_{\ddot{w}_{i+x}\ddot{w}_{i+1}} + G_{\ddot{w}_{i+x}\ddot{w}_i} + G_{\ddot{w}_i\ddot{w}_{i+1}} - G_{\ddot{w}_i\ddot{w}_i}]\} \quad \text{(B.6)}$$

In region 2, central-forward differencing is used according the grid shown in Figure B-2, giving each SI component as Equations (B.7) - (B.12).

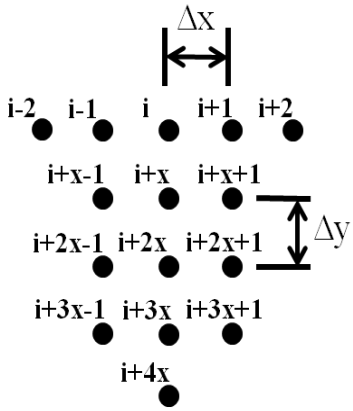

Figure B-2: Array used to calculate SI at any point within region 2 on a plate. The SI vector at the center point (point #i) is calculated via finite differencing of the structural response matrix.

$$I_x^s = \frac{-D}{2\omega^3 h\Delta x} Im\left\{(1-i\eta)\left[\frac{G_{\ddot{w}_{i+2}\ddot{w}_i} + 2G_{\ddot{w}_{i+1}\ddot{w}_i} - 2G_{\ddot{w}_{i-1}\ddot{w}_i} - G_{\ddot{w}_{i-2}\ddot{w}_i}}{\Delta x^2}\right.\right.$$
$$+ \frac{-(G_{\ddot{w}_{i+3x+1}\ddot{w}_i} - G_{\ddot{w}_{i+3x-1}\ddot{w}_i}) + 4(G_{\ddot{w}_{i+2x+1}\ddot{w}_i} - G_{\ddot{w}_{i+2x-1}\ddot{w}_i})}{\Delta y^2} \quad \text{(B.7)}$$
$$\left.\left. + \frac{-5(G_{\ddot{w}_{i+y+1}\ddot{w}_i} - G_{\ddot{w}_{i+y-1}\ddot{w}_i}) + 2(G_{\ddot{w}_{i+1}\ddot{w}_i} - G_{\ddot{w}_{i-1}\ddot{w}_i})}{\Delta y^2}\right]\right\}$$

$$I_x^b = \frac{D}{2\omega^3 h\Delta x} Im\left\{(1\right.$$
$$- i\eta)\left[\frac{G_{\ddot{w}_{i+1}\ddot{w}_{i+1}} - G_{\ddot{w}_{i+1}\ddot{w}_{i-1}} + 2\left(G_{\ddot{w}_i\ddot{w}_{i+1}} - G_{\ddot{w}_i\ddot{w}_{i-1}}\right) + G_{\ddot{w}_{i-1}\ddot{w}_{i+1}} - G_{\ddot{w}_{i-1}\ddot{w}_{i-1}}}{\Delta x^2}\right.$$
$$+ \frac{1}{v}\frac{-G_{\ddot{w}_{i+3x}\ddot{w}_{i+1}} + G_{\ddot{w}_{i+3x}\ddot{w}_{i-1}} + 4\left(G_{\ddot{w}_{i+2x}\ddot{w}_{i+1}} - G_{\ddot{w}_{i+2x}\ddot{w}_{i-1}}\right)}{\Delta y^2} \quad \text{(B.8)}$$
$$\left.\left. + \frac{1}{v}\frac{-5\left(G_{\ddot{w}_{i+x}\ddot{w}_{i+1}} - G_{\ddot{w}_{i+x}\ddot{w}_{i-1}}\right) + 2\left(G_{\ddot{w}_i\ddot{w}_{i+1}} - G_{\ddot{w}_i\ddot{w}_{i-1}}\right)}{\Delta y^2}\right]\right\}$$

$$I_x^t = \frac{D(1-v)}{2\omega^3 h\Delta x\Delta y^2} Im\{(1+i\eta)[G_{\ddot{w}_{i+x+1}\ddot{w}_{i+x}} - G_{\ddot{w}_{i+x+1}\ddot{w}_i} - G_{\ddot{w}_{i+x-1}\ddot{w}_{i+x}} + G_{\ddot{w}_{i+x-1}\ddot{w}_i} - G_{\ddot{w}_{i+1}\ddot{w}_{i+x}} \quad \text{(B.9)}$$
$$+ G_{\ddot{w}_{i+1}\ddot{w}_i} + G_{\ddot{w}_{i-1}\ddot{w}_{i+x}} - G_{\ddot{w}_{i-1}\ddot{w}_i}]\}$$

$$I_y^s$$

$$= \frac{-D}{2\omega^3 h\Delta y} Im\left\{(1-i\eta)\left[\frac{-3G_{\dot{w}_{i+4x}\dot{w}_i} + 14G_{\dot{w}_{i+3x}\dot{w}_i} - 24G_{\dot{w}_{i+2x}\dot{w}_i} + 18G_{\dot{w}_{i+x}\dot{w}_i} - 5G_{\dot{w}_i\dot{w}_i}}{\Delta y^2}\right.\right.$$

$$+ \frac{-(G_{\dot{w}_{i+2x+1}\dot{w}_i} - 4G_{\dot{w}_{i+x+1}\dot{w}_i} + 3G_{\dot{w}_{i+1}\dot{w}_i}) + 2(-G_{\dot{w}_{i+2x}\dot{w}_i} + 4G_{\dot{w}_{i+x}\dot{w}_i} - 3G_{\dot{w}_i\dot{w}_i})}{\Delta x^2} \quad \text{(B.10)}$$

$$\left.\left. + \frac{(-G_{\dot{w}_{i+2x-1}\dot{w}_i} + 4G_{\dot{w}_{i+x-1}\dot{w}_i} - 3G_{\dot{w}_{i-1}\dot{w}_i})}{\Delta x^2}\right]\right\}$$

$$I_y^b = \frac{D}{\omega^3 h\Delta y} Im\left\{(1-i\eta)\left[\frac{-G_{\dot{w}_{i+3x}\dot{w}_{i+x}} + G_{\dot{w}_{i+3x}\dot{w}_i} + 4\left(G_{\dot{w}_{i+2x}\dot{w}_{i+x}} - G_{\dot{w}_{i+2x}\dot{w}_i}\right)}{\Delta y^2}\right.\right.$$

$$+ \frac{-5\left(G_{\dot{w}_{i+x}\dot{w}_{i+x}} - G_{\dot{w}_{i+x}\dot{w}_i}\right) + 2\left(G_{\dot{w}_i\dot{w}_{i+x}} - G_{\dot{w}_i\dot{w}_i}\right)}{\Delta y^2} \quad \text{(B.11)}$$

$$\left.\left. + \frac{1}{v}\frac{G_{\dot{w}_{i+1}\dot{w}_{i+x}} - G_{\dot{w}_{i+1}\dot{w}_i} - 2\left(G_{\dot{w}_i\dot{w}_{i+x}} - G_{\dot{w}_i\dot{w}_i}\right) + \left(G_{\dot{w}_{i-1}\dot{w}_{i+x}} - G_{\dot{w}_{i-1}\dot{w}_i}\right)}{\Delta x^2}\right]\right\}$$

$$I_y^t = \frac{D(1-v)}{4\omega^3 h\Delta y\Delta x^2} Im\{(1+i\eta)[G_{\dot{w}_{i+x+1}\dot{w}_{i+1}} - G_{\dot{w}_{i+x+1}\dot{w}_{i-1}} - G_{\dot{w}_{i+1}\dot{w}_{i+1}} + G_{\dot{w}_{i+1}\dot{w}_{i-1}} - G_{\dot{w}_{i+x-1}\dot{w}_{i+1}} + G_{\dot{w}_{i+x-1}\dot{w}_{i-1}} + G_{\dot{w}_{i-1}\dot{w}_{i+1}} - G_{\dot{w}_{i-1}\dot{w}_{i-1}}]\} \quad \text{(B.12)}$$

In region 3, backward-backward differencing is used according the grid shown in Figure B-3, giving each SI component as Equations (B.13)-(B.18).

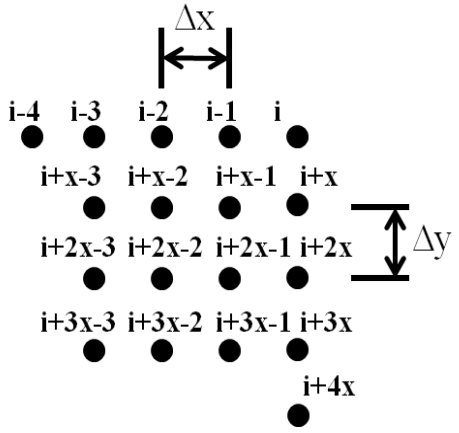

Figure B-3: Array used to calculate SI at any point within region 3 on a plate. The SI vector at the center point (point #i) is calculated via finite differencing of the structural response matrix.

$$I_x^s$$

$$= \frac{-D}{2\omega^3 h\Delta x} Im\left\{(1-i\eta)\left[\frac{-3G_{\ddot{w}_{i-4}\ddot{w}_i} + 14G_{\ddot{w}_{i-3}\ddot{w}_i} - 24G_{\ddot{w}_{i-2}\ddot{w}_i} + 18G_{\ddot{w}_{i-1}\ddot{w}_i} - 5G_{\ddot{w}_i\ddot{w}_i}}{\Delta x^2}\right.\right.$$

$$+ \frac{-(-G_{\ddot{w}_{i+3x-2}\ddot{w}_1} + 4G_{\ddot{w}_{i+3x-1}\ddot{w}_i} - 3G_{\ddot{w}_{i+3x}\ddot{w}_i}) + 4(G_{\ddot{w}_{i+2x-2}\ddot{w}_i} - 4G_{\ddot{w}_{i+2x-1}\ddot{w}_i} + 3G_{\ddot{w}_{i+2x}\ddot{w}_i})}{\Delta y^2} \quad \text{(B.13)}$$

$$\left.\left. + \frac{-5(G_{\ddot{w}_{i+x-2}\ddot{w}_i} - 4G_{\ddot{w}_{i+x-1}\ddot{w}_i} + 3G_{\ddot{w}_{i+x}\ddot{w}_i}) + 2(G_{\ddot{w}_{i-2}\ddot{w}_i} - 4G_{\ddot{w}_{i-1}\ddot{w}_i} + 3G_{\ddot{w}_i\ddot{w}_i})}{\Delta y^2}\right]\right\}$$

$$I_x^b = \frac{D}{\omega^3 h\Delta x} Im\left\{(1-i\eta)\left[\frac{-\left(-G_{\ddot{w}_{i-3}\ddot{w}_{i-1}} + G_{\ddot{w}_{i-3}\ddot{w}_i}\right) - 4\left(-G_{\ddot{w}_{i-2}\ddot{w}_{i-1}} + G_{\ddot{w}_{i-2}\ddot{w}_i}\right)}{\Delta x^2}\right.\right.$$

$$+ \frac{+5\left(-G_{\ddot{w}_{i-1}\ddot{w}_{i-1}} + G_{\ddot{w}_{i-1}\ddot{w}_i}\right) - 2\left(-G_{\ddot{w}_i\ddot{w}_{i-1}} + G_{\ddot{w}_i\ddot{w}_i}\right)}{\Delta x^2}$$

$$+ \frac{1}{\upsilon}\frac{-\left(-G_{\ddot{w}_{i+3x}\ddot{w}_{i-1}} + G_{\ddot{w}_{i+3x}\ddot{w}_i}\right) + 4\left(-G_{\ddot{w}_{i+2x}\ddot{w}_{i-1}} + G_{\ddot{w}_{i+2x}\ddot{w}_i}\right)}{\Delta y^2} \quad \text{(B.14)}$$

$$\left.\left. + \frac{1}{\upsilon}\frac{-5\left(-G_{\ddot{w}_{i+x}\ddot{w}_{i-1}} + G_{\ddot{w}_{i+x}\ddot{w}_i}\right) + 2\left(-G_{\ddot{w}_i\ddot{w}_{i-1}} + G_{\ddot{w}_i\ddot{w}_i}\right)}{\Delta y^2}\right]\right\}$$

$$I_x^t = -\frac{D(1-\upsilon)}{\omega^3 h\Delta x\Delta y^2} Im\{(1+i\eta)[-G_{\ddot{w}_{i+x-1}\ddot{w}_{i+x}} + G_{\ddot{w}_{i+x-1}\ddot{w}_i} + G_{\ddot{w}_{i+x}\ddot{w}_{i+x}} - G_{\ddot{w}_{i+x}\ddot{w}_i} + G_{\ddot{w}_{i-1}\ddot{w}_{i+x}} - G_{\ddot{w}_{i-1}\ddot{w}_i} - G_{\ddot{w}_i\ddot{w}_{i+x}} + G_{\ddot{w}_i\ddot{w}_i}]\} \quad \text{(B.15)}$$

$$I_y^s$$

$$= \frac{-D}{2\omega^3 h\Delta y} Im\left\{(1-i\eta)\left[\frac{-3G_{\ddot{w}_{i+4x}\ddot{w}_i} + 14G_{\ddot{w}_{i+3x}\ddot{w}_i} - 24G_{\ddot{w}_{i+2x}\ddot{w}_i} + 18G_{\ddot{w}_{i+x}\ddot{w}_i} - 5G_{\ddot{w}_i\ddot{w}_i}}{\Delta y^2}\right.\right.$$

$$+ \frac{-(-G_{\ddot{w}_{i+2x-3}\ddot{w}_i} + 4G_{\ddot{w}_{i+x-3}\ddot{w}_i} - 3G_{\ddot{w}_{i-3}\ddot{w}_i}) + 4(-G_{\ddot{w}_{i+2x-2}i} + 4G_{\ddot{w}_{i+x-2}\ddot{w}_i} - 3G_{\ddot{w}_{i-2}\ddot{w}_i})}{\Delta x^2} \quad \text{(B.16)}$$

$$\left.\left. + \frac{-5(-G_{\ddot{w}_{i+2x-1}\ddot{w}_i} + 4G_{\ddot{w}_{i+x-1}\ddot{w}_i} - 3G_{\ddot{w}_{i-1}\ddot{w}_i}) + 2(-G_{\ddot{w}_{i+2x}\ddot{w}_i} + 4G_{\ddot{w}_{i+x}\ddot{w}_i} - 3G_{\ddot{w}_i\ddot{w}_i})}{\Delta x^2}\right]\right\}$$

$$I_y^b = \frac{D}{\omega^3 h \Delta y} Im\left\{(1-i\eta)\left[\frac{-\left(G_{\ddot{w}_{i+3x}\ddot{w}_{i+x}} - G_{\ddot{w}_{i+3x}\ddot{w}_i}\right) + 4\left(G_{\ddot{w}_{i+2x}\ddot{w}_{i+x}} - G_{\ddot{w}_{i+2x}\ddot{w}_i}\right)}{\Delta y^2}\right.\right.$$
$$+ \frac{-5\left(G_{\ddot{w}_{i+x}\ddot{w}_{i+x}} - G_{\ddot{w}_{i+x}\ddot{w}_i}\right) + 2\left(G_{\ddot{w}_i\ddot{w}_{i+x}} - G_{\ddot{w}_i\ddot{w}_i}\right)}{\Delta y^2}$$
$$+ \frac{1}{\upsilon}\frac{-\left(G_{\ddot{w}_{i-3}\ddot{w}_{i+x}} - G_{\ddot{w}_{i-3}\ddot{w}_i}\right) + 4\left(G_{\ddot{w}_{i-2}\ddot{w}_{i+x}} - G_{\ddot{w}_{i-2}\ddot{w}_i}\right)}{\Delta x^2} \quad \text{(B.17)}$$
$$\left.\left. + \frac{1}{\upsilon}\frac{-5\left(G_{\ddot{w}_{i-1}\ddot{w}_{i+x}} - G_{\ddot{w}_{i-1}\ddot{w}_i}\right) + 2\left(G_{\ddot{w}_i\ddot{w}_{i+x}} - G_{\ddot{w}_i\ddot{w}_i}\right)}{\Delta x^2}\right]\right\}$$

$$I_y^t = -\frac{D(1-v)}{\omega^3 h \Delta y \Delta x^2} Im\{(1+i\eta)\left[G_{\ddot{w}_{i+x-1}\ddot{w}_{i-1}} - G_{\ddot{w}_{i+x-1}\ddot{w}_i} - G_{\ddot{w}_{i-1}\ddot{w}_{i-1}} + G_{\ddot{w}_{i-1}\ddot{w}_i} - G_{\ddot{w}_{i+x}\ddot{w}_{i-1}}\right.$$
$$\left. + G_{\ddot{w}_{i+x}\ddot{w}_i} + G_{\ddot{w}_i\ddot{w}_{i-1}} - G_{\ddot{w}_i\ddot{w}_i}\right]\} \quad \text{(B.18)}$$

In region 4, forward-central differencing is used according the grid shown in Figure B-4, giving each SI component as Equations (B.19) - (B.24).

Figure B-4: Array used to calculate SI at any point within region 4 on a plate. The SI vector at the center point (point #i) is calculated via finite differencing of the structural response matrix.

$$I_x^s = \frac{-D}{2\omega^3 h \Delta x} Im\left\{(1-i\eta)\left[\frac{-3G_{\ddot{w}_{i+4}\ddot{w}_i} + 14G_{\ddot{w}_{i+3}\ddot{w}_i} - 24G_{\ddot{w}_{i+2}\ddot{w}_i} + 18G_{\ddot{w}_{i+1}\ddot{w}_i} - 5G_{\ddot{w}_i\ddot{w}_i}}{\Delta x^2}\right.\right.$$
$$+ \frac{-(G_{\ddot{w}_{i+x+2}\ddot{w}_i} - 2G_{\ddot{w}_{i+2}\ddot{w}_i} + G_{\ddot{w}_{i-x+2}\ddot{w}_i}) + 4(G_{\ddot{w}_{i+y+1}\ddot{w}_i} - 2G_{\ddot{w}_{i+1}\ddot{w}_i} + G_{\ddot{w}_{i-x+1}\ddot{w}_i})}{\Delta y^2} \quad \text{(B.19)}$$
$$\left.\left. + \frac{-3(G_{\ddot{w}_{i+x}\ddot{w}_i} + 2G_{\ddot{w}_i\ddot{w}_i} - G_{\ddot{w}_{i-x}\ddot{w}_i})}{\Delta y^2}\right]\right\}$$

$$I_x^b = \frac{D}{\omega^3 h\Delta x} Im\left\{(1-i\eta)\left[\frac{-\left(G_{\ddot{w}_{i+3}\ddot{w}_{i+1}} - G_{\ddot{w}_{i+3}\ddot{w}_i}\right) + 4\left(G_{\ddot{w}_{i+2}\ddot{w}_{i+1}} - G_{\ddot{w}_{i+2}\ddot{w}_i}\right)}{\Delta x^2}\right.\right.$$
$$+ \frac{-5\left(G_{\ddot{w}_{i+1}\ddot{w}_{i+1}} - G_{\ddot{w}_{i+1}\ddot{w}_i}\right) + 2\left(G_{\ddot{w}_i\ddot{w}_{i+1}} - G_{\ddot{w}_i\ddot{w}_i}\right)}{\Delta x^2} \quad \text{(B.20)}$$
$$\left.\left. + \frac{1}{v}\frac{G_{\ddot{w}_{i+x}\ddot{w}_{i+1}} - G_{\ddot{w}_{i+x}\ddot{w}_i} - 2\left(G_{\ddot{w}_i\ddot{w}_{i+1}} - G_{\ddot{w}_i\ddot{w}_i}\right) + \left(G_{\ddot{w}_{i-x}\ddot{w}_{i+1}} - G_{\ddot{w}_{i-x}\ddot{w}_i}\right)}{\Delta y^2}\right]\right\}$$

$$I_x^t = \frac{D(1-v)}{4\omega^3 h\Delta x\Delta y^2} Im\{(1+i\eta)[G_{\ddot{w}_{i+x+1}\ddot{w}_{i+x}} - G_{\ddot{w}_{i+x+1}\ddot{w}_{i-x}} - G_{\ddot{w}_{i-x-1}\ddot{w}_{i+x}} - G_{\ddot{w}_{i-x-1}\ddot{w}_{i-x}}$$
$$- G_{\ddot{w}_{i+x}\ddot{w}_{i+x}} - G_{\ddot{w}_{i+x}\ddot{w}_{i-x}} + G_{\ddot{w}_{i-x}\ddot{w}_{i+x}} - G_{\ddot{w}_{i-x}\ddot{w}_{i-x}}]\} \quad \text{(B.20)}$$

$$I_y^s = \frac{-D}{2\omega^3 h\Delta y} Im\left\{(1-i\eta)\left[\frac{G_{\ddot{w}_{i+2x}\ddot{w}_i} - 2G_{\ddot{w}_{i+x}\ddot{w}_i} + 2G_{\ddot{w}_{i-x}\ddot{w}_i} - G_{\ddot{w}_{i-2x}\ddot{w}_i}}{\Delta y^2}\right.\right.$$
$$+ \frac{-(G_{\ddot{w}_{i+x+3}\ddot{w}_i} - G_{\ddot{w}_{i-x+3}\ddot{w}_i}) + 4(G_{\ddot{w}_{i+x+2}\ddot{w}_i} - G_{\ddot{w}_{i-x+2}\ddot{w}_i})}{\Delta x^2} \quad \text{(B.21)}$$
$$\left.\left. + \frac{-5(G_{\ddot{w}_{i+x+1}\ddot{w}_i} - G_{\ddot{w}_{i-x+1}\ddot{w}_i}) + 2(G_{\ddot{w}_{i+x}\ddot{w}_i} - G_{\ddot{w}_{i-x}\ddot{w}_i})}{\Delta x^2}\right]\right\}$$

$$I_y^b = \frac{D}{2\omega^3 h\Delta y} Im\left\{(1-i\eta)\left[\frac{G_{\ddot{w}_{i+x}\ddot{w}_{i+x}} - G_{\ddot{w}_{i+x}\ddot{w}_{i-x}} + 2\left(G_{\ddot{w}_i\ddot{w}_{i+x}} - G_{\ddot{w}_i\ddot{w}_{i-x}}\right)}{\Delta y^2}\right.\right.$$
$$+ \frac{G_{\ddot{w}_{i-x}\ddot{w}_{i+x}} - G_{\ddot{w}_{i-x}\ddot{w}_{i-x}}}{\Delta y^2}$$
$$+ \frac{1}{v}\frac{-\left(G_{\ddot{w}_{i+3}\ddot{w}_{i+x}} - G_{\ddot{w}_{i+3}\ddot{w}_{i-x}}\right) + 4\left(G_{\ddot{w}_{i+2}\ddot{w}_{i+x}} - G_{\ddot{w}_{i+2}\ddot{w}_{i-x}}\right)}{\Delta x^2} \quad \text{(B.22)}$$
$$\left.\left. + \frac{1}{v}\frac{-5\left(G_{\ddot{w}_{i+1}\ddot{w}_{i+x}} - G_{\ddot{w}_{i+1}\ddot{w}_{i-x}}\right) + 2\left(G_{\ddot{w}_i\ddot{w}_{i+x}} - G_{\ddot{w}_i\ddot{w}_{i-x}}\right)}{\Delta x^2}\right]\right\}$$

$$I_y^t = \frac{D(1-v)}{2\omega^3 h\Delta y\Delta x^2} Im\{(1+i\eta)[G_{\ddot{w}_{i+x+1}\ddot{w}_{i+1}} - G_{\ddot{w}_{i+x+1}\ddot{w}_i} - G_{\ddot{w}_{i+x}\ddot{w}_{i+1}} + G_{\ddot{w}_{i+x}\ddot{w}_i} - G_{\ddot{w}_{i-x+1}\ddot{w}_{i+1}}$$
$$+ G_{\ddot{w}_{i-x+1}\ddot{w}_i} + G_{\ddot{w}_{i-x}\ddot{w}_{i+1}} - G_{\ddot{w}_{i-x}\ddot{w}_i}]\} \quad \text{(B.23)}$$

In region 6, backward-central differencing is used according the grid shown in Figure B-5, giving each SI component as Equations (B.24) – (B.29).

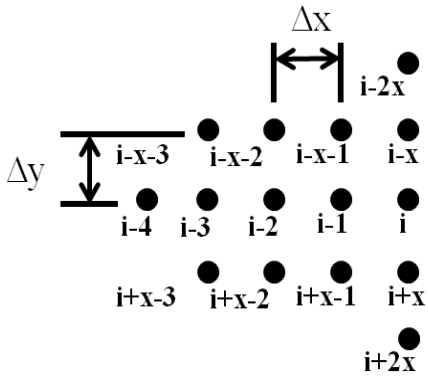

Figure B-5: Array used to calculate SI at any point within region 6 on a plate. The SI vector at the center point (point #i) is calculated via finite differencing of the structural response matrix.

$$I_x^s = \frac{-D}{2\omega^3 h\Delta x} Im\left\{(1-i\eta)\left[\frac{3G_{\ddot{w}_{i-4}\ddot{w}_i} - 14G_{\ddot{w}_{i-3}\ddot{w}_i} + 24G_{\ddot{w}_{i-2}\ddot{w}_i} - 18G_{\ddot{w}_{i-1}\ddot{w}_i} + 5G_{\ddot{w}_i\ddot{w}_i}}{\Delta x^2}\right.\right.$$
$$+ \frac{(G_{\ddot{w}_{i+x-2}\ddot{w}_i} - 2G_{\ddot{w}_{i-2}\ddot{w}_i} + G_{\ddot{w}_{i-x-2}\ddot{w}_i}) + 4(G_{\ddot{w}_{i+y-1}\ddot{w}_i} - 2G_{\ddot{w}_{i-1}\ddot{w}_i} + G_{\ddot{w}_{i-x-1}\ddot{w}_i})}{\Delta y^2} \quad \text{(B.24)}$$
$$\left.\left. + \frac{3(G_{\ddot{w}_{i+x}\ddot{w}_i} + 2G_{\ddot{w}_i\ddot{w}_i} - G_{\ddot{w}_{i-x}\ddot{w}_i})}{\Delta y^2}\right]\right\}$$

$$I_x^b = \frac{D}{\omega^3 h\Delta x} Im\left\{(1-i\eta)\left[\frac{\left(G_{\ddot{w}_{i-3}\ddot{w}_{i-1}} - G_{\ddot{w}_{i-3}\ddot{w}_i}\right) - 4\left(G_{\ddot{w}_{i-2}\ddot{w}_{i-1}} - G_{\ddot{w}_{i-2}\ddot{w}_i}\right)}{\Delta x^2}\right.\right.$$
$$+ \frac{5\left(G_{\ddot{w}_{i-1}\ddot{w}_{i-1}} - G_{\ddot{w}_{i-1}\ddot{w}_i}\right) - 2\left(G_{\ddot{w}_i\ddot{w}_{i-1}} - G_{\ddot{w}_i\ddot{w}_i}\right)}{\Delta x^2} \quad \text{(B.25)}$$
$$\left.\left. + \frac{1}{v}\frac{-\left(G_{\ddot{w}_{i+x}\ddot{w}_{i-1}} - G_{\ddot{w}_{i+x}\ddot{w}_i}\right) + 2\left(G_{\ddot{w}_i\ddot{w}_{i-1}} - G_{\ddot{w}_i\ddot{w}_i}\right) - \left(G_{\ddot{w}_{i-x}\ddot{w}_{i-1}} - G_{\ddot{w}_{i-x}\ddot{w}_i}\right)}{\Delta y^2}\right]\right\}$$

$$I_x^t = \frac{D(1-v)}{4\omega^3 h\Delta x\Delta y^2} Im\{(1+i\eta)[-G_{\ddot{w}_{i+x-1}\ddot{w}_{i+x}} + G_{\ddot{w}_{i+x-1}\ddot{w}_{i-x}} + G_{\ddot{w}_{i-x-1}\ddot{w}_{i+x}} - G_{\ddot{w}_{i-x-1}\ddot{w}_{i-x}}$$
$$- G_{\ddot{w}_{i+x}\ddot{w}_{i+x}} - G_{\ddot{w}_{i+x}\ddot{w}_{i-x}} - G_{\ddot{w}_{i-x}\ddot{w}_{i+x}} + G_{\ddot{w}_{i-x}\ddot{w}_{i-x}}]\} \quad \text{(B.26)}$$

$$I_y^s = \frac{-D}{2\omega^3 h\Delta y} Im\left\{(1-i\eta)\left[\frac{G_{\ddot{w}_{i+2x}\ddot{w}_i} - 2G_{\ddot{w}_{i+x}\ddot{w}_i} + 2G_{\ddot{w}_{i-x}\ddot{w}_i} - G_{\ddot{w}_{i-2x}\ddot{w}_i}}{\Delta y^2}\right.\right.$$
$$+ \frac{-(G_{\ddot{w}_{i+x-3}\ddot{w}_i} - G_{\ddot{w}_{i-x-3}\ddot{w}_i}) + 4(G_{\ddot{w}_{i+x-2}\ddot{w}_i} - G_{\ddot{w}_{i-x-2}\ddot{w}_i})}{\Delta x^2} \quad \text{(B.27)}$$
$$\left.\left. + \frac{-5(G_{\ddot{w}_{i+x-1}\ddot{w}_i} - G_{\ddot{w}_{i-x-1}\ddot{w}_i}) + 2(G_{\ddot{w}_{i+x}\ddot{w}_i} - G_{\ddot{w}_{i-x}\ddot{w}_i})}{\Delta x^2}\right]\right\}$$

$$I_y^b = \frac{D}{2\omega^3 h\Delta y} Im\left\{(1-i\eta)\left[\frac{G_{\ddot{w}_{i+x}\ddot{w}_{i+x}} - G_{\ddot{w}_{i+x}\ddot{w}_{i-x}} - 2\left(G_{\ddot{w}_i\ddot{w}_{i+x}} - G_{\ddot{w}_i\ddot{w}_{i-x}}\right)}{\Delta y^2}\right.\right.$$
$$+ \frac{G_{\ddot{w}_{i-x}\ddot{w}_{i+x}} - G_{\ddot{w}_{i-x}\ddot{w}_{i-x}}}{\Delta y^2}$$
$$+ \frac{1}{v}\frac{-\left(G_{\ddot{w}_{i-3}\ddot{w}_{i+x}} - G_{\ddot{w}_{i-3}\ddot{w}_{i-x}}\right) + 4\left(G_{\ddot{w}_{i-2}\ddot{w}_{i+x}} - G_{\ddot{w}_{i-2}\ddot{w}_{i-x}}\right)}{\Delta x^2} \quad \text{(B.28)}$$
$$\left.\left. + \frac{1}{v}\frac{-5\left(G_{\ddot{w}_{i-1}\ddot{w}_{i+x}} - G_{\ddot{w}_{i-1}\ddot{w}_{i-x}}\right) + 2\left(G_{\ddot{w}_i\ddot{w}_{i+x}} - G_{\ddot{w}_i\ddot{w}_{i-x}}\right)}{\Delta x^2}\right]\right\}$$

$$I_y^t = \frac{D(1-v)}{2\omega^3 h\Delta y\Delta x^2} Im\{(1+i\eta)[G_{\ddot{w}_{i+x-1}\ddot{w}_{i-1}} - G_{\ddot{w}_{i+x-1}\ddot{w}_i} - G_{\ddot{w}_{i+x}\ddot{w}_{i-1}} + G_{\ddot{w}_{i+x}\ddot{w}_i} - G_{\ddot{w}_{i-x-1}\ddot{w}_{i+1}} \quad \text{(B.29)}$$
$$+ G_{\ddot{w}_{i-x-1}\ddot{w}_i} + G_{\ddot{w}_{i-x}\ddot{w}_{i-1}} - G_{\ddot{w}_{i-x}\ddot{w}_i}]\}$$

In region 7, forward-backward differencing is used according the grid shown in Figure B-6, giving each SI component as Equations (B.30) – (B.35).

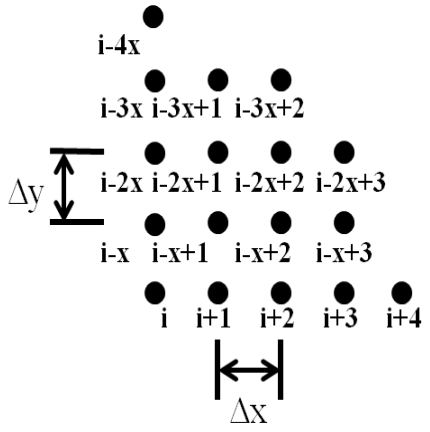

Figure B-6: Array used to calculate SI at any point within region 7 on a plate. The SI vector at the center point (point #i) is calculated via finite differencing of the structural response matrix.

$$I_x^s = \frac{-D}{2\omega^3 h\Delta x} Im\left\{(1-i\eta)\left[\frac{-3G_{\ddot{w}_{i+4}\ddot{w}_i} + 14G_{\ddot{w}_{i+3}\ddot{w}_i} - 24G_{\ddot{w}_{i+2}\ddot{w}_i} + 18G_{\ddot{w}_{i+1}\ddot{w}_i} - 5G_{\ddot{w}_i\ddot{w}_i}}{\Delta x^2}\right.\right.$$

$$+ \frac{(G_{\ddot{w}_{i-3x+2}\ddot{w}_i} - 4G_{\ddot{w}_{i-3x+1}\ddot{w}_i} + 3G_{\ddot{w}_{i-3x}\ddot{w}_i}) - 4(G_{\ddot{w}_{i-2x+2}\ddot{w}_i} - 4G_{\ddot{w}_{i-2x+1}\ddot{w}_i} + 3G_{\ddot{w}_{i-2x}\ddot{w}_i})}{\Delta y^2} \quad \text{(B.30)}$$

$$\left.\left. + \frac{5(G_{\ddot{w}_{i-x+2}\ddot{w}_i} - 4G_{\ddot{w}_{i-x+1}\ddot{w}_i} + 3G_{\ddot{w}_{i-x}\ddot{w}_i}) - 2(G_{\ddot{w}_{i+2}\ddot{w}_i} - 4G_{\ddot{w}_{i+1}\ddot{w}_i} + 3G_{\ddot{w}_i\ddot{w}_i})}{\Delta y^2}\right]\right\}$$

$$I_x^b = \frac{D}{\omega^3 h\Delta x} Im\left\{(1-i\eta)\left[\frac{-G_{\ddot{w}_{i+3}\ddot{w}_{i+1}} + G_{\ddot{w}_{i+3}\ddot{w}_i} - 4\left(-G_{\ddot{w}_{i+2}\ddot{w}_{i+1}} + G_{\ddot{w}_{i+2}\ddot{w}_i}\right)}{\Delta x^2}\right.\right.$$

$$+ \frac{5\left(-G_{\ddot{w}_{i+1}\ddot{w}_{i+1}} + G_{\ddot{w}_{i+1}\ddot{w}_i}\right) - 2\left(-G_{\ddot{w}_i\ddot{w}_{i+1}} + G_{\ddot{w}_i\ddot{w}_i}\right)}{\Delta x^2}$$

$$+ \frac{1}{v}\frac{-G_{\ddot{w}_{i-3x}\ddot{w}_{i+1}} + G_{\ddot{w}_{i-3x}\ddot{w}_i} - 4\left(-G_{\ddot{w}_{i-2x}\ddot{w}_{i+1}} + G_{\ddot{w}_{i-2x}\ddot{w}_i}\right)}{\Delta y^2} \quad \text{(B.31)}$$

$$\left.\left. + \frac{1}{v}\frac{5\left(-G_{\ddot{w}_{i-x}\ddot{w}_i} + G_{\ddot{w}_{i-x}\ddot{w}_i}\right) - 2\left(-G_{\ddot{w}_i\ddot{w}_{i+1}} + G_{\ddot{w}_i\ddot{w}_i}\right)}{\Delta y^2}\right]\right\}$$

$$I_x^t = -\frac{D(1-v)}{\omega^3 h\Delta x\Delta y^2} Im\{(1+i\eta)[G_{\ddot{w}_{i-x+1}\ddot{w}_{i+x}} - G_{\ddot{w}_{i-x+1}\ddot{w}_i} - G_{\ddot{w}_{i-x}\ddot{w}_{i-x}} + G_{\ddot{w}_{i-x}\ddot{w}_i} - G_{\ddot{w}_{i+1}\ddot{w}_{i-x}} + G_{\ddot{w}_{i+1}\ddot{w}_i} + G_{\ddot{w}_i\ddot{w}_{i-x}} - G_{\ddot{w}_i\ddot{w}_i}]\} \quad \text{(B.32)}$$

$$I_y^s = \frac{-D}{2\omega^3 h\Delta y} Im\left\{(1-i\eta)\left[\frac{3G_{\ddot{w}_{i-4x}\ddot{w}_i} - 14G_{\ddot{w}_{i-3x}\ddot{w}_i} + 24G_{\ddot{w}_{i-2x}\ddot{w}_i} - 18G_{\ddot{w}_{i-x}\ddot{w}_i} + 5G_{\ddot{w}_i\ddot{w}_i}}{\Delta y^2}\right.\right.$$
$$+\frac{(-G_{\ddot{w}_{i-2x+3}\ddot{w}_i} + 4G_{\ddot{w}_{i-x+3}\ddot{w}_i} - 3G_{\ddot{w}_{i+3}\ddot{w}_i})}{\Delta x^2}$$
$$+\frac{-4(-G_{\ddot{w}_{i-2x+2}\ddot{w}_i} + 4G_{\ddot{w}_{i-x+2}\ddot{w}_i} - 3G_{\ddot{w}_{i+2}\ddot{w}_i})}{\Delta x^2} \quad \text{(B.33)}$$
$$+\frac{5(-G_{\ddot{w}_{i-2x+1}\ddot{w}_i} + 4G_{\ddot{w}_{i-x+1}\ddot{w}_i} - 3G_{\ddot{w}_{i+1}\ddot{w}_i})}{\Delta x^2}$$
$$\left.\left.+\frac{-2(-G_{\ddot{w}_{i-2x}\ddot{w}_i} + 4G_{\ddot{w}_{i-x}\ddot{w}_i} - 3G_{\ddot{w}_i\ddot{w}_i})}{\Delta x^2}\right]\right\}$$

$$I_y^b = \frac{D}{\omega^3 h\Delta y} Im\left\{(1-i\eta)\left[\frac{-(-G_{\ddot{w}_{i-3x}\ddot{w}_{i-x}} + G_{\ddot{w}_{i-3x}\ddot{w}_i}) + 4(-G_{\ddot{w}_{i-2x}\ddot{w}_{i-x}} + G_{\ddot{w}_{i-2x}\ddot{w}_i})}{\Delta y^2}\right.\right.$$
$$+\frac{5(G_{\ddot{w}_{i-x}\ddot{w}_{i-x}} - G_{\ddot{w}_{i-x}\ddot{w}_i}) - 2(G_{\ddot{w}_i\ddot{w}_{i-x}} - G_{\ddot{w}_i\ddot{w}_i})}{\Delta y^2}$$
$$+\frac{1}{v}\frac{G_{\ddot{w}_{i+3}\ddot{w}_{i-x}} - G_{\ddot{w}_{i+3}\ddot{w}_i} - 4(G_{\ddot{w}_{i+2}\ddot{w}_{i-x}} - G_{\ddot{w}_{i+2}\ddot{w}_i})}{\Delta x^2} \quad \text{(B.34)}$$
$$\left.\left.+\frac{1}{v}\frac{+5(G_{\ddot{w}_{i+1}\ddot{w}_{i-x}} - G_{\ddot{w}_{i+1}\ddot{w}_i}) - 2(G_{\ddot{w}_i\ddot{w}_{i-x}} - G_{\ddot{w}_i\ddot{w}_i})}{\Delta x^2}\right]\right\}$$

$$I_y^t = -\frac{D(1-v)}{\omega^3 h\Delta y\Delta x^2} Im\{(1+i\eta)[-G_{\ddot{w}_{i-x+1}\ddot{w}_{i+1}} + G_{\ddot{w}_{i-x+1}\ddot{w}_i} + G_{\ddot{w}_{i+1}\ddot{w}_{i+1}} - G_{\ddot{w}_{i+1}\ddot{w}_i} + G_{\ddot{w}_{i-x}\ddot{w}_{i+1}} - G_{\ddot{w}_{i-x}\ddot{w}_i} - G_{\ddot{w}_i\ddot{w}_{i+1}} + G_{\ddot{w}_i\ddot{w}_i}]\} \quad \text{(B.35)}$$

In region 8, central-backward differencing is used according the grid shown in Figure B-7, giving each SI component as Equations (B.36)-(B.41).

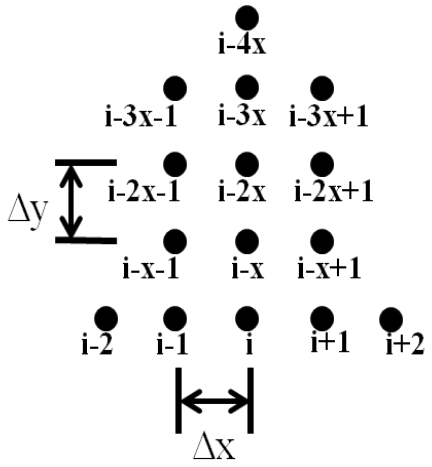

Figure B-7: Array used to calculate SI at any point within region 8 on a plate. The SI vector at the center point (point #i) is calculated via finite differencing of the structural response matrix.

$$I_x^s = \frac{-D}{2\omega^3 h\Delta x} Im\left\{(1-i\eta)\left[\frac{G_{\ddot{w}_{i+2}\ddot{w}_i} - 2G_{\ddot{w}_{i+1}\ddot{w}_i} + 2G_{\ddot{w}_{i-1}\ddot{w}_i} - G_{\ddot{w}_{i-2}\ddot{w}_i}}{\Delta x^2}\right.\right.$$
$$+ \frac{-(G_{\ddot{w}_{i-3x+1}\ddot{w}_i} - G_{\ddot{w}_{i-3x-1}\ddot{w}_i}) + 4(G_{\ddot{w}_{i-2x+1}\ddot{w}_i} - G_{\ddot{w}_{i-2x-1}\ddot{w}_i})}{\Delta y^2} \quad \text{(B.36)}$$
$$\left.\left. + \frac{-5(G_{\ddot{w}_{i-x+1}\ddot{w}_i} - G_{\ddot{w}_{i-x-1}\ddot{w}_i}) + 2(G_{\ddot{w}_{i+1}\ddot{w}_i} - G_{\ddot{w}_{i-1}\ddot{w}_i})}{\Delta y^2}\right]\right\}$$

$$I_x^b = \frac{D}{2\omega^3 h\Delta x} Im\left\{(1-i\eta)\left[\frac{G_{\ddot{w}_{i+1}\ddot{w}_{i+1}} - G_{\ddot{w}_{i+1}\ddot{w}_{i-1}} - 2\left(G_{\ddot{w}_i\ddot{w}_{i+1}} - G_{\ddot{w}_i\ddot{w}_{i-1}}\right)}{\Delta x^2}\right.\right.$$
$$+ \frac{G_{\ddot{w}_{i-1}\ddot{w}_{i+1}} - G_{\ddot{w}_{i-1}\ddot{w}_{i-1}}}{\Delta x^2}$$
$$+ \frac{1}{\upsilon}\frac{-G_{\ddot{w}_{i-3x}\ddot{w}_{i+1}} + G_{\ddot{w}_{i-3x}\ddot{w}_{i-1}} + 4\left(G_{\ddot{w}_{i-2x}\ddot{w}_{i+1}} - G_{\ddot{w}_{i-2x}\ddot{w}_{i-1}}\right)}{\Delta y^2} \quad \text{(B.37)}$$
$$\left.\left. + \frac{1}{\upsilon}\frac{-5\left(G_{\ddot{w}_{i-x}\ddot{w}_{i+1}} - G_{\ddot{w}_{i-x}\ddot{w}_{i-1}}\right) + 2\left(G_{\ddot{w}_i\ddot{w}_{i+1}} - G_{\ddot{w}_i\ddot{w}_{i-1}}\right)}{\Delta y^2}\right]\right\}$$

$$I_x^t = \frac{D(1-\upsilon)}{2\omega^3 h\Delta x\Delta y^2} Im\{(1+i\eta)[G_{\ddot{w}_{i-x+1}\ddot{w}_{i-x}} - G_{\ddot{w}_{i-x+1}\ddot{w}_i} - G_{\ddot{w}_{i-x-1}\ddot{w}_{i+x}} + G_{\ddot{w}_{i-x-1}\ddot{w}_i} - G_{\ddot{w}_{i+1}\ddot{w}_{i-x}} \quad \text{(B.38)}$$
$$+ G_{\ddot{w}_{i+1}\ddot{w}_i} + G_{\ddot{w}_{i-1}\ddot{w}_{i-x}} - G_{\ddot{w}_{i-1}\ddot{w}_i}]\}$$

$$I_y^s = \frac{-D}{2\omega^3 h\Delta y} Im\left\{(1-i\eta)\left[\frac{3G_{\ddot{w}_{i-4x}\ddot{w}_i} - 14G_{\ddot{w}_{i-3x}\ddot{w}_i} + 24G_{\ddot{w}_{i-2x}\ddot{w}_i} - 8G_{\ddot{w}_{i-x}\ddot{w}_i} + 5G_{\ddot{w}_i\ddot{w}_i}}{\Delta y^2}\right.\right.$$
$$+ \frac{(G_{\ddot{w}_{i-2x+1}\ddot{w}_i} - 4G_{\ddot{w}_{i-x+1}\ddot{w}_i} + 3G_{\ddot{w}_{i+1}\ddot{w}_i}) + 2(-G_{\ddot{w}_{i-2x}\ddot{w}_i} + 4G_{\ddot{w}_{i-x}\ddot{w}_i} - 3G_{\ddot{w}_i\ddot{w}_i})}{\Delta x^2} \quad \text{(B.39)}$$
$$\left.\left. + \frac{-(-G_{\ddot{w}_{i-2x-1}\ddot{w}_i} + 4G_{\ddot{w}_{i-x-1}\ddot{w}_i} - 3G_{\ddot{w}_{i-1}\ddot{w}_i})}{\Delta x^2}\right]\right\}$$

$$I_y^b = \frac{D}{\omega^3 h\Delta y} Im\left\{(1-i\eta)\left[\frac{-G_{\ddot{w}_{i-3x}\ddot{w}_{i-x}} + G_{\ddot{w}_{i-3x}\ddot{w}_i} + 4\left(G_{\ddot{w}_{i-2x}\ddot{w}_{i-x}} - G_{\ddot{w}_{i-2x}\ddot{w}_i}\right)}{\Delta y^2}\right.\right.$$
$$+ \frac{-5\left(G_{\ddot{w}_{i-x}\ddot{w}_{i-x}} - G_{\ddot{w}_{i-x}\ddot{w}_i}\right) + 2\left(G_{\ddot{w}_i\ddot{w}_{i-x}} - G_{\ddot{w}_i\ddot{w}_i}\right)}{\Delta y^2} \quad \text{(B.40)}$$
$$\left.\left. + \frac{1}{v}\frac{G_{\ddot{w}_{i+1}\ddot{w}_{i-x}} - G_{\ddot{w}_{i+1}\ddot{w}_i} - 2\left(G_{\ddot{w}_i\ddot{w}_{i-x}} - G_{\ddot{w}_i\ddot{w}_i}\right) + \left(G_{\ddot{w}_{i-1}\ddot{w}_{i-x}} - G_{\ddot{w}_{i-1}\ddot{w}_i}\right)}{\Delta x^2}\right]\right\}$$

$$I_y^t = \frac{D(1-v)}{4\omega^3 h\Delta y\Delta x^2} Im\{(1+i\eta)[G_{\ddot{w}_{i-x+1}\ddot{w}_{i+1}} - G_{\ddot{w}_{i-x+1}\ddot{w}_{i-1}} - G_{\ddot{w}_{i+1}\ddot{w}_{i+1}} + G_{\ddot{w}_{i+1}\ddot{w}_{i-1}} - G_{\ddot{w}_{i-x-1}\ddot{w}_{i+1}}$$
$$+ G_{\ddot{w}_{i-x-1}\ddot{w}_{i-1}} + G_{\ddot{w}_{i-1}\ddot{w}_{i+1}} - G_{\ddot{w}_{i-1}\ddot{w}_{i-1}}]\} \quad \text{(B.41)}$$

In region 9, backward-backward differencing is used according the grid shown in Figure B-8, giving each SI component as Equations (B.42) – (B.46).

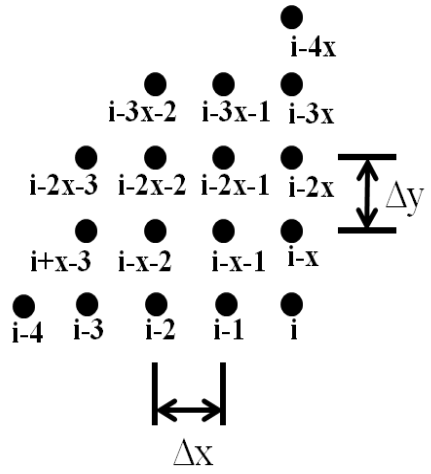

Figure B-8: Array used to calculate SI at any point within region 9 on a plate. The SI vector at the center point (point #i) is calculated via finite differencing of the structural response matrix.

$$I_x^s$$

$$= \frac{-D}{2\omega^3 h\Delta x} Im\left\{(1-i\eta)\left[\frac{-3G_{\ddot{w}_{i-4}\ddot{w}_i} + 14G_{\ddot{w}_{i-3}\ddot{w}_i} - 24G_{\ddot{w}_{i-2}\ddot{w}_i} + 18G_{\ddot{w}_{i-1}\ddot{w}_i} - 5G_{\ddot{w}_i\ddot{w}_i}}{\Delta x^2}\right.\right.$$

$$+ \frac{-(-G_{\ddot{w}_{i-3x-2}\ddot{w}_1} + 4G_{\ddot{w}_{i-3x-1}\ddot{w}_i} - 3G_{\ddot{w}_{i-3x}\ddot{w}_i}) + 4(-G_{\ddot{w}_{i-2x-2}\ddot{w}_i} + 4G_{\ddot{w}_{i-2x-1}\ddot{w}_i} - 3G_{\ddot{w}_{i-2x}\ddot{w}_i})}{\Delta y^2} \quad \text{(B.42)}$$

$$\left.\left. + \frac{-5(-G_{\ddot{w}_{i-x-2}\ddot{w}_i} + 4G_{\ddot{w}_{i-x-1}\ddot{w}_i} - 3G_{\ddot{w}_{i-x}\ddot{w}_i}) + 2(-G_{\ddot{w}_{i-2}\ddot{w}_i} + 4G_{\ddot{w}_{i-1}\ddot{w}_i} - 3G_{\ddot{w}_i\ddot{w}_i})}{\Delta y^2}\right]\right\}$$

$$I_x^b = \frac{D}{\omega^3 h\Delta x} Im\left\{(1-i\eta)\left[\frac{-\left(-G_{\ddot{w}_{i-3}\ddot{w}_{i-1}} + G_{\ddot{w}_{i-3}\ddot{w}_i}\right) + 4\left(G_{\ddot{w}_{i-2}\ddot{w}_{i-1}} - G_{\ddot{w}_{i-2}\ddot{w}_i}\right)}{\Delta x^2}\right.\right.$$

$$+ \frac{-5\left(G_{\ddot{w}_{i-1}\ddot{w}_{i-1}} - G_{\ddot{w}_{i-1}\ddot{w}_i}\right) + 2\left(G_{\ddot{w}_i\ddot{w}_{i-1}} - G_{\ddot{w}_i\ddot{w}_i}\right)}{\Delta x^2}$$

$$+ \frac{1}{\upsilon}\frac{-\left(G_{\ddot{w}_{i-3x}\ddot{w}_{i-1}} - G_{\ddot{w}_{i-3x}\ddot{w}_i}\right) + 4\left(G_{\ddot{w}_{i-2x}\ddot{w}_{i-1}} - G_{\ddot{w}_{i-2x}\ddot{w}_i}\right)}{\Delta y^2} \quad \text{(B.43)}$$

$$\left.\left. + \frac{1}{\upsilon}\frac{-5\left(G_{\ddot{w}_{i-x}\ddot{w}_{i-1}} - G_{\ddot{w}_{i-x}\ddot{w}_i}\right) + 2\left(G_{\ddot{w}_i\ddot{w}_{i-1}} - G_{\ddot{w}_i\ddot{w}_i}\right)}{\Delta y^2}\right]\right\}$$

$$I_x^t = -\frac{D(1-\upsilon)}{\omega^3 h\Delta x\Delta y^2} Im\{(1+i\eta)[G_{\ddot{w}_{i-x-1}\ddot{w}_{i-x}} - G_{\ddot{w}_{i-x-1}\ddot{w}_i} - G_{\ddot{w}_{i-x}\ddot{w}_{i-x}} + G_{\ddot{w}_{i-x}\ddot{w}_i} - G_{\ddot{w}_{i-1}\ddot{w}_{i-x}}$$
$$+ G_{\ddot{w}_{i-1}\ddot{w}_i} + G_{\ddot{w}_i\ddot{w}_{i-x}} - G_{\ddot{w}_i\ddot{w}_i}]\} \quad \text{(B.44)}$$

$$I_y^s = \frac{-D}{2\omega^3 h\Delta y} Im\left\{(1-i\eta)\left[\frac{-3G_{\ddot{w}_{i-4x}\ddot{w}_i} + 14G_{\ddot{w}_{i-3x}\ddot{w}_i} - 24G_{\ddot{w}_{i-2x}\ddot{w}_i} + 18G_{\ddot{w}_{i-x}\ddot{w}_i} - 5G_{\ddot{w}_i\ddot{w}_i}}{\Delta y^2}\right.\right.$$

$$+ \frac{-(-G_{\ddot{w}_{i-2x-3}\ddot{w}_i} + 4G_{\ddot{w}_{i-x-3}\ddot{w}_i} - 3G_{\ddot{w}_{i-3}\ddot{w}_i})}{\Delta x^2}$$

$$+ \frac{4(-G_{\ddot{w}_{i-2x-2}i} + 4G_{\ddot{w}_{i-x-2}\ddot{w}_i} - 3G_{\ddot{w}_{i-2}\ddot{w}_i})}{\Delta x^2} \quad \text{(B.45)}$$

$$+ \frac{-5(-G_{\ddot{w}_{i-2x-1}\ddot{w}_i} + 4G_{\ddot{w}_{i-x-1}\ddot{w}_i} - 3G_{\ddot{w}_{i-1}\ddot{w}_i})}{\Delta x^2}$$

$$\left.\left. + \frac{2(-G_{\ddot{w}_{i-2x}\ddot{w}_i} + 4G_{\ddot{w}_{i-x}\ddot{w}_i} - 3G_{\ddot{w}_i\ddot{w}_i})}{\Delta x^2}\right]\right\}$$

$$I_y^b = \frac{D}{\omega^3 h \Delta y} Im\left\{(1-i\eta)\left[\frac{-\left(G_{\ddot{w}_{i-3x}\ddot{w}_{i-x}} - G_{\ddot{w}_{i-3x}\ddot{w}_i}\right) + 4\left(G_{\ddot{w}_{i-2x}\ddot{w}_{i-x}} - G_{\ddot{w}_{i-2x}\ddot{w}_i}\right)}{\Delta y^2}\right.\right.$$

$$+\frac{-5\left(G_{\ddot{w}_{i-x}\ddot{w}_{i-x}} - G_{\ddot{w}_{i-x}\ddot{w}_i}\right) + 2\left(G_{\ddot{w}_i\ddot{w}_{i-x}} - G_{\ddot{w}_i\ddot{w}_i}\right)}{\Delta y^2}$$

$$+\frac{1}{v}\frac{-\left(G_{\ddot{w}_{i-3}\ddot{w}_{i-x}} - G_{\ddot{w}_{i-3}\ddot{w}_i}\right) + 4\left(G_{\ddot{w}_{i-2}\ddot{w}_{i-x}} - G_{\ddot{w}_{i-2}\ddot{w}_i}\right)}{\Delta x^2} \tag{B.46}$$

$$\left.\left.+\frac{1}{v}\frac{-5\left(G_{\ddot{w}_{i-1}\ddot{w}_{i-x}} - G_{\ddot{w}_{i-1}\ddot{w}_i}\right) + 2\left(G_{\ddot{w}_i\ddot{w}_{i-x}} - G_{\ddot{w}_i\ddot{w}_i}\right)}{\Delta x^2}\right]\right\}$$

References

1. Farrar, B., R., Worden, K., 2006, "An Introduction to Structural Health Monitoring", *Philosophical Transaction of the Royal Society*, Vol.365, pp.303-315.

2. Hood and D. Pines, "Feasibility of a phased acoustic array for monitoring acoustic signatures from meshing gear teeth," *Journal of the Acoustical Society of America* 112(6), 2849-57, 2002.

3. Halfpenny, T.C. Walton, "CBM for vibrating equipment on rotorcraft," *American Helicopter Society Technical Specialists' Meeting on Condition Based Maintenance*, Huntsville, AL, February 10-11, 2009.

4. Montalvao, D., N. M. M. Maia and A. M. R. Ribeiro. "A Review of Vibration-Based Structural Health Monitoring with Special Emphasis on Composite Materials." *The Shock and Vibration Digest* (2006): 295-324.

5. Doebling, Scott W., Farrar, Charles R., Prime, Michael B., 1998, "A summary review of vibration-based damage identification methods", *Shock and Vibration Digest*, v 30, n 2, pp. 91-105.

6. B. Larder, "An analysis of HUMS diagnostic capabilities", *American Helicopter Society 53rd Annual Forum*, Virginia Beach, VA, April 29-may 1, 1997.

7. I.Y. Solodov, "Ultrasonics of non-linear contacts: propagation, reflection and NDE-applications," *Ultrasonics*,36,383-390 (1998).

8. Y. Ohara, T. Mihara, R. Sasaki, T. Ogata, S. Yamamoto, Y. Kishimoto, and K. Yamanaka, "Imaging of closed cracks using nonlinear response of elastic waves at subharmonic frequencies," *Applied Physics Letters*, 90, 011902 (2007).

9. I.Y. Solodov, "CAN: an example of nonclassical acoustic nonlinearity in solids," *Ultrasonics*,40,621-625 (2002) .

10. I.Y. Solodov, J. Wackerl, K. Pfleiderer, G. Busse, "Nonlinear self-modulation and subharmonic acoustic spectroscopy for damage detection and location," *Applied Physics Letters*, 84, 5386 (2004) .

11. I.Y. Solodov, "Non-classical nonlinearity in solids for defect-selective imaging and NDE," *IUTAM Symposium on Recent Advances of Acoustic Waves in Solids*, IUTAM Bookseries 26, 2010

12. K. Van Den Abeele, P. Johnson A. Sutin, "Nonlinear elastic wave spectroscopy (NEWS) techniques to discern material damage, Pat 1: Nonlinear Wave Modulation Spectroscopy (NWMS)," *Research in Nondestructive Evaluation*, 12(1), 17-30 (2000).

13. K. Van Den Abeele, A. Sutin, J. Carmeliet, P. Johnson, "Micro-damage diagnostics using nonlinear elastic wave spectroscopy (NEWS)," *NDT&E International*, 34, 239-248 (2001).

14. F. Semperlotti, “Structural damage detection via nonlinear system identification and structural intensity methods,” Ph.D. Dissertation, The Pennsylvania State University, 2009.

15. Noiseux, D. “Measurement of Power Flow in Uniform Beams and Plates.” *Journal of the Acoustical Society of America* (1970): 239-247.

16. Pavic, G. “Measurement of Structure Borne Wave Intensity, Part 1: Formulation of the Methods,” *Journal of Sound and Vibration* (1976): 221-230.

17. S. C. Conlon, M. R. Shepherd, J. A. Hines, A. R. Barnard, F. Semperlotti, P. Q. Romano, E. C. Smith, “Development of an Airframe Intensity Based Structural Health Monitoring System”, *American Helicopter Society 66th Annual Forum*, Phoenix, AZ, May 11-13, 2010.

18. W. Schmidt, “Open crack damage assessment using structural intensity-based techniques,” M.S. Thesis, The Pennsylvania State University, 2009.

19. F. Semperlotti and S.C. Conlon, “Structural damage identification in plates via nonlinear structural intensity maps,” *Journal of the Acoustical Society of America* 127(2), EL48-EL53, 2010.

20. G. Pavic, “Structural Surface Intensity: an Alternative Approach in Vibration Analysis and Diagnosis,” *Journal of Sound and Vibration*, Vol. 115, No. 3, pp. 405-422, 1987.

21. F. Semperlotti, S. C. Conlon “Nonlinear Structural Surface Intensity: an application of contact acoustic nonlinearity to power flow based damage detection”, *Applied Physics Letters*, 97, 1 (2010).

22. J.W. Dally and W.F. Riley, *Experimental Stress Analysis*, College House Enterprises, Knoxville, 2005.

23. J.S. Bendat and A.G Piersol, *Random Data Analysis and Measurement Procedures*, Fourth Edition, John Wiley and Sons Inc., New York, NY, 2010.

24. Conlon, S., May, R., Hambric, S., Banks, J., and K. Reichard. “Structural Intensity Measurement for Damage Detection.” Proceedings, Inter-Noise Conference. Istanbul, Turkey. 2007.

25. Arruda, J. R. F., and P. Mas. “Predicting and Measuring Flexural Power Flow in Plates.” Proceedings, SPIE. Washington, DC. 1996.

26. Daley, M. J. “Prediction and Measurement of Structural Intensity in Thin Plates Excited by Distributed Random Fluctuating Pressure Fields.” Ph.D. Thesis, The Pennsylvania State University Graduate Program in Acoustics, 2003.

27. Cremer, L.,Heckl, M. and Petersson, B.A.T, “Structure borne sound: structural vibrations and sound radiations at audio frequencies,” Berlin, Germany, Springer-Verlag, 2010.

28. James, M., Smith, G., and J. Wolford. “Applied Numerical Methods for Digital Computation with FORTRAN and CSMP.” Boston, MA, Addison-Wesley Longman Publishing Co., 1977.

29. Daley, M. and S. Hambric. “Simulating and Measuring Structural Intensity Fields in Plates Induced by Spatially and Temporally Random Excitation.” Journal of Vibration and Acoustics. (2005): 451-457.

30. F. Jacobsen, “Decay rates and wall absorption at low frequencies.” Journal of Sound and Vibration 81 (3), 1982.

31. S. Conlon, F. Semperlotti, M. Shepherd, J. Hines, P. Romano, A. Barnard, E. Smith, J. Banks. “Intensity Based Structural Health Monitoring.” Technical Report, U.S. Army Research, Development & Engineering Command, Aviation Applied Technology Directorate, Contract No. W911W6-08-C-0036